International Scientific-Technical and Production Journal

The Paton WELDING JOURNAL

June 2010 # 6

English translation of the monthly «Avtomaticheskaya Svarka» (Automatic Welding) journal published in Russian since 1948

Founders: *E.O. Paton Electric Welding Institute of the NAS of Ukraine International Association «Welding»* ***Publisher:*** *International Association «Welding»*

Address:
E.O. Paton Electric Welding Institute,
International Association «Welding»,
11, Bozhenko str., 03680, Kyiv, Ukraine
Tel.: (38044) 287 67 57
Fax: (38044) 528 04 86
E-mail: journal@paton.kiev.ua
http://www.nas.gov.ua/pwj

State Registration Certificate
KV 4790 of 09.01.2001

Subscriptions:
$324, 12 issues per year,
postage and packaging included.
Back issues available.

CONTENTS

MODEL OF THE PROCESSES OF HEAT, MASS AND CHARGE TRANSFER IN THE ANODE REGION AND COLUMN OF THE WELDING ARC WITH REFRACTORY CATHODE

I.V. KRIVTSUN[1], **V.F. DEMCHENKO**[1] and **I.V. KRIKENT**[2]
[1]E.O. Paton Electric Welding Institute, NASU, Kiev, Ukraine
[2]Dneprodzerzhinsk State Technical University, Dneprodzerzhinsk, Ukraine

The main difference of the proposed mathematical model of the welding arc from the known ones describing the atmospheric-pressure arcs is allowance for the multi-component composition of the arc plasma, which is caused by evaporation of the anode metal and convective diffusion of metal vapours in the arc column. The model can be used for numerical analysis of thermal, gas-dynamic and electromagnetic characteristics of the arc plasma in inert-gas tungsten-electrode and plasma welding, as well as for modelling of thermal and dynamic effects of the arc on the weld pool surface.

Keywords: *tungsten-electrode welding, plasma welding, electric arc, arc column, multi-component plasma, anode region, anode potential drop, mathematical model*

Many models are available for numerical investigation of the processes of energy, impulse, mass and charge transfer in plasma of the electric arc, as well as of the processes of its interaction with electrodes using different arc welding methods [1–14]. However, most of them assume that the arc plasma is one-component, i.e. containing atoms and ions of a shielding or plasma gas, which is the inert one in the majority of cases. As a rule, plasma of the real welding arcs is multi-component, as along with gas particles it also contains atoms and ions of an evaporating material of electrodes, and anode in the first turn. Therefore, it is necessary to allow for the multi-component nature of the arc plasma in development of an adequate mathematical model.

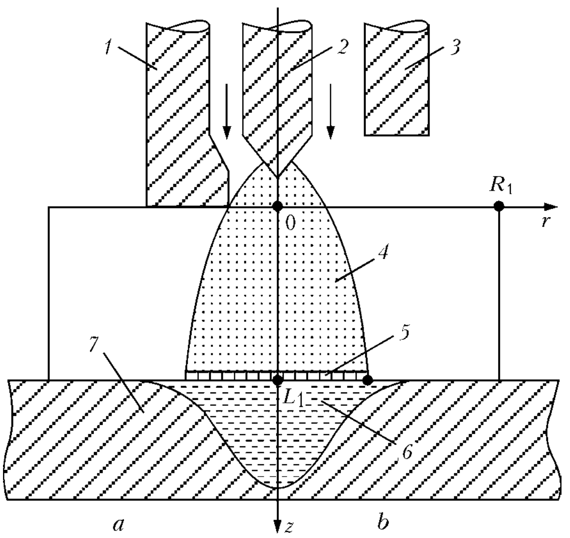

Figure 1. Schematics of plasma (*a*) and TIG (*b*) welding: *1* — plasma-shaping nozzle; *2* — refractory electrode (cathode); *3* — shielding gas nozzle; *4* — arc column; *5* — anode region of the arc; *6* — weld pool; *7* — workpiece (anode)

Such a model must have another important characteristic — self-consistency, which makes it possible to allow for relationship between the physical processes occurring at electrodes and in near-electrode plasma regions and processes occurring in the arc column. It should be noted that the majority of studies dedicated to integrated modelling of the electric (including welding) arc use fairly simplified models of the near-electrode regions [4, 6, 9–12], whereas studies dedicated to investigation of the near-electrode phenomena (e.g. [15] and references given in it) pay an insufficient attention to the processes occurring in the arc column.

As theories of the cathode phenomena, as well as processes occurring in the near-cathode plasma of the electric arc with a refractory (non-evaporating) cathode are adequately elaborated [16–19], the purpose of the present study consists in development of the self-consistent mathematical model of physical processes taking place in the anode region and welding arc column (electric arc with the evaporating anode) in inert-gas tungsten-electrode and plasma welding (Figure 1).

Processes occurring in the arc plasma adjoining the surface of the evaporating anode are described by using the approach suggested in studies [20–22], according to which the near-anode plasma is conditionally subdivided into three zones (Figure 2).

The first zone directly adjoining the anode surface is a layer of the space charge, wherein the condition of quasi-neutrality of the plasma in violated and the main potential drop takes place between the plasma and anode. This layer can be considered collisionless, as under a pressure close to the atmospheric one and at electron temperature $T_e \sim 1$ eV characteristic of the conditions under investigation [23, 24], thickness of this layer $\bar{x}$ commensurable with Debye radius $r_D \sim 1\cdot10^{-8}$ m (here and further on the line over a letter means that the value relates to the external boundary of the space charge layer) turns out to be much smaller than the characteristic length of free path of the plasma particles, $l \sim 1\cdot10^{-7}$–$1\cdot10^{-5}$ m (estimations in this study were made for the atmospheric-pressure Fe-plasma).

The second zone is an ionisation region of the non-isothermal quasi-neutral plasma (presheath), wherein the charged particles are generated due to plasma electron ionisation of the gas atoms desorbed from the surface of the metallic anode and evaporating metal atoms. Ions formed here are accelerated towards the anode surface by the electric field induced by more mobile electrons and recombine near this surface. Therefore, conditions of local ionisation equilibrium are violated within the ionisation region. Moreover, a marked change of the plasma potential takes place here, which can be commensurable with its drop in the space charge layer.

The Knudsen layer boundary, which we will compare with a boundary of the anode region, is situated at a distance from the anode surface equal to several lengths of free path of the heavy particles. The third zone begins outside the anode region. This zone is a gas-dynamic plasma region with a local thermodynamic equilibrium formed therein. It should be noted that this region can also be conditionally subdivided into two zones: thermal boundary layer, wherein electron and heavy particles temperatures, T_e^0 and T_h^0, level with the plasma temperature in the arc column, T, and the arc column proper [23].

Because Knudsen layer thickness $L_K \sim 1\cdot10^{-4}$ m is much smaller than anode surface (weld pool) curvature radius $R \sim 1\cdot10^{-3}$ m, the latter can be assumed to be flat in description of the processes occurring in the anode region. As L_K is much smaller than the characteristic scale of measurement of plasma parameters in the gas-dynamic region, when considering the transfer processes taking place in the arc column the anode region can be assumed to be infinitely thin. Therefore, from the standpoint of mathematical description of the processes in the arc plasma, it can be broken down into two regions: anode region (or Knudsen layer) and arc column (or gas-dynamic region), for which the first region is a discontinuity surface. In this connection, the self-consistent mathematical model of the processes of energy, mass and charge transfer in the column plasma and anode region of the welding arc with the refractory cathode should include two interrelated models: model of the thermal, electromagnetic, gas-dynamic and diffusion processes occurring in the multi-component plasma of the arc column, and model of the anode region of the arc, which makes it possible to formulate boundary conditions on the anode surface required to solve equations of the arc column model and determine characteristics of the thermal and dynamic effect of the arc on the weld pool surface.

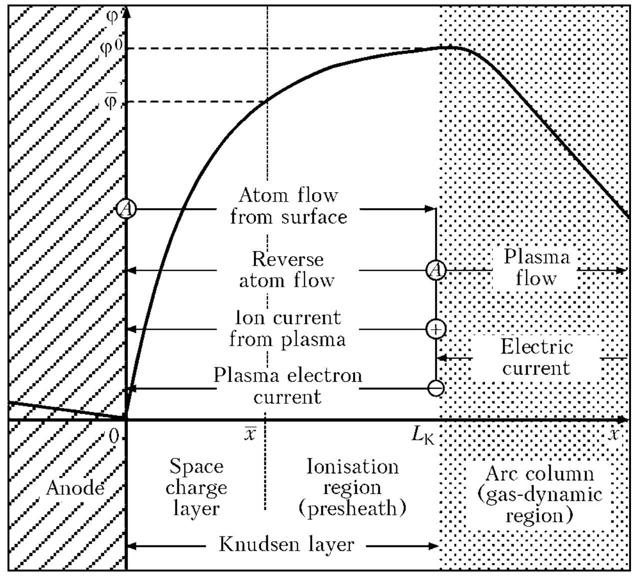

Figure 2. Structure of plasma presheath, particle flows and distribution of potential in the anode region of the welding arc: $\bar{\varphi}$ — value of potential at the space charge boundary layer; A — atoms; + — ions; − — electrons; the rest of the designations are given in the text

Consider first the model of the processes of charge, mass and energy transfer in the anode region of the welding arc.

Model of the anode region. To describe processes occurring in the anode region of the arc with the evaporating anode, assume that plasma at the external boundary of this region is characterised by the following parameters: n_e^0 — concentration of electrons; $n_{\alpha Z}^0$ — concentration of atoms (charge number $Z = 0$) and ions ($Z = 1$) of the shielding or plasma gas (kind of particles $\alpha = g$), atoms ($Z = 0$) and ions ($Z = 1$, 2) of the metal vapour ($\alpha = m$); Z_e — ion charge; e — elementary charge; T_h^0 — temperature of heavy particles, which is assumed to be identical for all kinds of atoms and ions, but differing from T_e^0 (two-temperature plasma model); m_e — electron mass; M_α — masses of heavy particles (atoms and ions) of gas ($\alpha = g$) and metal ($\alpha = m$); and j_a — density of the electric current on the anode surface. As noted above, the anode region can be considered flat. Hence, the n_e^0, $n_{\alpha Z}^0$, T_e^0, T_h^0 and j_a values can be regarded as local, corresponding to a given point on the anode surface, which is characterised by a local value of temperature T_s.

Assume that the current is transferred to the anode only with electrons and ions coming from the plasma (assume that ions arriving on the anode surface recombine there and come back in the form of atoms, and the flow of electrons emitted by the anode is negligibly small). Then the total density of the electric current on the anode surface can be represented as follows:

$$j_a = j_e - j_i \ (j_a > 0), \tag{1}$$

where j_e is the density of the electric current coming to the anode, and $J_i = \sum_{\alpha = m,\, g;\, Z \geq 1} j_{\alpha Z}$ is the total density of the ion current (for ions of all kinds and charges).

The electron component of the plasma within the anode region can be considered collisionless to a high degree of accuracy, and electron temperature — almost constant through its thickness. In addition, as the plasma potential is, as a rule, higher than the anode potential [24], electrons are decelerated by the electric field, and ions are accelerated towards the anode surface. In this case, the density of the electron current on the anode is [23]

$$j_e = \frac{1}{4} e n_e^0 v_{T_e} \exp\left(-\frac{e\varphi^0}{kT_e^0}\right), \tag{2}$$

where $v_{T_e} = \sqrt{\dfrac{8kT_e^0}{\pi m_e}}$ is the thermal velocity of electrons at the external boundary of the anode region; k is the Boltzmann constant; and φ^0 is the plasma potential with respect to the anode surface ($\varphi^0 > 0$).

To find the ion currents, it is necessary to consider the processes occurring in the ionisation region, wherein ions are generated and accelerated towards the anode. For this, we will use the approach [25] based on an assumption that the length of the free path of ions relative to Coulomb collisions between them is much smaller than the ionisation length and length of their free path at collision with atoms (their characteristic values, respectively, are as follows: $l_{ii} \sim \sim 1\cdot 10^{-7}$ m, $l_{ion} \sim 1\cdot 10^{-6}$ m, $l_{ia} \sim 1\cdot 10^{-5}$ m). This suggests that ions in the presheath are intensively maxwellised and acquire the common directed motion velocity, the value of which at a boundary of the ionisation region with the space charge layer is determined by the following expression:

$$\overline{V}_i \equiv v_i(\overline{x}) = \sqrt{\frac{\sum\limits_{\alpha = m,\, g;\, Z \geq 1} k(ZT_e^0 + T_h^0) n_{\alpha Z}^0}{\sum\limits_{\alpha = m,\, g;\, Z \geq 1} M_\alpha n_{\alpha Z}^0}};$$

$$\left(\overline{V}_i = \frac{w^0}{2}\left[\sqrt{1 + \frac{4\sum\limits_{Z \geq 1} k(ZT_e^0 + T_h^0) n_{\alpha Z}^0}{(w^0)^2 \sum\limits_{Z \geq 1} M_m n_{mZ}^0}} - 1\right]\right). \tag{3}$$

The first relationship in formula (3) corresponds to the diffusion mode of evaporation ($w^0 \approx 0$) [22], whereas the expression in brackets corresponds to the convective mode of evaporation of the anode metal ($w^0 > 0$), where w^0 is the vapour velocity at the anode region boundary, which is normal to the anode surface.

By selecting such a value of $\overline{x}$ as a boundary of the presheath with the space charge layer, at which the plasma quasi-neutrality condition is violated [26], we find the concentration of charged particles at this boundary [22]:

$$\overline{n}_e \equiv n_e(\overline{x}) = n_e^0 \exp\left(-\frac{1}{2}\right);$$
$$\overline{n}_{\alpha Z} \equiv n_{\alpha Z}(\overline{x}) = n_{\alpha Z}^0 \exp\left(-\frac{1}{2}\right), \quad \alpha = m,\, g;\, Z \geq 1. \tag{4}$$

Then the ion currents to the anode surface can be written down as follows:

$$j_{\alpha Z} = Zen_{\alpha Z}^0 \exp\left(-\frac{1}{2}\right) \overline{V}_i, \quad \alpha = m, \quad g;\, Z \geq 1. \tag{5}$$

In the convective mode of evaporation of the anode, the exp $(-1/2)$ value in (4) and (5) should be replaced by

$$\exp\left[-\frac{(w^0)^2 \sum\limits_{Z \geq 1} M_m n_{mZ}^0}{8\sum\limits_{Z \geq 1} k(ZT_e^0 + T_h^0) n_{mZ}^0} \times \left\{1 + \sqrt{1 + \frac{4\sum\limits_{Z \geq 1} k(ZT_e^0 + T_h^0) n_{mZ}^0}{(w^0)^2 \sum\limits_{Z \geq 1} M_m n_{mZ}^0}}\right\}^2\right].$$

The values of the electron and ion currents on the anode surface being known, plasma potential φ^0 relative to this surface or anode potential drop U_a can be easily found from equation (1):

$$U_a \equiv -\varphi^0 = -\frac{kT_e^0}{e} \ln\left(\frac{en_e^0 v_{T_e}}{4\left[j_a + \sum\limits_{\alpha = m,\, g;\, Z \geq 1} j_{\alpha Z}\right]}\right). \tag{6}$$

Calculation of the j_e, $j_{\alpha Z}$ and U_a values requires the knowledge of temperatures T_e^0 and T_h^0, as well as concentrations n_e^0 and $n_{\alpha Z}^0$ of the charged particles at the external boundary of the anode region. Assuming that the multi-component plasma in the arc column is ionisation-equilibrium, the composition of such plasma at a boundary with the anode region can be determined by using the following system of equations:

- Saha equation allowing for plasma imperfection

$$\frac{n_e^0 n_{\alpha Z+1}^0}{n_{\alpha Z}^0} = \left(\frac{2\pi m_e k T_e^0}{h^2}\right)^{3/2} \frac{2\theta_{\alpha Z+1}}{\theta_{\alpha Z}} \times \exp\left[-\frac{e(U_{\alpha Z} - \Delta U_Z)}{kT_e^0}\right], \quad \alpha = m,\, g; \quad Z \geq 0, \tag{7}$$

where h is the Planck's constant; $\theta_{\alpha Z}$ are the statistical sums for heavy particles of kind α, which are in charged state Z; $U_{\alpha Z}$ are the ionisation potentials (for transfer of the particles of kind α from charged state Z to $Z + 1$); $\Delta U_Z = \dfrac{e(Z+1)}{r_D}$ is the decrease of the ionisation potentials caused by interaction of the charged particles of the plasma; and

$$r_{\rm D} = \left[kT_e^0/4\pi e^2 \left(n_e^0 + \frac{T_e^0}{T_h^0} \sum_{\alpha = m,\, g;\, Z \geq 1} n_{\alpha Z}^0 Z^2 \right) \right]^{-1/2};$$

- quasi-neutrality condition of plasma

$$n_e^0 = \sum_{\alpha = m,\, g;\, Z \geq 1} n_{\alpha Z}^0 Z; \qquad (8)$$

- law of partial pressures

$$p = n_e^0 kT_e^0 + \sum_{Z \geq 0} n_{mZ}^0 kT_h^0 + \sum_{Z \geq 0} n_{gZ}^0 kT_h^0 - \Delta p. \qquad (9)$$

Here p is the plasma pressure near the anode, and $\Delta p = \frac{1}{6} \frac{e^2}{r_{\rm D}} \left(n_e^0 + \sum_{\alpha = m,\, g;\, Z \geq 0} n_{\alpha Z}^0 Z^2 \right)$ is the decrease of the pressure due to the plasma imperfection [27].

Another condition determining the concentration of the metal vapour particles at the external boundary of the anode region is required to close the system of equations (7) through (9). With the diffusion mode of evaporation, the rate of diffusion of the vapour particles is assumed to be low, i.e. the vapour state is close to saturation. The equality of partial pressure of the heavy particles of the evaporated metal at this boundary to saturated vapour pressure p_s over the surface of the molten metal with temperature T_s can be chosen as such a condition:

$$\sum_{Z \geq 0} n_{mZ}^0 kT_h^0 = p_s \equiv p_0 \exp \left[\frac{\lambda_v}{k} \left(\frac{1}{T_{\rm B}} - \frac{1}{T_s} \right) \right], \qquad (10)$$

where p_0 is the atmospheric pressure; $T_{\rm B}$ is the boiling temperature; λ_v is the work function of the anode metal atom; and $T_h^0 = T_s$.

If the anode surface temperature exceeds the temperature at which the ionised vapour pressure becomes higher than the external pressure ($p_m^0 \equiv n_e^0 kT_e^0 + \sum_{Z \geq 0} n_{mZ}^0 kT_h^0 - \Delta p \geq p$), the vapour starts expanding (spreading), thus pressing away the external gas. As a result, the near-anode plasma becomes one-component, i.e. containing only the evaporated metal particles. It should be noted that metal boiling temperature $T_{\rm B}$ at the absence of ionisation serves as a boundary temperature of the surface, above which the vapour begins spreading into the atmospheric pressure environment (the saturated vapour pressure is equal to the atmospheric one). The impact on this boundary temperature by the electron pressure was investigated in [22]. It follows from the results obtained that the

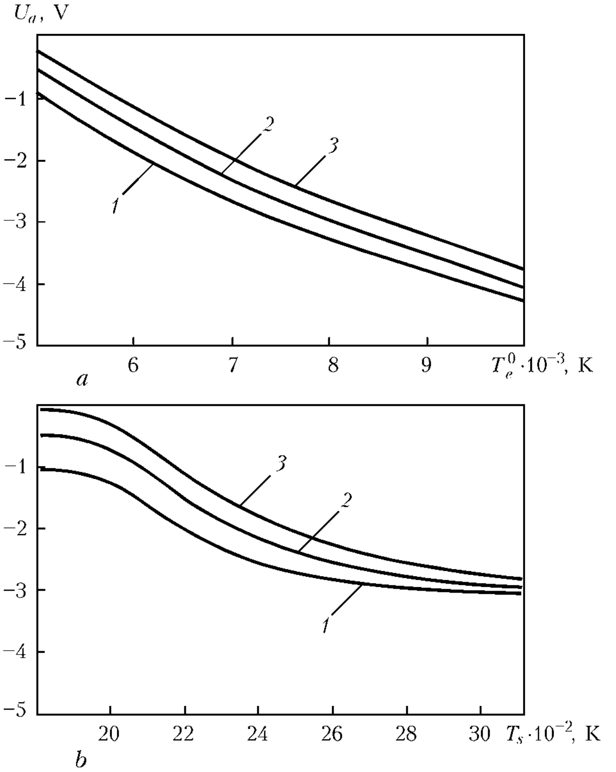

Figure 3. Anode potential drop U_a versus electron temperature in the near-anode plasma layer (*a*) and temperature of its surface (*b*) for steel anode in argon welding: *a* — *1* — j_a = 200; *2* — 500; *3* — 1000 A/cm^2 at T_s = 2472 K; *b* — *1*–*3* — see Figure 3, *a*, but at $T_e^0 = 7\cdot 10^3$ K

anode surface temperature, above which the ionised vapour pressure becomes higher than the atmospheric one, and the diffusion evaporation mode is replaced by the convective one, becomes much lower than $T_{\rm B}$ with increase in T_e^0.

Composition of the near-anode plasma with the convective mode of evaporation of the anode can be calculated using equations (7) through (9), by assuming that $n_{g0}^0 = n_{g1}^0 = 0$ and supplementing this system of equations with the relationships that determine the concentration and temperature of heavy particles of the expanding vapour near the anode surface. To find the values of $\sum_{Z \geq 0} n_{mZ}^0$ and T_h^0, in this case it is possible to use approximate expressions derived in study [28]:

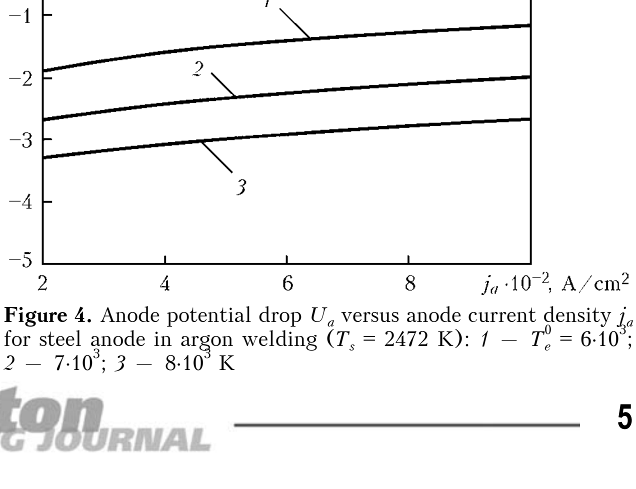

Figure 4. Anode potential drop U_a versus anode current density j_a for steel anode in argon welding (T_s = 2472 K): *1* — $T_e^0 = 6\cdot 10^3$; *2* — $7\cdot 10^3$; *3* — $8\cdot 10^3$ K

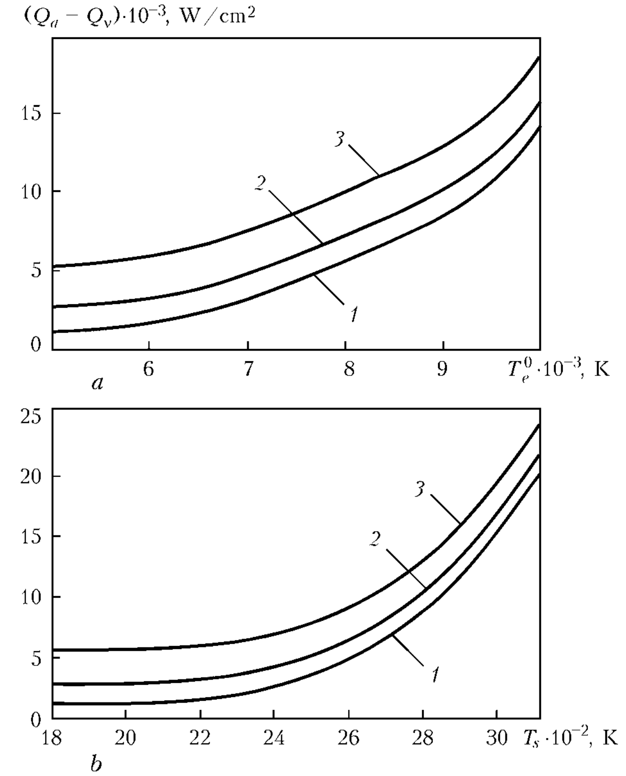

Figure 5. Heat flow on steel anode surface versus electron temperature T_e^0 in the near-anode plasma layer (*a*) and anode surface temperature T_s (*b*) in argon welding: *1–3* — same as in Figure 3

$$\frac{\sum\limits_{Z\ge 0} n^0_{mZ}}{n_s} = \left\{(\gamma_m^2 + \frac{1}{2})\exp(\gamma_m^2)\,[1 - \Phi(\gamma_m)] - \frac{\gamma_m}{\sqrt{\pi}}\right\}\times$$
$$\times\sqrt{\frac{T_s}{T_h^0}} + \frac{1}{2}\left\{1 - \gamma_m\sqrt{\pi}\exp(\gamma_m^2)\,[1 - \Phi(\gamma_m)]\right\}\frac{T_s}{T_h^0}; \quad (11)$$
$$\frac{T_h^0}{T_s} = 1 + \frac{\gamma_m^2\pi}{32}\left(1 - \sqrt{1 + \frac{64}{\gamma_m^2\pi}}\right).$$

Here $n_s = p_s/kT_s$ is the concentration of the saturated vapour corresponding to a given temperature of the anode surface; $\gamma_m = w^0\left(\frac{M_m}{2kT_h^0}\right)^{1/2}$ is the dimensionless vapour velocity; and $\Phi(\gamma_m)$ is the probability integral.

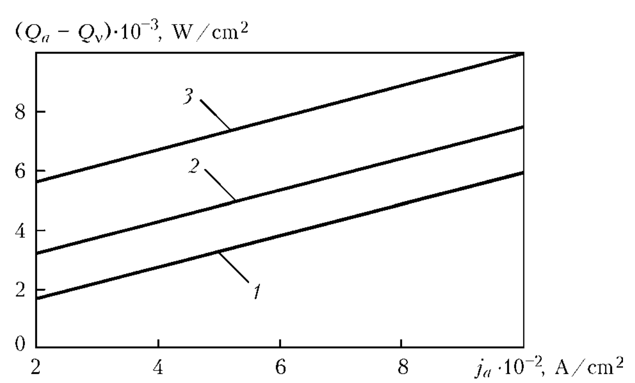

Figure 6. Heat flow to the steel anode surface versus current density j_a in it in argon welding, T_s = 2472 K: *1–3* — see Figure 3

Note that velocity w^0 is an external parameter, and it is determined by conditions of expansion of the vapour in the gas-dynamic region (arc column). To numerically estimate the w^0 value in a case of the subsonic plasma flow, it is possible to use the following approximate expression [28]:

$$w^0 = s^0\left(\frac{p_m^0}{p^0} - 1\right)\Big/\gamma^0\sqrt{1 + \frac{\gamma^0 + 1}{2\gamma^0}\left(\frac{p_m^0}{p^0} - 1\right)}, \quad (12)$$

where s^0 is the local sound velocity, and γ^0 is the adiabatic exponent for the shielding or plasma gas under normal conditions.

The values of the anode potential drop calculated in this way for the conditions characteristic of TIG welding of steel in argon atmosphere are shown in Figure 3. As follows from the calculation data, the anode potential drop in the system under consideration is negative, increasing in its absolute value with growth of the electron temperature of the plasma near the anode and temperature of its surface (see Figure 3), and decreasing to some extent with increase in the anode current density (Figure 4). The U_a value under the conditions considered is within a range of −1 to −4 V.

Consider now the energy transfer processes occurring in the anode region of the electric arc. Heat flow Q_a from the near-anode plasma to the anode surface has the following form:

$$Q_a = Q_e + Q_i, \quad (13)$$

where Q_e and Q_i are the flows of the potential and kinetic energy transferred with electrons and ions, respectively.

Write down the expression for Q_e in the following form [24]:

$$Q_e = j_e\left(\frac{5kT_e^0}{2e} + \varphi_m\right), \quad (14)$$

where φ_m is the work function of electrons for a given metal.

Allowing for the initial energy of ions at the external boundary of the space charge layer, as well as for their extra acceleration in this layer, it can be written down for Q_i

$$Q_i = \sum_{\alpha = m,\, g;\, Z\ge 0} j_{\alpha Z}\left(\overline{\varphi} + \frac{M_\alpha \overline{V_i^2}}{2e} + \frac{1}{Z}\sum_{Z'=1}^{Z} U_{\alpha Z'} - \varphi_m\right), \quad (15)$$

where $\overline{\varphi} \equiv \varphi(\overline{x}) = \varphi^0 - \frac{1}{2}\frac{kT_e^0}{e}$ is the plasma potential at the boundary of the space charge layer

$$\left(\overline{\varphi} = \varphi^0 - \frac{T_e^0 (w^0)^2 \sum\limits_{Z \geq 1} M_m n_{mZ}^0}{8e \sum\limits_{Z \geq 1} (Z T_e^0 + T_h^0) n_{mZ}^0} \times \right.$$

$$\times \left\{ 1 + \sqrt{1 + \frac{4 \sum\limits_{Z \geq 1} k (Z T_e^0 + T_h^0) n_{mZ}^0}{(w^0)^2 \sum\limits_{Z \geq 1} M_m n_{mZ}^0}} \right\}^2$$

for the case of the convective evaporation mode)].

Expression (13) can be written down in the following form:

$$Q_a = j_a V_a, \tag{16}$$

where V_a is the voltage equivalent of heat released at the anode, which always takes a positive value, in contrast to anode potential drop U_a. Allowing for (1), (14) and (15), find

$$V_a = \varphi_m + \frac{j_e}{j_a} \frac{5kT_e^0}{2e} + \sum_{\alpha = m,\, g;\, Z \geq 0} \frac{j_{\alpha Z}}{j_a} \left(\overline{\varphi} + \frac{M_\alpha \overline{V_i^2}}{2e} + \frac{1}{Z} \sum_{Z' = 1}^{Z} U_{\alpha, Z'} \right). \tag{17}$$

In the case of the convective mode of evaporation of the anode metal, energy Q_v removed from the melt surface by the metal vapour flow should be taken into account while considering the energy balance on the anode surface

$$Q_v = \sum_{Z \geq 0} n_{mZ}^0 w^0 \lambda_v. \tag{18}$$

As far as the pressure on the molten anode metal (weld pool) surface is concerned, in the diffusion evaporation mode it is equal to the plasma pressure determined by solving the gas-dynamic equations for the arc column, whereas in the convective evaporation mode this pressure, allowing for the reactive component, can be calculated from the following expression [29]:

$$p_s = p_m^0 \left(1 + \frac{5}{3} \mathrm{M}^2 \right), \tag{19}$$

where $\mathrm{M} \equiv w^0 / s^0$ is the value of the Mach number at a boundary between the anode region and arc column.

Figures 5 and 6 show the calculation results for a heat flow to the anode, considering the energy losses for evaporation under conditions characteristic of TIG welding of steel in argon atmosphere. As follows from the given calculation curves, the values of Q_a grow with increase of the electron temperature in the near-anode plasma layer, current density at the anode and temperature of its surface. This trend is most pronounced in dependence $Q_a - Q_v(T_s)$ (see Figure 5).

Model of the arc column. To describe the processes of heat, mass and charge transfer in the gas-dynamic region of the plasma (in the arc column), which contains atoms and ions of the evaporated anode metal along with particles of the shielding or plasma gas, we use the model of the two-temperature ionisation-equilibrium plasma. The corresponding system of equations written down, e.g. in cylindrical coordinates (see Figure 1) has the following form [2]:

- continuity equation

$$\frac{\partial \rho}{\partial t} + \frac{1}{r} \frac{\partial}{\partial r} (r \rho v) + \frac{\partial}{\partial z} (\rho u) = 0, \tag{20}$$

where ρ is the mass density of the plasma; v and u are the radial and axial components, respectively, of the plasma velocity;

- equations of motion

$$\rho \left(\frac{\partial v}{\partial t} + v \frac{\partial v}{\partial r} + u \frac{\partial v}{\partial z} \right) = -\frac{\partial p}{\partial r} - j_z B_\varphi + \frac{2}{r} \frac{\partial}{\partial r} \left(r \eta \frac{\partial v}{\partial r} \right) + \frac{\partial}{\partial z} \left[\eta \left(\frac{\partial u}{\partial r} + \frac{\partial v}{\partial z} \right) \right] - 2\eta \frac{v}{r^2} - \frac{2}{3} \frac{\partial}{\partial r} \left\{ \eta \left[\frac{1}{r} \frac{\partial (rv)}{\partial r} + \frac{\partial u}{\partial z} \right] \right\}; \tag{21}$$

$$\rho \left(\frac{\partial u}{\partial t} + v \frac{\partial u}{\partial r} + u \frac{\partial u}{\partial z} \right) = -\frac{\partial p}{\partial z} + j_r B_\varphi + 2 \frac{\partial}{\partial z} \left(\eta \frac{\partial u}{\partial z} \right) + \frac{1}{r} \frac{\partial}{\partial r} \left[r \eta \left(\frac{\partial u}{\partial r} + \frac{\partial v}{\partial z} \right) \right] - \frac{2}{3} \frac{\partial}{\partial z} \left\{ \eta \left[\frac{1}{r} \frac{\partial (rv)}{\partial r} + \frac{\partial u}{\partial z} \right] \right\}, \tag{22}$$

where j_z and j_r are the axial and radial components, respectively, of the current density in plasma; B_φ is the azimuthal component of the magnetic induction vector; and η is the coefficient of dynamic viscosity of the plasma;

- energy equations

$$n_e C_{pe} \times \left(\frac{\partial T_e}{\partial t} + v \frac{\partial T_e}{\partial r} + u \frac{\partial T_e}{\partial z} \right) = \frac{1}{r} \frac{\partial}{\partial r} \left(r \chi_e \frac{\partial T_e}{\partial r} \right) + \frac{\partial}{\partial z} \left(\chi_e \frac{\partial T_e}{\partial z} \right) + \frac{k}{e} \left\{ j_r \frac{\partial [(5/2 - \delta) T_e]}{\partial r} + j_z \frac{\partial [(5/2 - \delta) T_e]}{\partial z} \right\} + \frac{j_r^2 + j_z^2}{\sigma} - \psi - \beta (T_e - T_h); \tag{23}$$

$$\rho C_p \left(\frac{\partial T_h}{\partial t} + v \frac{\partial T_h}{\partial r} + u \frac{\partial T_h}{\partial z} \right) = \frac{1}{r} \frac{\partial}{\partial r} \left(r \chi \frac{\partial T_h}{\partial r} \right) + \frac{\partial}{\partial z} \left(\chi \frac{\partial T_h}{\partial z} \right) + \beta (T_e + T_h), \tag{24}$$

where C_{pe} is the specific heat of the electron gas, allowing for the ionisation energy; χ_e is the coefficient of electron thermal conductivity; δ is the constant of thermal diffusion of electrons; σ is the specific electrical conductivity of the plasma; ψ are the energy losses for radiation (approximation of the optically thin plasma); β is the coefficient of heat exchange between electrons and heavy particles; C_p is the specific heat of a heavy component of the plasma (atoms and ions); and χ is the coefficient of thermal conductivity of the heavy component;

- electromagnetic field equations

$$\frac{1}{r}\frac{\partial}{\partial r}\left(r\sigma\frac{\partial\varphi}{\partial r}\right)+\frac{\partial}{\partial z}\left(\sigma\frac{\partial\varphi}{\partial z}\right)=0; \quad (25)$$

$$B_\varphi(r, z)=\frac{\mu^0}{r}\int_0^r j_z(\xi, z)\xi d\xi, \quad (26)$$

where μ^0 is the universal magnetic constant;

$$j_r=-\sigma\frac{\partial\varphi}{\partial r}; \quad j_z=-\sigma\frac{\partial\varphi}{\partial z}. \quad (27)$$

To close the system of equations (20) through (27), it is necessary to determine dependence of thermal-physical characteristics ρ, C_{pe} and C_e, transfer coefficients η, χ_e, χ, δ and σ, heat transfer coefficient β and radiation losses ψ upon the temperature, pressure and composition of the arc plasma. Composition of the multi-component plasma of the arc column with the evaporating anode can be found using equations (7) through (9), which should be supplemented with the following equation of convective diffusion of the metal vapour in the gas-dynamic region:

$$\begin{aligned}\rho\left(\frac{\partial C_m}{\partial t}+v\frac{\partial C_m}{\partial r}+u\frac{\partial C_m}{\partial z}\right)&=\\=\frac{1}{r}\frac{\partial}{\partial r}\left(r\rho D_{m0}\frac{\partial C_m}{\partial r}\right)&+\frac{\partial}{\partial z}\left(\rho D_{m0}\frac{\partial C_m}{\partial z}\right)+\\+\frac{1}{r}\frac{\partial}{\partial r}\left(r\rho\left[\overline{D}_{m1}\frac{\partial C_{m1}}{\partial r}+\overline{D}_{m2}\frac{\partial C_{m2}}{\partial r}\right]\right)&+\\+\frac{\partial}{\partial z}\left(\rho\left[\overline{D}_{m1}\frac{\partial C_{m1}}{\partial z}+\overline{D}_{m2}\frac{\partial C_{m2}}{\partial z}\right]\right)&.\end{aligned} \quad (28)$$

Here $C_m=\frac{M_m\sum_{Z\geq 0}n_{mZ}}{\rho}$ is the relative mass concentration of the metal vapour in the arc column plasma; $C_{m1}=\frac{M_m n_{m1}}{\rho}$ and $C_{m2}=\frac{M_m n_{m2}}{\rho}$ are the relative mass concentrations of metal ions; $\overline{D}_{m1}=D_{m1}-D_{m0}$, $\overline{D}_{m2}=D_{m2}-D_{m0}$, where D_{m0}, D_{m1} and D_{m2} are the coefficients of diffusion of atoms, single- and double-charged ions in the multi-component plasma. Solution of this equation requires evaluation of dependence of diffusion coefficients D_{m0}, D_{m1} and D_m upon the temperature, pressure and composition of the plasma. It should be noted that equation (28), in contrast to the diffusion equation used in study [11], allows for diffusion of ions of the metal vapour.

To solve the system of differential equations (20) through (25) and (28), it is necessary to specify the corresponding initial and boundary conditions. As physical fields in the arc discharge can be set readily enough, the initial distribution of the velocity and temperature is of no fundamental importance. Zero values can be set for the velocity, and the temperature of electrons in the current channel region should provide the plasma conductivity characteristic of the arc discharge. Standard boundary conditions described in detail, e.g. in [2, 9, 17] can be chosen for the boundaries ($r = 0$, $r = R_1$, $z = 0$, $z = L_1$) of the calculation region (see Figure 1). It remains to set conditions at the boundary of the anode and gas-dynamic regions of the plasma.

Let Γ be the boundary of the anode region with the arc column (because of a small thickness of the anode region, anode surface $z = L_1$ can be regarded as Γ). Then the boundary conditions for equations (20) through (22) at this boundary can be set as follows:

$$v_t\Big|_\Gamma=0;$$

$$v_n\Big|_\Gamma=\begin{cases}0 & \text{(diffusion evaporation mode)},\\ w^0 & \text{(convective evaporation mode)}.\end{cases} \quad (29)$$

Here v_t and v_n are the tangential and normal plasma components relative to the anode surface, while to calculate distribution of the w^0 values along the anode surface it is possible to use approximate formula (12). Note that more accurate is to find the w^0 values from equations (11) and condition

$$n_e^0kT_e^0+\sum_{Z\geq 0}n_{mZ}^0kT_h^0-\Delta p=p^0,$$

where p^0 is the distribution of the plasma pressure near the anode along its surface, which is determined by solving the gas-dynamic problem.

Designate the vector of normal to Γ (in a direction of the arc column) as $\vec{n}$. Then the corresponding boundary conditions for equations (23) and (24) can be written down in the following form:

$$\chi_e\frac{\partial T_e}{\partial n}\Big|_\Gamma+\chi\frac{\partial T_h}{\partial n}\Big|_\Gamma+j_a\frac{k}{e}\left(\frac{5}{2}-\delta\right)T_e\Big|_\Gamma=$$
$$=\begin{cases}\varphi^0 j_a+Q_a & \text{(diffusion evaporation mode)},\\ \varphi^0 j_a+Q_a+\varepsilon_v & \text{(convective evaporation mode)};\end{cases} \quad (30)$$

$$T_h\Big|_\Gamma=\begin{cases}T_s & \text{(diffusion evaporation mode)},\\ T_h^0 & \text{(convective evaporation mode)},\end{cases} \quad (31)$$

where ε_v are the energy losses for heating and ionisation of the metal vapour coming to the arc column from the anode surface; T_s is the known distribution of temperature over the anode surface, and distribution of the T_h^0 values at the known distributions of T_s and w^0 can be calculated using the second equation in (11).

As conductivity of the anode metal is much higher, as a rule, than the specific electrical conductivity of the plasma, its surface at a sufficient degree of accuracy can be considered equipotential, by assuming, e.g. that $\varphi_a = 0$. Then the condition at a boundary between the arc column and anode region for equation (25) can be set in the following form:

$$\varphi \Big|_{\Gamma} = \varphi^0, \quad (32)$$

where distribution of the φ^0 values along the anode surface can be calculated from (6).

Finally, write down the boundary conditions for equation (28) in the following form:

$$C_m \Big|_{\Gamma} = \begin{cases} \dfrac{M_m p_s}{\rho^0 k T_s} & \text{(diffusion evaporation mode)}, \\ 1 & \text{(convective evaporation mode)}, \end{cases} \quad (33)$$

where p_s is the distribution of the saturated gas pressure determined at the known distribution of T_s from formula (10); ρ^0 is the distribution of the mass density of the multi-component arc column plasma along the boundary with the anode region.

This exhausts description of the self-consistent mathematical model of physical processes occurring in the multi-component plasma of the anode region and column of the electric arc with the evaporating anode for tungsten-electrode and plasma welding conditions in inert atmosphere.

Therefore, only the self-consistent mathematical model, which allows for interrelation of all physical phenomena accompanying arcing, provides the adequate description of physical processes in column of the welding arc and its anode region, permitting generation of the reliable data on the arcing conditions. Model of the anode region of the arc is an important structural component of this model, responsible for interaction of thermal and electrical processes in the arc column and at the anode (workpiece). Models of properties of the multi-component plasma of the welding arc (ionisation composition, thermodynamic, transport and optical properties), which are determined depending upon the chemical composition of the shielding gas, content of the evaporated anode metal, plasma temperature and ambient pressure, are an indispensable component of the self-consistent model. The input parameters of the self-consistent model should be a set of technological parameters (welding current, shielding gas composition, arc length, etc.), whereas other distributed and integrated characteristics of the arc should be determined as a result of a calculation experiment on the basis of the said model.

1. Hsu, K.S., Etemadi, K., Pfender, E. (1983) Study of the free-burning high-intensity argon arc. *J. of Appl. Phys.*, 54(**3**), 1293–1301.
2. Hsu, K.S., Pfender, E. (1983) Two-temperature modeling of the free-burning high-intensity arc. *Ibid.*, 54(**8**), 4359–4366.
3. Engelsht, V.S., Gurovich, V.Ts., Desyatkov, G.A. et al. (1990) *Low-temperature plasma*. Vol. 1: Theory of electric arc column. Novosibirsk: Nauka.
4. Zhu, P., Lowke, J.J., Morrow, R. et al. (1995) Prediction of anode temperatures of free burning arcs. *J. Phys. D: Appl. Phys.*, **28**, 1369–1376.
5. Jenista, J., Heberlein, J.V.R., Pfender, E. (1997) Numerical model of the anode region of high-current electric arcs. *IEEE Transact. on Plasma Sci.*, 25(**5**), 883–890.
6. Lowke, J.J., Morrow, R., Haidar, J. (1997) A simplified unified theory of arcs and their electrodes. *J. Phys. D: Appl. Phys.*, **30**, 2033–2042.
7. Haidar, J. (1999) Non-equilibrium modeling of transferred arcs. *Ibid.*, **32**, 263–272.
8. Sansonnets, L., Haidar, J., Lowke, J.J. (2000) Prediction of properties of free burning arcs including effects of ambipolar diffusion. *Ibid.*, **33**, 148–157.
9. Fan, H.G., Kovacevic, R. (2004) A unified model of transport phenomena in gas metal arc welding including electrode, arc plasma and molten pool. *Ibid.*, **37**, 2531–2544.
10. Nishiyama, H., Sawada, T., Takana, H. et al. (2006) Computational simulation of arc melting process with complex interactions. *ISIJ Int.*, 46(**5**), 705–711.
11. Hu, J., Tsai, H.L., (2007) Heat and mass transfer in gas metal arc welding. Pt 1: The arc. *Int. J. of Heat and Mass Transfer*, **50**, 833–846.
12. Masquere, M., Freton, P., Gonzalez, J.J. (2007) Theoretical study in two dimensions of the energy transfer between an electric arc and an anode material. *J. Phys. D: Appl. Phys.*, **40**, 432–446.
13. Li He-Ping, Benilov, M.S. (2007) Effect of a near-cathode sheath on heat transfer in high-pressure arc plasmas. *Ibid.*, 2010–2017.
14. Tanaka, M., Yamamoto, K., Tashiro, S. et al. (2008) Metal vapour behaviour in gas tungsten arc thermal plasma during welding. *Welding in the World*, 52(**11/12**), 82–88.
15. Benilov, M.S. (2008) Understanding and modeling plasma-electrode interaction in high-pressure arc discharges: A review. *J. Phys. D: Appl. Phys.*, **41**, 30.
16. Mojzhes, B.Ya., Nemchinsky, V.A. (1972) To the theory of high-pressure arc at refractory cathode. *Zhurnal Teoret. Fiziki*, 42(**5**), 1001–1009.
17. Mojzhes, B.Ya., Nemchinsky, V.A. (1973) To the theory of high-pressure arc at refractory cathode. Pt 2. *Ibid.*, 43(**11**), 2309–2317.
18. Zhukov, M.F., Kozlov, N.P., Pustogarov, A.V. et al. (1982) *Near-electrode processes in arc discharges*. Novosibirsk: Nauka.
19. Wendelstorf, J., Simon, G., Decker, I. et al. (1997) Investigation of cathode spot behaviour of atmospheric argon arcs by mathematical modeling. In: *Proc. of 12th Int. Conf. on Gas Discharges and Their Applications* (Germany, Greifswald, 1997). Vol. 1, 62–65.
20. Nemchinsky, V.A., Perets, L.N. (1977) Near-anode layer of high-pressure high-current arc. *Zhurnal Teoret. Fiziki*, 47(**9**), 1868–1875.
21. Dinulescu, H.A., Pfender, E. (1980) Analysis of the anode boundary layer of high intensity arcs. *J. of Appl. Phys.*, 51(**6**), 3149–3157.
22. Krivtsun, I.V. (2001) Model of evaporation of metal in arc, laser and laser-arc welding. *The Paton Welding J.*, **3**, 2–9.
23. Dyuzhev, G.A., Nemchinsky, V.A., Shkolnik, S.M. et al. (1983) Anode processes in high-current arc discharge. *Khimiya Plazmy*, **10**, 169–209.
24. Sanders, N.A., Pfender, E. (1984) Measurement of anode falls and anode heat transfer in atmospheric pressure high intensity arcs. *J. of Appl. Phys.*, 55(**3**), 714–722.
25. Baksht, F.G., Dyuzhev, G.A., Mitrofanov, N.K. et al. (1973) Probe measurements in low-temperature dense plasma at high ionization degrees. *Zhurnal Teoret. Fiziki*, 43(**12**), 2574–2583.
26. Chen, F. (1967) Electric probes. In: *Diagnostics of plasma*. Moscow: Mir.
27. Griem, H.R. (1962) High-density correction in plasma spectroscopy. *Phys. Rev.*, **128**, 997–1001.
28. Knight, Ch.J. (1979) Theoretical modeling of rapid surface vaporization with back pressure. *AIAA J.*, 17(**5**), 519–523.
29. Arutyunyan, R.V., Baranov, V.Yu., Bolshov, L.A. et al. (1989) *Effect of laser radiation on materials*. Moscow: Nauka.

KINETICS OF CORROSION CRACK GROWTH IN 17G1S PIPE STEEL

V.I. MAKHNENKO, L.I. MARKASHOVA, E.N. BERDNIKOVA, V.M. SHEKERA and **E.M. ONOPRIENKO**
E.O. Paton Electric Welding Institute, NASU, Kiev, Ukraine

Relationship between the rate of growth of corrosion cracks and stress intensity factor was described on the basis of the static corrosion crack resistance diagram. The main working hypothesis that crack growth is of a discrete nature was proved by means of analytical scanning microscopy.

Keywords: *pipe steels, corrosion cracks, diagram of static corrosion resistance, acoustic emission, electron microscopy, hydrogen embrittlement zone*

Corrosion cracks in underground main gas and oil pipelines are the most hazardous defects, which are quite difficult to detect using modern means of in-pipe diagnostics. In this connection, studying the above defects in terms of their initiation and development certainly is of great interest, particularly for specialists, dealing with pipeline repair without taking them out of service, i.e. under pressure, when ranking the detected defects by the urgency of their repair is a critical component of the repair schedule.

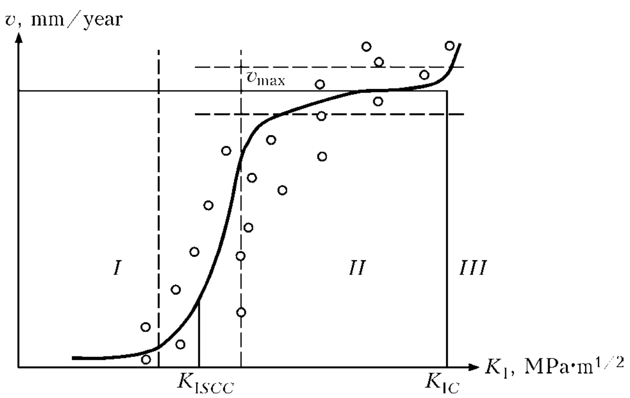

Figure 1. Diagram of static corrosion crack resistance (*I–III*, as well as other designations see in the text)

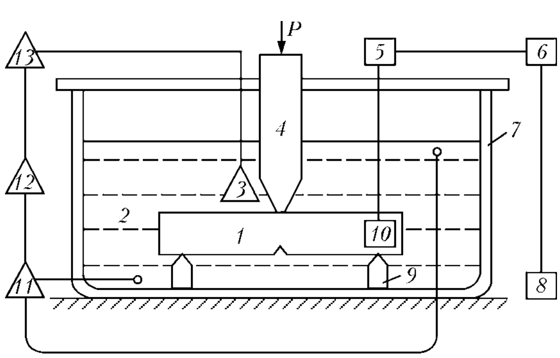

Figure 2. Schematic of sample testing in a pilot unit developed at PWI: *1* — sample; *2* — corrosion medium; *3* — medium temperature sensor; *4* — indenter; *5* — amplifier; *6* — acoustic emission source; *7* — pool; *8* — registering device; *9* — support; *10* — piezoelectric transducer; *11* — medium circulating pump; *12* — medium heater; *13* — temperature regulator

In the general case, corrosion crack development in pipe steels at relative static loads is described by the diagram of static corrosion crack resistance (DSCCR) of this material under the appropriate corrosion-temperature conditions [1]. Figure 1 shows the schematic of such a diagram correlating growth rate v of normal tear corrosion crack with stress intensity factor K_I, determined by the stressed state, crack dimensions and sample geometry. In the general case, three characteristic zones are singled out on the DSCCR (see Figure 1), namely: *I* — $0 < K_I < K_{ISCC}$, where the crack growth rate is relatively low and anode dissolution of sample material in the crack tip is the main mechanism; *II* — $K_{ISCC} < K_I < K_{IC}$ (K_{IC} is the K_I critical value at the given temperature conditions), where crack growth rate is considerable and the mechanism of hydrogen embrittlement of the material in the crack tip prevails; *III* — $K_I < K_{IC}$, where spontaneous crack growth corresponds to brittle fracture. In terms of ranking the detected corrosion crack, or its initiation, zone *II* is very important, determining the safe waiting period in the repair queue.

To obtain data on pipe steel behaviour in water solutions of various soils, PWI uses a procedure de-

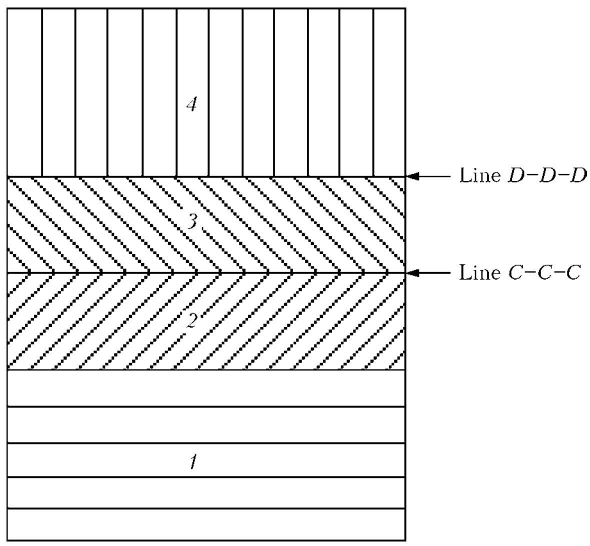

Figure 3. Schematic of characteristic regions on sample fracture surface (*1–4* — see in the text)

scribed in [2, 3] allowing a sufficiently fast acquisition of information on DSCCR parameters in zone *II*, where crack growth proceeds in individual jumps, the presence of which is controlled with an acoustic emission transducer.

The purpose of this work was to confirm by the means of analytical scanning microscopy the working hypothesis of crack growth in the form of individual jumps, part of which are recorded as an acoustic emission signal on the screen and in the computer memory. In view of the selective nature of the process of hydrogenation of metal volumes along the crack front through local dissociation of water solution in this zone, the jumps of crack growth along its front are of a local nature. Their displacement is quite chaotic — in spots along the front, from which layers are formed, determining the average rate of crack front movement.

Given below are the results of examination of fracture surface of 10 × 10 mm cross-section samples with Charpy notch and pre-grown crack. Testing was conducted by three-point bending (Figure 2) in the medium of aqueous extract of sand taken in different regions. Testing time for sample 1 was 740 h, for sample 2 it was 336 h. Samples were made from 17G1S

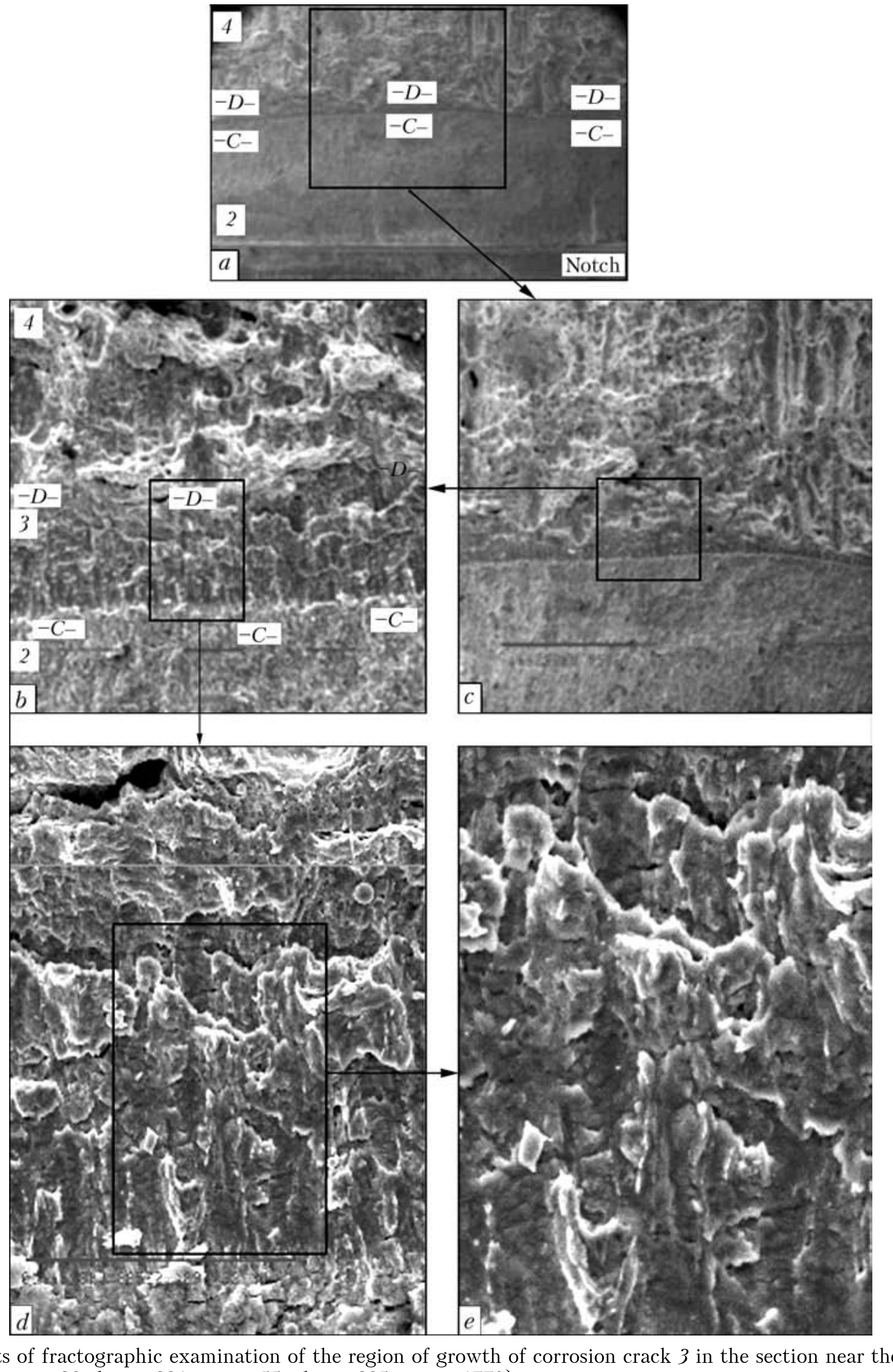

Figure 4. Fragments of fractographic examination of the region of growth of corrosion crack *3* in the section near the region of growth of fatigue crack *2* (*a* — ×28; *b* — ×221; *c* — ×55; *d* — ×885; *e* — ×1770)

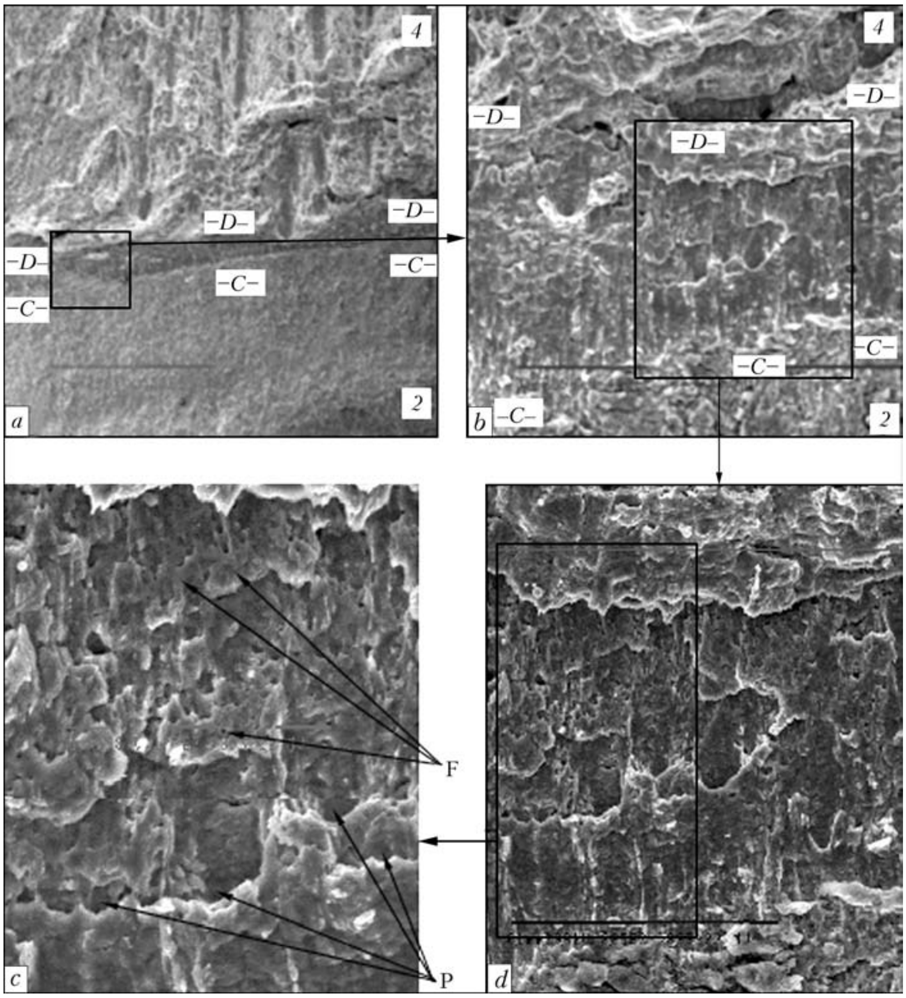

Figure 5. Fragments of fractographic examination of the region of corrosion crack growth near the final fracture region *4* (*a* — ×555; *b* — ×442 *c* — ×1770; *d* — ×885): F — quasibrittle fracture facets; P — flat pit in the extract zone

pipe steel. The following load was selected to achieve $K_I = 25$ MPa·m$^{1/2}$.

Fractures were studied using scanning electron microscope SEM-515 of Philips Company, fitted with energy dispersive spectrometers of «Link» system. Raster images of fracture surface structure enable producing a microimage with greater depth of the field of vision and getting a clearer view of structural details. Before conducting fracture surface examination, they were thoroughly cleaned from corrosion deposits using ultrasound. Four characteristic regions were found on fracture surfaces of each of the studied samples (Figure 3): *1* — notch region; *2* — region of pre-grown fatigue crack; *3* — region of bending deformations (i.e. corrosion crack growth), separating clear-cut region *2* and final fracture region *4*. We are interested in the region separating regions *2* and *4*. In sample 1 it is located between points *D*–*D*–*D* and *C*–*C*–*C* (Figures 4 and 5). Its width is 150–250 μm, which agrees quite well with measurements under the objective of UIM-21 microscope on sample side surfaces before fracture. A system of quasibrittle fracture facets is visible in the corrosion fracture zone, which form the above-mentioned layers (see Figures 4 and 5). Such a pattern was also found in sample 2. However, in connection with shorter testing time (336 h) the extent of the corrosion fracture region decreased to 70 μm, and the quantity of conditional layers of corrosion crack growth was also reduced.

Thus, fracture morphology of tested samples demonstrates the acceptability of the concept of corrosion crack growing jump-like in hydrogen embrittlement zone, not simultaneously over the entire front, but in individual spots, moving quite chaotically along the front, yet still forming growth layers.

1. (2005) *Fracture mechanics and strength of materials*: Refer. Book. Ed. by V.V. Panasyuk. Vol. 7: Reliability and service life of structure elements of heat-and-power units. Ed. by I.M. Dmitrakh. Kyiv: Akademperiodika.
2. (2001) *Fracture mechanics and strength of materials*: Refer. Book. Ed. by Z.T. Nazarchuk. Vol. 5: Nondestructive testing and technical diagnostics. Lviv: G.V. Karpenko FMI.
3. Makhnenko, V.I., Shekera, V.M., Onoprienko, E.M. (2008) Determination of parameters of simplified static corrosion crack resistance diagram for pipe steels in soil corrosion. *The Paton Welding J.*, **10**, 26–30.

NUMERICAL CALCULATION OF THERMAL PROCESSES IN CENTRIFUGAL PLASMA POWDER CLADDING

A.I. SOM[1] and **A.T. ZELNICHENKO**[2]
[1]Plasma-Master Ltd., Kiev, Ukraine
[2]E.O. Paton Electric Welding Institute, NASU, Kiev, Ukraine

In this work, thermal processes running in the thick-walled pipe wall at centrifugal plasma powder cladding were studied by computational experiment method. Temperature fields in each point of the item were calculated, depending on the cladding mode. A measuring stand and procedure for determination of the heat transfer coefficient and effective thermal power were developed.

Keywords: *centrifugal plasma powder cladding, drill pump bushings, circular pool, plasmatron, thermal processes, numerical simulation, calorimetry method*

Centrifugal plasma powder cladding (CPPC) is an efficient technological process of deposition of wear-resistant, corrosion-resistant and antifriction coatings on the surface of various parts [1, 2], including the inner surface of cylindrical parts [3]. CPPC (Figures 1 and 2) is conducted by melting a layer of filler powder by transferred plasma arc at fast rotation of the part (500–1200 rpm). A liquid circular pool forms, which moves together with the plasmatron along the part axis. Presence of a circular pool is a mandatory condition of formation of a metal bond between the deposited metal and substrate. Temperature on the part inner surface in the area of pool location should not be lower than the melting temperature of the filler powder. Its overheating is undesirable, as it leads to base metal dissolution and, as a result, to its mixing with the deposited metal.

Provision of optimum cladding conditions depends on mode parameters, primarily, on arc current and plasmatron movement speed. Diameter of the cylindrical part, its wall thickness and thermophysical properties of base metal, also have a great role. In connection with the fact that visual inspection of the processes of heating, melting and solidification of the filler metal is difficult, selection of optimum mode parameters is highly labour-consuming and costly. Preparation of microsections requires cladding and then cutting several samples of the bushings.

In this work, the method of computational experiment was used to search for optimum CPPC modes. This method was used to study the thermal processes running in the thick-walled pipe wall. Coefficients of heat transfer and effective thermal power required for the computational experiment, were determined using the proposed calculation-experimental method and specially designed measuring stand.

Thermal processes running at CPPC of thick-walled pipes (Figure 3), are described by differential equation of thermal conductivity:

$$c\rho \frac{\partial T}{\partial t} = \frac{1}{r}\frac{\partial}{\partial r}\left(r\lambda \frac{\partial T}{\partial r}\right) + \frac{\partial}{\partial z}\left(\lambda \frac{\partial T}{\partial z}\right), \quad (1)$$
$$R_{\text{in}} < r < R_{\text{o}}, \quad 0 < z < H,$$

where c, ρ, λ is the specific heat capacity, density and coefficient of material heat conductivity; T is the temperature; r, z are the radial and axial coordinates; t is the time; R_{in}, R_{o} are the pipe inner and outer radius; H is the pipe length.

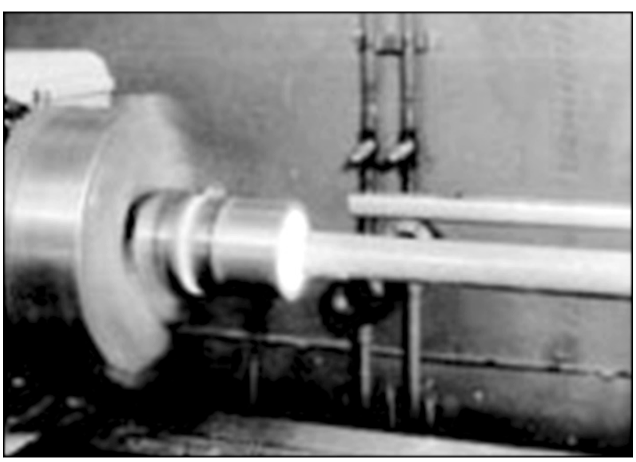

Figure 1. Fragment of a machine for CPPC performance

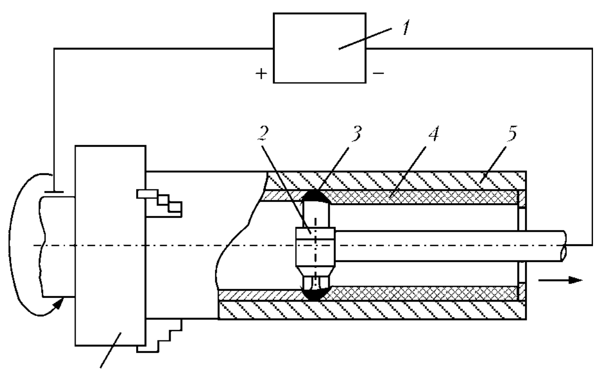

Figure 2. Schematic of the process of CPPC on the part inner surface [1]: *1* — power source; *2* — plasmatron; *3* — circular weld pool; *4* — filler powder; *5* — part; *6* — chuck

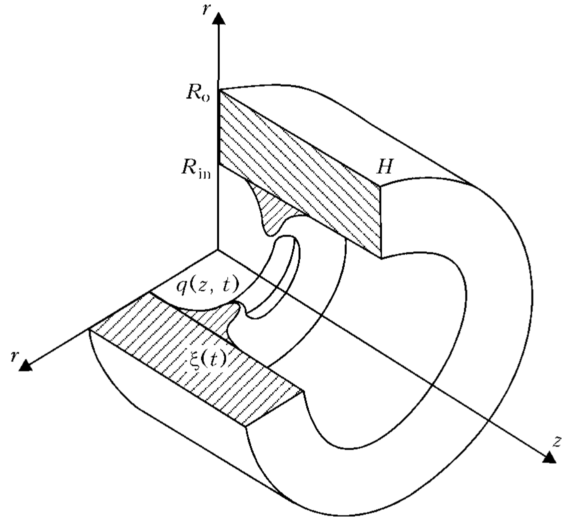

Figure 3. Schematic of bushing heating accepted for calculations

Let us assume that the heat source, moving in the axial direction along the inner surface of rapidly wearing pipe, is distributed by the normal law:

$$q(z,\ t) = q_0 \exp\left[-k(z - \xi(t)^2)\right], \tag{2}$$

where q_0 is the maximum density of the heat flow; k is the concentration coefficient; $\xi(t)$ is the current co-ordinate of the source:

$$\xi(t) = \begin{cases} t_0, & t < t_{in}; \\ t_0 + vt, & t > t_{in}, \end{cases}$$

where t_{in} is the duration of arc impact in the initial point with co-ordinate z_0; v is the speed of source movement.

Total power of heat source Q is connected to value q_0 by the following ratio:

$$q_0 = \frac{Q\sqrt{k/\pi}}{2\pi R_{in}}. \tag{3}$$

Processes of heat transfer and radiation exchange with the environment run on the outer and end face surfaces of the pipe, environment temperature T_{en} being expressed as

$$-\lambda \frac{\partial T}{\partial r}\Big|_{r = R_o} = \alpha_2(T - T_{en}) + \varepsilon\delta(T^4 - T_{en}^4) \tag{4}$$

or

$$-\lambda \frac{\partial T}{\partial r}\Big|_{r = R_o} = \alpha'_2(T - T_{en}), \tag{5}$$

where

$$\alpha'_2 = \alpha_2 + \varepsilon\sigma(T - T_{en})(T^4 - T_{en}^4). \tag{6}$$

Similarly,

$$-\lambda \frac{\partial T}{\partial r}\Big|_{z = 0} = \alpha'_3(T - T_{en}), \tag{7}$$

$$-\lambda \frac{\partial T}{\partial r}\Big|_{z = H} = \alpha'_1(T - T_{en}), \tag{8}$$

where α is the coefficient of heat transfer; ε is the emissivity factor; δ is the Stefan–Boltzmann constant.

In addition to the above-mentioned processes, transfer of heat source energy occurs on the pipe inner surface. Part of this energy is consumed in heating and melting of filler powder. Simulation of the process of powder heating at plasma powder cladding was performed in [4]. In keeping with study [5] the powder layer can be presented in the form of concentrated heat capacity. In this case, the boundary condition on the pipe inner surface has the following form:

$$\lambda \frac{\partial T}{\partial r}\Big|_{r = R_{in}} = q(z,\ t) + \alpha'_4(T - T'_{en}) + C_p \frac{\partial T}{\partial t}\Big|_{r = R_{in}}, \tag{9}$$

where C_p is the heat capacity of the deposited powder layer equal to ρcS; S is the powder layer thickness.

Equation (1) with boundary conditions (4), (5), (7), (8) was solved* by the method of finite differences (taking into account temperature dependence of heat capacity and thermal diffusivity of bushing material). Integration of a two-dimensional equation of heat conductivity was reduced to solving two one-dimensional problems in keeping with local one-dimensional schematic of A.A. Samarsky [6] and procedure of allowing for concentrated heat capacity proposed in work [5].

Proceeding from the developed models and computational algorithm software has been developed, envisaging on-line entry of initial data and graphic representation of results in the form of isotherms and thermal cycles in assigned points. Values of heat transfer coefficient α and effective thermal power q, required for practical calculations, were determined experimentally.

It is known that heat transfer coefficient depends on the shape and dimensions of the surface releasing the heat, its position in space, properties of the environment and other factors. Therefore, experiments on its determination were conducted under the conditions maximum close to the real conditions.

The essence of measurement procedure consisted in the following. A cylinder of steel 20 of 80 mm diameter and 300 mm length was heated in the furnace up to the temperature of 900 °C, mounted in the lathe centers, made to rotate at the speed of 800 rmp and an optical pyrometer was used to record the curves of cylindrical surface cooling (thermally insulating inserts were mounted on cylinder end faces to eliminate heat transfer). Cylinder cooling process was also simulated in the computer. For this purpose equation (1) was solved with the following boundary conditions:

*A.V. Romanenko participated in numerical integration.

$$\lambda \frac{\partial T}{\partial r} \Big|_{r=0} - \lambda \frac{\partial T}{\partial r} \Big|_{r=R_o} = \alpha(T - T_{en}) + \varepsilon\sigma(T^4 - T_{en}^4).$$

A series of calculations were performed with different α values, the results of which were compared with experimental data. For further calculations of thermal processes, value α = 50 W/(m^2·K) was selected, at which the calculated curve was the closest to the experimental one.

As is seen from Figure 4, a slight discrepancy between the experimental and calculated cooling curves of the studied cylinder in the temperature field of 500–700 °C is associated with running of phase transformations in steel, which are not allowed for in model (1)–(9).

Energy characteristics of the plasma arc have been quite well studied for the case of welding, cutting and surfacing [7–10]. However, the results of this work cannot be used for evaluation of effective thermal power of the arc at centrifugal cladding, as item heating in this case has significant special features: the arc runs in a closed space and moves relative to the heated surface at the speed of 3–5 m/s, i.e. by 2–3 orders of magnitude higher than with other plasma processing methods. It should be also taken into account that the effective arc efficiency depends essentially on plasmatron design and its operation mode.

Effective thermal power of the arc was determined by calorimetry, using a thick-walled copper sleeve of 7900 g mass with 80 mm inner diameter and 100 mm length of the cylindrical section as the calorimetric body. The sleeve had a stainless steel stem brazed to its bottom for its fastening in the machine chuck, as well as a case with thermal insulation from basalt fiber. A connector for connection of an external measuring system to two chromel-copel thermocouples caulked into the sleeve, is mounted into the case. The essence of the procedure of determination of the arc effective thermal power was reduced to measurement of the amount of heat, which was gained by the calorimetric body per a unit of arcing time:

$$q_e = \frac{Q_b}{t_r} = \frac{C_{cop} m \Delta T}{t_r},$$

where C_{cop} is the specific heat capacity of copper; m is the calorimetric body weight; ΔT is the temperature increment; t_r is the arc revolution time.

Body temperature was recorded by three-point potentiometer KSP-4 cl. 0.5 with 0–100 °C scale. Arcing time was assigned using the electronic timer, and it was recorded with digital millisecond meter F.291, the signal to which came from current sensor. The signal of arc ignition simultaneously came to the potentiometer. Arc current and voltage were recorded using instruments of magnetoelectric system of cl. 0.2. Experiments were conducted in UD251 unit (Figure 5). A plasmatron with a tungsten electrode was used in the experiments. Plasmatron nozzle diameter

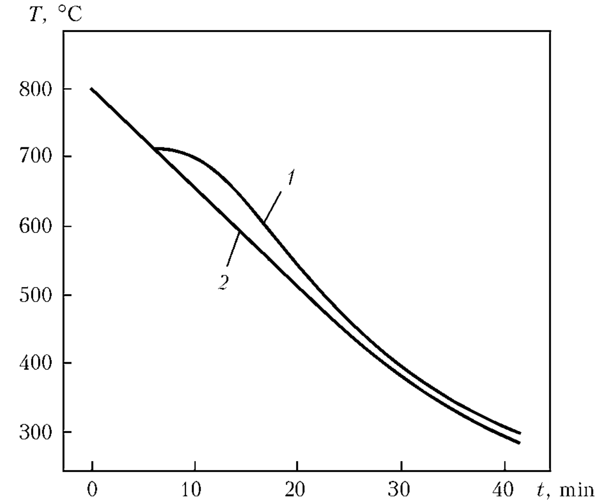

Figure 4. Experimental (*1*) and calculated (*2*) curves of cooling of a cylinder of 80 mm diameter at revolution with the speed of 800 rpm (α = 50 W/(m^2·K))

was 5 mm, nozzle length was 5 mm, depth of electrode immersion into the nozzle was 5 mm, and plasma gas was argon.

Arc parameters were varied within the following ranges: arc current of 300–700 A; arc length of 5–15 mm; plasma gas consumption of 4–20 l/min; calorimeter revolution speed of 50–1250 rpm. When changing one parameter, the others were kept constant and close to optimum ones.

Experimental sequence was as follows. Plasmatron was inserted into the calorimetric body cavity, potentiometer was connected and initial calorimeter curve was recorded. Then, the potentiometer was disconnected, without switching off diagram tape feed to record the moment of arc striking, calorimeter rotation was switched on and the arc was excited. After 6–8 s the arc was switched off, the calorimeter was stopped, the plasmatron was quickly taken out of it and the cover was put on. Potentiometer was simultaneously

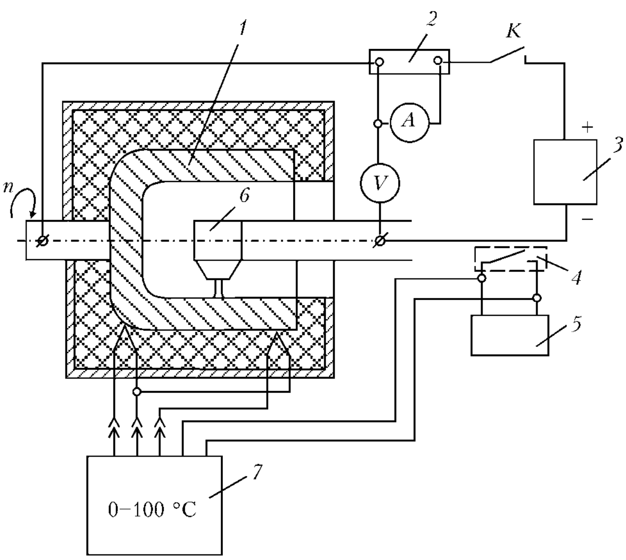

Figure 5. Schematic of UD251 unit for determination of effective thermal power of the arc: *1* — calorimeter; *2* — shunt; *3* — welding rectifier; *4* — current sensor; *5* — millisecond meter; *6* — plasmatron; *7* — potentiometer

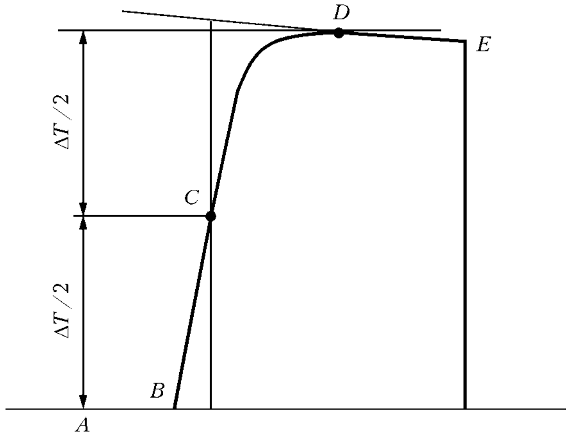

Figure 6. Full cycle of calorimeter temperature variation: *AB* — initial period; *BCD* — main period; *DE* — final period

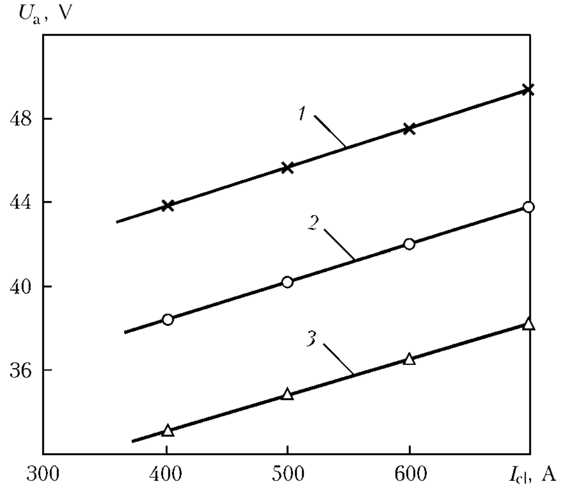

Figure 8. Dependence of arc voltage on cladding current (Q_{melt} = = 10 l/min; n = 800 rpm) at arc length L_a = 15 (*1*), 10 (*2*) and 5 (*3*) mm

connected and the main and final periods of calorimeter temperature curve were recorded. Figure 6 gives an example of recording the full cycle of calorimeter temperature change. Before conducting the next experiment, the calorimeter was cooled to room temperature by an air jet.

Calorimeter heat losses into the environment because of imperfect thermal insulation were allowed for through a correction for heat exchange, which was graphically determined in each experiment by a procedure described in [10]. The actual temperature value, allowing for this correction, was found by extrapolation of the initial and final temperature change by straight lines up to the moment of the main period, when system temperature change will amount to half of the observed change (point *C*). Each experiment was repeated 3–4 times. Some investigation results are given in Figures 7 and 8.

To check the adequacy of the calculation model, heating of outer surface of steel bushing during cladding (bushing inner diameter of 105 mm, outer diameter of 135 mm, length of 250 mm) was experimentally studied. Powder of PG-SR4 grade (GOST 21448–75) with 80–200 μm particle size was used as

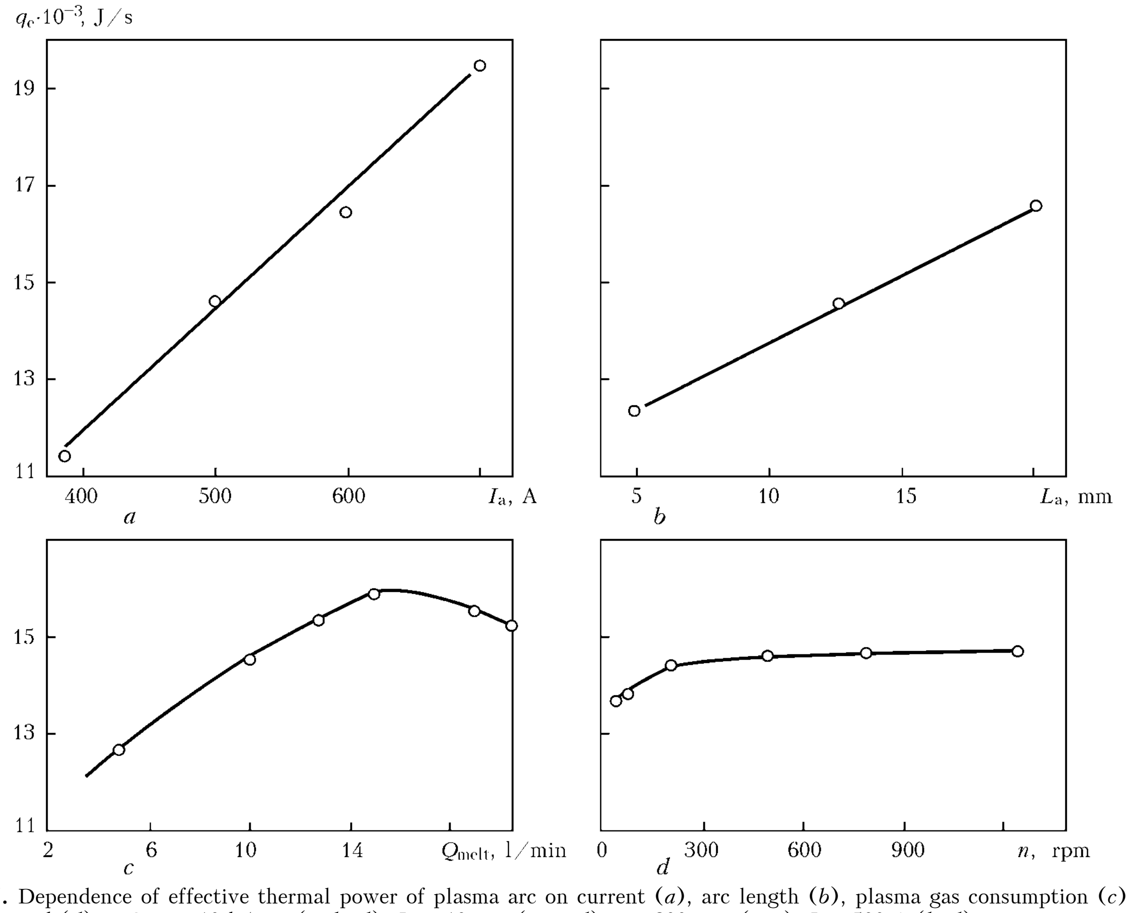

Figure 7. Dependence of effective thermal power of plasma arc on current (*a*), arc length (*b*), plasma gas consumption (*c*) and arc rotation speed (*d*) at Q_{melt} = 10 l/min (*a, b, d*); L_a = 10 mm (*a, c, d*); n = 800 rpm (*a–c*); I_a = 500 A (*b–d*)

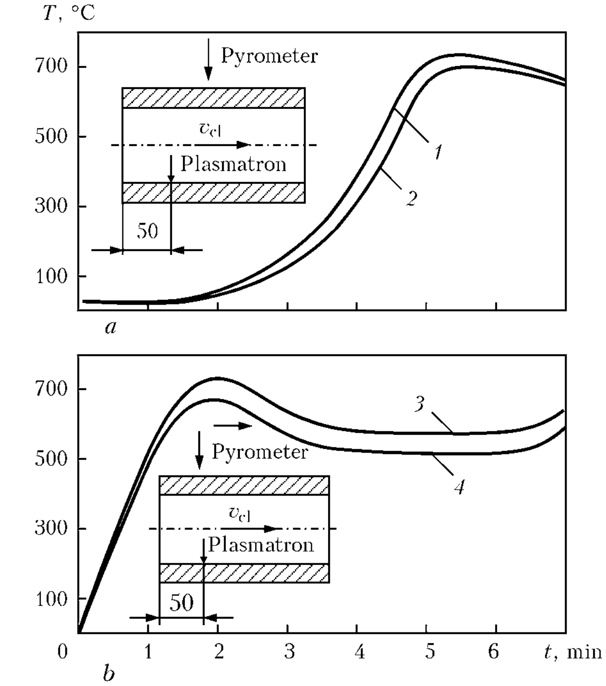

Figure 9. Change of temperature of busing outer surface during cladding in mid-section (*a*) and in sections coinciding with arc axis (*b*): *1, 3* — calculated curves; *2, 4* — experimental curves

filler material. Cladding mode was as follows: arc current of 500 A, speed of plasmatron axial movement of 35.5 mm/min, plasma gas (argon) flow rate of 10 l/min, part rotation speed of 800 rpm, and deposited layer thickness of 2 mm. Cladding was started at 50 mm distance from the bushing left end. The main criteria for selection of cladding mode parameters were good formation of the deposited layer and minimum penetration of base metal (< 3 %).

Temperature was recorded at stationary pyrometer aimed at the bushing middle (Figure 9, *a*) and at its displacement along the bushing in synchronism with the arc (Figure 9, *b*). In the latter case, the pyrometer optical axis and plasmatron axis coincided. Maximum discrepancy of experimental and calculated curves is not more than 7 %.

The developed mathematical model allows calculation of temperatures in any point of the item, depending on cladding mode, thus essentially facilitating selection of optimum mode parameters. For instance, having assigned the temperature of the bushing wall inner surface, it is possible to select the effective thermal power of the arc, speed of plasmatron axial displacement and other mode parameters, ensuring this temperature by successive approximation method (this problem is solved in 10–15 min in the PC). Software allows tracing on the computer monitor the item thermal state at any moment of cladding, which is highly important for the non-stationary process (start and end of cladding, cladding of bushings with variable wall thickness, etc.).

Figure 10 shows as an example the thermal field of a bushing of UNBT-950 drill pump 8 min after the start of cladding. Bushing dimensions are as follows:

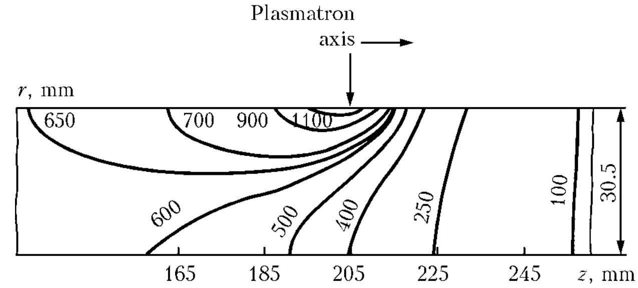

Figure 10. Thermal field (°C) in the wall of bushing of drill pump UNBT-950 8 min after the start of cladding

inner diameter of 154 mm, outer diameter of 215 mm, length of 450 mm. Cladding mode was as follows: arc current of 2 × 600 A; speed of plasmatron axial displacement of 30 mm/min; plasma gas flow rate in each plasmatron of 10 l/min; arc length of 10 mm; thickness of deposited layer of 2.5 mm: speed of part rotation of 800 rpm. Cladding started at 50 mm distance from the bushing left end face. Deposited material was iron-based alloy. Figure 11 shows temperature change on the wall inner and outer surface for the same bushing during the entire cladding cycle. Analysis of the given curves shows that this cladding mode is close to the optimal one. Temperature on the bushing inner wall at the steady-state process is equal to 1240 °C, which is by 100–150 °C higher than the filler powder melting temperature, and, therefore, fu-

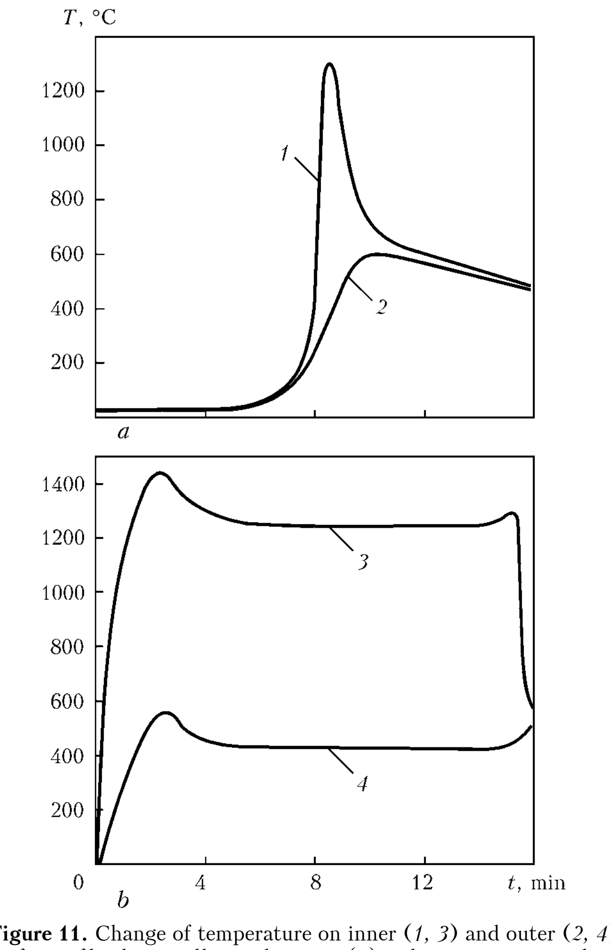

Figure 11. Change of temperature on inner (*1, 3*) and outer (*2, 4*) surfaces of bushing wall in mid-section (*a*) and in sections coinciding with arc axis (*b*)

Figure 12. Transverse macrosection of bushing

sion of the deposited layer with base metal should be ensured. On the other hand, it is lower than base metal melting temperature, so that deposited metal dilution should be minimum. Figure 12 shows a transverse macrosection of the bushing, which confirms the drawn conclusion.

CONCLUSIONS

1. Developed mathematical model of item heating at CPPC quite accurately describes the thermal processes. Conducted series of computational experiments allowed optimization of cladding parameters.

2. Calculation-experimental procedure of determination of the coefficient of heat transfer from the surface of the rotating bushing allowed determination of its value, which is equal to 50 W/(m^2·K).

3. Measuring stand has been developed and a procedure has been proposed for determination of effective heat power at CPPC. Obtained quantitative data have been used with success in engineering calculations.

1. Gladky, P.V., Pereplyotchikov, E.F., Ryabtsev, I.A. (2007) *Plasma cladding*. Kiev: Ekotekhnologiya.
2. Pereplyotchikov, E.F., Ryabtsev, I.A. (2007) *Plasma-powder cladding in armature engineering*. Kiev: Ekotekhnologiya.
3. Gladky, P.V., Som, A.I., Pereplyotchikov, E.F. (1984) Centrifugal plasma cladding. In: *New processes of cladding, properties of deposited metal and transition zone*. Kiev: PWI.
4. Gladky, P.V., Pavlenko, A.V., Zelnichenko, A.T. (1989) Mathematical modeling of powder heating in the arc during plasma cladding. *Avtomatich. Svarka*, **11**, 17–21.
5. Zelnichenko, A.T. (1984) Difference scheme of end-to-end count for equation of heat conductivity with concentrated heat capacity. *Vych. i Prikladn. Matematika*, Issue 53, 57–65.
6. Samarsky, A.A. (1977) *Theory of difference schemes*. Moscow: Nauka.
7. Vajnbojm, D.I., Ratmanova, Zh.V. (1974) Power characteristics of argon arc with different degree of constriction. *Svarochn. Proizvodstvo*, **5**, 1–3.
8. Kulagin, I.D., Nikolaev, A.V. (1960) *Treatment of materials by arc plasma jet*. Moscow: A.A. Bajkov IM.
9. Stikhin, V.A., Patskevich, I.R. (1967) Determination of thermal characteristics of constricted arc. *Svarochn. Proizvodstvo*, **9**, 26–27.
10. Popov, M.M. (1954) *Thermometry and calorimetry*. Moscow: MGU.

FEATURES OF DAMAGEABILITY OF STEAM PIPELINE WELDED JOINTS BY THE CREEP MECHANISM

V.V. DMITRIK and **S.N. BARTASH**
Ukrainian Engineering Pedagogic Academy, Kharkov, Ukraine

Considered are the features of damageability of long-term operating welded joints from heat-resistant pearlitic steels by the creep mechanism. It is shown that damageability of welded joints is a three-stage process, and essentially depends on metal degradation, which is controlled by physicochemical processes occurring in welded joint metal.

Keywords: *arc welding, heat-resistant pearlitic steels, steam pipelines, welded joints, corrosive environment, creep, damageability, physicochemical processes*

High-pressure welded steam pipelines manufactured from heat-resistant pearlitic steels 15Kh1M1F and 12Kh1MF function under the creep and low-cycle fatigue conditions in corrosive environment for a long time. The main constituents of fracture of welded joints are creep, fatigue and fatigue-corrosion cracks and their formation mechanisms have a significant difference [1–4]. Also one of the types of fracture is corrosion damageability. Its role increases during a long-term running of welded joints. From our point of view, an influence of mentioned above constituents on damageability of welded joints should be considered separately for general evaluation of metal degradation.

The purpose of present paper is to specify the features of damageability of long-term operating welded joints of steam pipelines from heat-resistant pearlitic steels by the creep mechanism.

Plastic deformations, a level of which locally can make from 0.5 up to 8.0 % [2], are accumulated in the welded joint metal in the process of running. Creep cracks are formed from the outside of long-term operating welded joints and further crack propagation occurs deep into metal (Figure 1). Such cracks are generated, mainly, along a fusion area or area of incomplete recrystallization of HAZ metal [1, 2, 5, 6]. However, their formation is also noted over the deposited metal in welded joints of steam pipelines with a life time above 200,000 h. A rate of crack propagation significantly depends on structural, chemical and mechanical inhomogeneity of welded joints [2, 6–8] and cracks have, mainly, brittle intergrain character (Figure 2). The presence of structural inhomogeneity provides different intensity of physicochemical processes occurring in the metal of long-term (> 200,000 h) operating welded joints. Volume diffusion of atoms of chromium, manganese, silicon and phosphorus into a thin near-boundary area of grains of α-phase [9], grain boundary diffusion, dislocation displacement by means of creeping and sliding, polygonization of grains of α-phase, $M_3C \to M_7C_3 \to M_{23}C_6 \to M_6C$ carbide reactions, and formation, displacement and coalescence of microdiscontinuities can be referred to such processes. The greatest intensity of such processes is characteristic of structures, classified as rejected or close to them.

Figure 1. Macrosection (×1.5) of the welded joint on steel 12Kh1MF with creep crack in the weld metal (live steam pipeline, 190,000 h running)

From our point of view, a list of rejected structures should be enlarged. Structures consisting of grains of α-phase (Figure 3) with $l/n > 2$, where l is the grain length, and n is the width of grain from 15 μm and more, should be referred to them. Such structures form during welding under higher conditions, for example, in mechanized welding of joints 60 mm thick in CO_2 + + Ar atmosphere with 400 A current. The level of intensity of grain-boundary and volume diffusion will

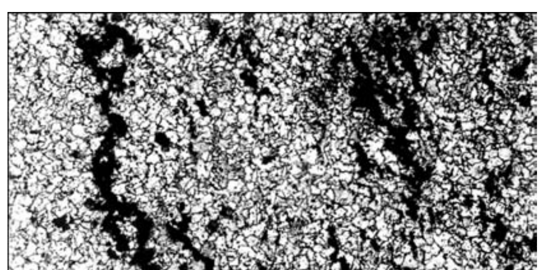

Figure 2. Microstructure (×100) of metal of area with incomplete recrystallization of HAZ of welded joint on steel 12Kh1MF of direct steam pipeline (third stage of damageability, 210,000 h running)

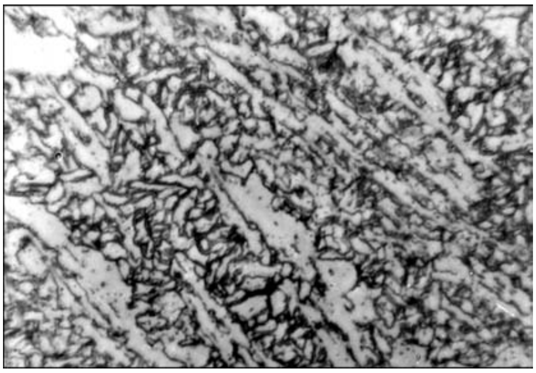

Figure 3. Microstructure (×600) of weld metal of 09KhMF type alloy with elongated grains of α-phase (base metal is steel 15Kh1M1F)

be significantly different under the conditions of anisotropy and cubic singony of grains of α-phase as well as various stage of activation. The presence of grains of elongated shape due to increased intensity of grain-boundary diffusion (in a lesser degree of volume one) provides accelerated formation of the segregations of atoms of chromium, molybdenum, phosphorus and manganese along their boundaries [7, 9]. The rate of solid phase reactions $M_3C \rightarrow M_7C_3 \rightarrow$ $\rightarrow M_{23}C_6 \rightarrow M_6C$ along the boundaries of grains of α-phase significantly (2–3 times) increases at the presence of such segregations in comparison with reactions between the similar precipitates localized along the grain body.

Coarsened equiaxial or length-coarsened grains of α-phase [6] or Widmanstetten ferrite can be locally formed depending on heating conditions in the area of fusion of HAZ to weld metal undergoing welding heating in T_L–T_S temperature zone. Width of fusion area makes up around 0.1–0.2 mm and metal deformation (applicable to 200,000 h of running) can be 2–3 %. In comparison the deformation of base metal (without welding heating) under similar conditions makes up 0.5–0.7 %, respectively, that fulfills the requirements of normative documents.

The shape and dimensions of the area of incomplete recrystallization of HAZ metal with approximate width of 1.2–1.7 mm depend on welding heating and have differences in thickness of welded joints. New decay products of austenite can be presented as pearlite, sorbite, troostite or bainite in this case and differ evidently on structure of the base metal [5, 6, 10–12]. Deformation of the area of metal can make up to 3–5 % and values of weakening from 5 up to 20 % in comparison with the base metal that is close to the data of study [2]. However, no weakening can be observed [6] at the presence of new decay products of austenite such as bainite or troostite. Characteristic feature of the structure of this area is a diversity of grains (Figure 4) and increased structural and chemical inhomogeneity. The physicochemical processes are more intensive in the area of metal in comparison with other areas. Their intensity significantly depends on a type of new decay products of austenite. If new decay products are represented by pearlite the structures are characterized by the greatest processes intensity. In the case of bainite they run with the smallest one. A proof is evidently increased coagulation of $M_{23}C_6$ precipitates along the boundaries of grains of α-phase and formation from such precipitates the chains having elements of uniformity (Figure 5).

Allowable deformation of welded joint metal ($\varepsilon <$ < 1 %) is characterized by a formation of substructure of grains of α-phase [3, 8] and provided by creeping and sliding of the dislocations. The effect of creeping and sliding of dislocations on the process of polygonization at different stages of its realization has the distinctive features that are related to diffusion migration of atoms of chromium, molybdenum, silicon and manganese. Stable VC precipitates uniformly distributed along the body of grains of α-phase and along their boundaries effectively stop moving dislocations. It is reasonable also that the distance between VC, longitudinal dimensions of which are close to 0.7–2.0 nm, remains in the ranges of 80–110 nm.

Stopping of dislocation mobility in the grains of α-phase also takes place with the help of friction forces (Peierls forces) through an interaction of atoms of chromium, molybdenum, vanadium, manganese and silicon with the dislocations, formation of local clus-

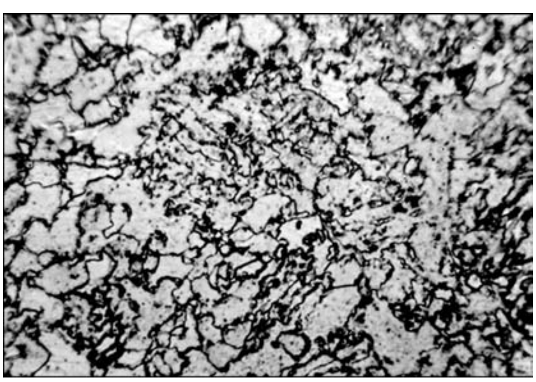

Figure 4. Microstructure (×300) of area with incomplete recrystallization of HAZ metal of welded joints on steel 12Kh1MF of direct steam pipeline (275,637 h running)

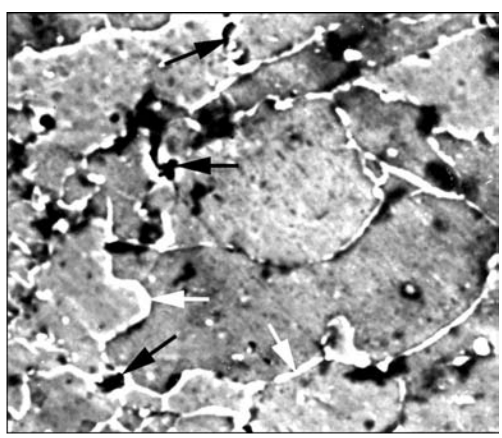

Figure 5. Microstructure (×2500) of area with incomplete recrystallization of HAZ metal with $M_{23}C_6$ precipitates along the boundaries of grains of α-phase (*light arrows*) and pores (*dark*) (the same sample as in Figure 4)

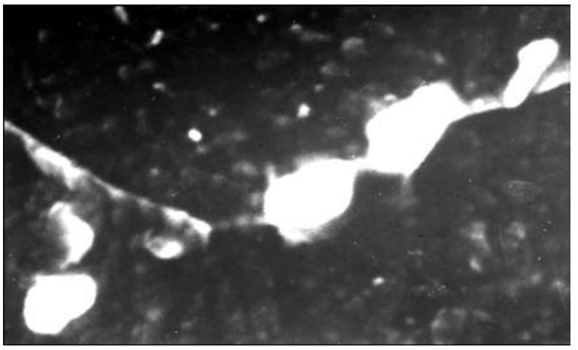

Figure 6. Microstructure (×7500) of area of HAZ with $M_{23}C_6$ precipitates after coalescence

ters of alloying elements in α-phase (of type of Guinier–Preston zones) and atmospheres of impurity atoms around the dislocations as well as barrier effect of the grains and subgrains.

It is convenient to classify the damageability of long-term operating welded joints from heat-resistant pearlitic steels by the creep mechanism as a three-stage process.

The first stage of damageability is characterized by an increase of local segregations of chromium, molybdenum, phosphorus and manganese along the boundaries of grains of α-phase, $M_3C \rightarrow M_7C_3 \rightarrow$ $\rightarrow M_{23}C_6 \rightarrow M_6C$ carbide reactions, coagulation of the precipitates of the first group including coalescence (Figure 6) as well as concentration of such precipitates along the boundaries of grains of α-phase (see Figure 5). It was determined that mainly $M_{23}C_6$ precipitates coagulate and form the chains [10]. Their amount among the carbides forming the chains makes up approximately 70 %, around 15 % of M_7C_3 precipitates and 10 % of $M_{23}C$ and ≤ 5 % of M_6C are determined, respectively.

The coalescence process of microdiscontinuities and formation of creep micropores of around 0.01–0.9 μm in size takes place during the second (incubation) stage of the damageability. Effective identification of such micropores is possible only by means of electron microscopy.

The third stage of damageability (running of less than 250,000 h) is characterized by formation of coalesced and separate micropores of 1–4 μm size as well as formation of creep micro- and macrocracks (see Figure 1). The microcracks and coalesced large micropores having branched form (Figure 7) are located in the direction of main macrocrack. Increased degree of metal deformation in the direction of macrocrack propagation provides its accelerated development. The third stage of damageability has mainly intergrain brittle character and can be well identified by using optical microscopy.

It is reasonable to identify exactly this stage of damageability in proper time and carry out repair using approved technologies [2].

There are cracks and pores in operating welded joints of steam pipelines which at their further running do not obtain propagation though their number can be critical [4, 8, 10]. Stopping in this case can be explained by the presence of a structure adjusting to the direction of cracks and pores propagation and having obviously reduced degradation. However, welded joints involving the critical level of damageability are to be repaired or replaced to avoid their sudden fracture.

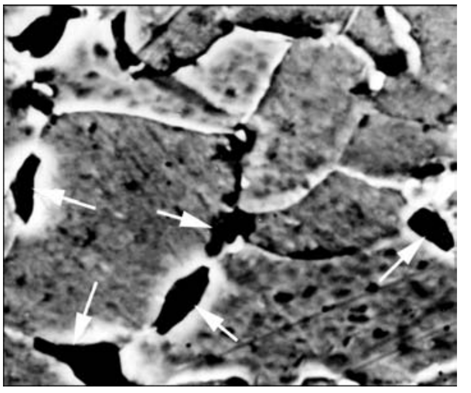

Figure 7. Microstructure (×5000) of area with incomplete recrystallization of HAZ metal of welded joint of direct steam pipeline (*arrows* — micropores along the boundaries of grains of α-phase)

CONCLUSIONS

1. It was experimentally confirmed that the damageability of welded joints by the creep mechanism significantly depends on intensity of physicochemical processes occurring in their metal during long-term operation (running of > 200,000 h).

2. The damageability of long-term operating welded joints from heat-resistant pearlitic steels by the creep mechanism should be considered as a three-stage process.

1. (2005) *Fracture mechanics and strength of materials*: Refer. Book. Ed. by V.V. Panasyuk. Vol. 7: Reliability and service life of structure elements of heat-and-power engineering units. Kyiv: Akademperiodika.
2. Khromchenko, F.A. (2002) *Resource of welded joints of steam pipeline*. Moscow: Mashinostroenie.
3. Dmitrik, V.V., Konyk, A.I. (2005) On concept of pore initiation in welded joints under low-temperature creep. *The Paton Welding J.*, **7**, 24–27.
4. Dmitrik, V.V., Tsaryuk, A.K., Bugaets, A.A. et al. (2006) Evaluation of remaining life of welded joints of pipelines for thermal power plants. *Ibid.*, **2**, 6–10.
5. Kumanin, V.I., Kovaleva, L.A., Alekseev, S.V. (1988) *Service life of metal under creep conditions*. Moscow: Metallurgiya.
6. Dmitrik, V.V. (2000) Structure of welded joints from low-alloyed heat-resistant Cr–Mo–V pearlitic steels. *The Paton Welding J.*, **4**, 26–29.
7. Tsaryuk, A.K. (1999) Peculiarities of phosphorus effect on size of nonmetallic inclusions and properties of heat-resistant steel welds. *Avtomatich. Svarka*, **4**, 26–30.
8. Berezina, T.E., Bugaj, N.V., Trunin, I.I. (1991) *Diagnostics and prediction of life of metal of heat-and-power engineering units*. Kiev: Tekhnika.
9. Dmitrik, V.V., Baumer, V.N. (2007) Carbide phases and damageability of long-term operating welded joints. *Metallofizika, Nov. Tekhnologii*, 29(**7**), 937–948.
10. Utevsky, L.M., Glikman, E.E., Kark, G.S. (1987) *Reversible temper brittleness of steel and iron alloy*. Moscow: Metallurgiya.
11. Dmitrik, V.V., Tsaryuk, A.K., Konyk, A.I. (2008) Carbide phases and damageability of welded joints of steam pipelines under creep conditions. *The Paton Welding J.*, **3**, 28–32.
12. Berezina, T.E. (1986) Structural method for determination of residual life of parts of long-term operating steam pipelines. *Teploenergetika*, **3**, 53–56.

ELIMINATION OF UNDERCUTS IN EBW WITH COMPLETE AND INCOMPLETE PENETRATION

L.A. KRAVCHUK
E.O. Paton Electric Welding Institute, NASU, Kiev, Ukraine

Some peculiarities of formation of crater and weld pool in electron beam welding of 17 mm thick titanium alloy VT20 with complete and incomplete penetration in different positions are considered. Welding schematics and parameters providing defect-free formation of the face and reverse weld beads are given.

Keywords: *electron beam welding. titanium alloys, electron beam, welding schematic, weld pool, defects, crater, face and reverse weld beads*

Principle of faultlessness of critical structures in aircraft and space industry also implies making sound welded joints formed in electron beam welding (EBW) without undercuts on both sides of the weld. The above defects are inadmissible, as they lead to an abrupt lowering of welded joint performance. The problem of undercut elimination on the face and reverse weld bead is particularly urgent in welding of titanium alloys.

It is known that undercuts on the face and reverse weld beads are eliminated by special preparation of the butts to be welded with a technological thickening of 2–3 mm which is mechanically removed after welding [1].

This work is a study of weld formation in EBW with complete and incomplete penetration of high-temperature pseudo α-alloy of titanium VT20 of thickness δ = 17 mm in different positions, in order to prevent undercuts. Selection of VT20 alloy as an object of investigations is due to the fact that it is widely applied in welded structure fabrication.

Composition of VT20 alloy according to GOST 23755–79 includes, wt.%: 5.5–7.5 Al; 0.5–2.0 Mo; 0.8–1.8 V; 1.5–2.5 Zr. Content of specified impurities is as follows, wt.%: 0.18 [O_2]; 0.05 [N_2]; 0.015 [H_2].

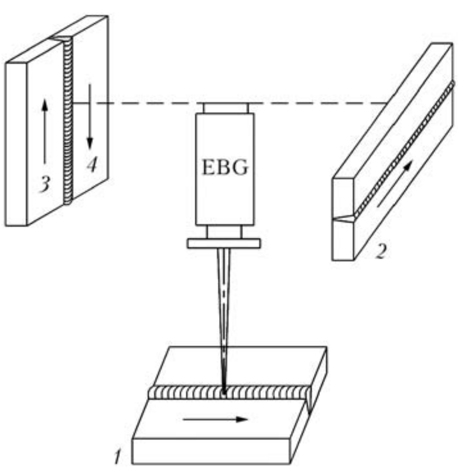

Figure 1. Schematic of downhand (*1*), horizontal (*2*) and vertical (*3, 4*) welding; for *1–4* see the text

Penetration and butt welding of VT20 alloy plates of 17 × 100 × 330 mm size was performed in computer-controlled KL-138 machine of PWI design with power unit based on ELA-60/60 and electron beam gun (EBG), which moves inside the vacuum chamber along linear co-ordinates *x, y, z*. Abutted plates were fixed by short tack-welds from both sides by argon-arc welding, and then they were mounted in an assembly-welding device. The following spatial schematics of welding were selected (Figure 1):

1 — downhand position (vertical electron beam), at which the direction of the gravity force of molten metal in the crater and of the electron beam coincide; EBG moves along *y–y* coordinate;

2 — vertical position (horizontal electron beam), at which the direction of the gravity force is normal to electron beam axis; EBG moves along *y–y* coordinate;

3 — vertical position (horizontal electron beam), at which the direction of the gravity force is normal to electron beam axis and coincides with the direction of molten metal transfer in the crater; EBG moves upwards along *z–z* coordinate;

4 — vertical position (horizontal electron beam), at which the gravity force direction is normal to electron beam axis and is opposite to the direction of molten metal transfer in the crater; EBG moves downwards along *z–z* coordinate.

Electron beam focusing on the surface of plates being welded, electron beam alignment with the butt, visualization of EBW process when cleaning the near-weld zone by a low-power sharply-focused electron beam and making short tack-welds, were performed automatically by a program using «Rastr-6» system with secondary-emission image [2], which provided an alignment accuracy not worse than 0.1 mm and 5 times magnification of the object of observation. Focusing control by image sharpness on the monitor of «Rastr-6» system was checked visually by the brightness of circular sweep of electron beam of diameter d_{circ} = 5 mm with beam current I_b = 10 mA on a copper plate. Discrepancy between the compared values of focusing current at working distance from gun edge

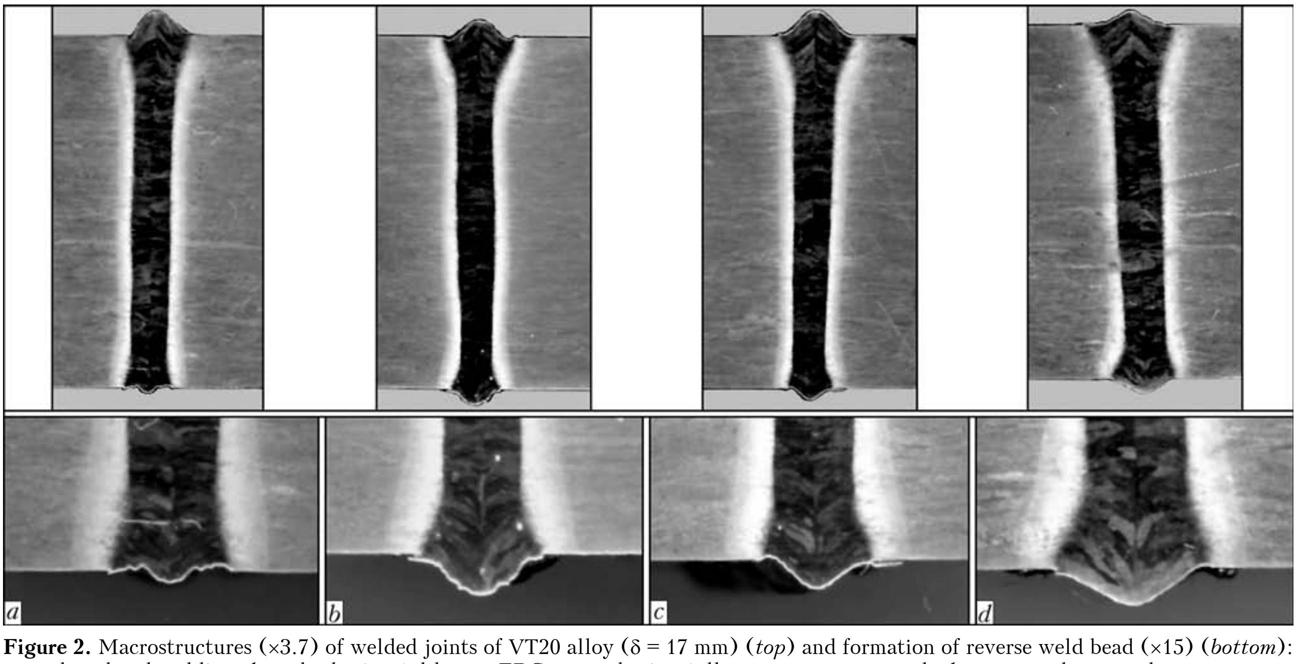

Figure 2. Macrostructures (×3.7) of welded joints of VT20 alloy (δ = 17 mm) (*top*) and formation of reverse weld bead (×15) (*bottom*): *a* — downhand welding; *b* — by horizontal beam, EBG moves horizontally; *c* — same, upward; *d* — same, downward

to the plate l_{work} = 200 mm was equal to ±1 mA on the level of I_f = 550 A, which is quite acceptable for practical application.

Selection of the speed of welding VT20 alloy 17 mm thick with complete penetration in one pass and formation of the face and reverse beads is the starting point of investigations. We found that at welding speed v_w = 100 m/h (27.8 mm/s) the reverse bead forms without undercuts, and undercuts on the face bead are minimum. With increase of welding speed the region of optimum values of electron beam and focusing currents becomes wider, and penetration geometry changes from wedge-like to a shape closer to the cylindrical one.

Various technological sweeps of the electron beam are used, namely around the circumference, ellipse, longitudinal, transverse, along an arc, etc. [3, 4] to produce welds with parallel walls and create conditions for gas escape. From all the sweep types we have applied the transverse sweep, in which the local oscillations of the electron beam occur by the sawtooth law. At beam transverse oscillation amplitude A = = 0.6 mm and frequency of sawtooth oscillations F = = 500 Hz a face bead of VT20 alloy weld with minimum undercuts was produced.

At EBW with a sharply focused electron beam without edge preparation the maximum achievable penetration depth at up to 40 mm thickness of samples is practically the same and does not depend on gravity force F_{gr} of molten weld metal or butt orientation in space [5]. In the case of single-pass butt joints of titanium with complete penetration, in order to achieve sound formation of the reverse weld bead the value of electron beam current is set in the range of I_b = (1.75–2.0)I_0, where I_0 is the beam current, at which the first indications of complete penetration are observed [6].

Proceeding from the above prerequisites, EBW mode was optimized for all the four positions in space, which was not changed further on: accelerating voltage U_{acc} = 60 kW; I_b = 350 mA; v_w = 30 mm/s; I_f = = 553 mA; l_{work} = 200 mm; A = 0.6 mm; F = 500 Hz.

Conducted metallographic analysis of welded joints of VT20 alloy with complete penetration allowed revealing certain peculiarities. As is seen on transverse macrosections, reverse bead formation in EBW by a vertical electron beam in the downhand position is accompanied by formation of undercuts and depressions down to 0.3 mm (Figure 2, *a*), which cannot be removed by cosmetic smoothing because of a lack of metal; weld face bead is formed with up to 2.5 mm excess over the plate surface, and is smoothed by making a repeated cosmetic pass.

In EBW by a horizontal electron beam with EBG displacement along a horizontal (y–y co-ordinate) the weld reverse bead forms without undercuts (Figure 2, *b*), and up to 0.15 mm deep undercuts form on both sides of the weld on the face bead, which are smoothed only by a repeated cosmetic pass.

In EBW by a horizontal electron beam with EBG displacement along z–z co-ordinate upwards (Figure 2, *c*) and downwards (Figure 2, *b*) the weld face and reverse beads form without undercuts; if required they are smoothed by a repeated cosmetic pass.

Thus, proceeding from the requirements to formation of defect-free welded joints of titanium alloy VT20 17 mm thick with complete penetration, the schematics of welding by the horizontal electron beam at EBG displacement upwards, downwards, and horizontally (y–y co-ordinate) without machining of weld reverse bead, limiting ourselves to just the cosmetic pass, can be recommended for commercial production.

Visual observation of the process of crater and weld pool formation in EBW by a horizontal electron

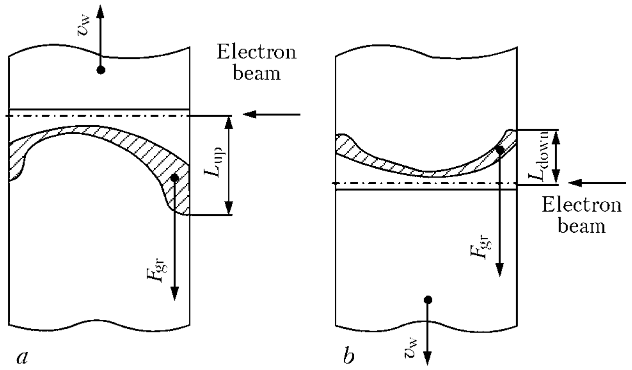

Figure 3. Schematic of formation of a crater and weld pool in the case of EBW by a horizontal beam at EBG movement upwards (*a*) and downwards (*b*)

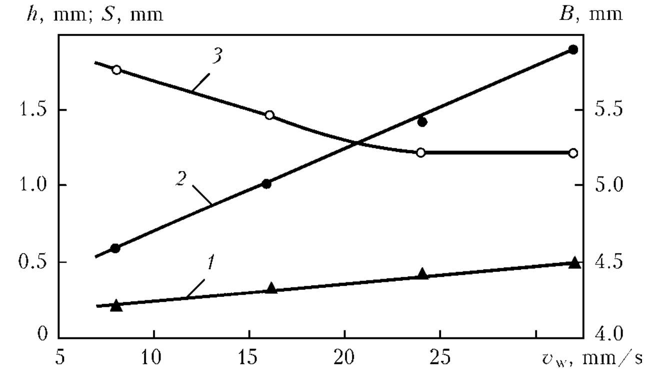

Figure 5. Dependence of undercut depth $S = f(v_w)$ (*1*), face bead reinforcement $h = f(v_w)$ (*2*) and weld width $B = f(v_w)$ (*3*) on welding speed

beam in the cases, when gravity force F_{gr} of molten metal and melt transfer into the solidification zone coincide (EBG moves upwards) or oppose each other (EBG moves downwards), allowed revealing the differences. As shown in Figure 3, weld pool length L_{up} at EBG upward movement is much greater than weld pool length L_{down} at EBG downward movement, i.e. $L_{up} >> L_{down}$. This means that the duration of weld pool existence in the compared schematics is similar, and is determined in the first approximation from ratio $t_w = L/v_w$, where L is the weld pool length.

For a more detailed study of EBW process and confirmation of the validity of $L_{up} >> L_{down}$ ratio video observation was performed using «Rastr-6» system and a special computer program, which allows saving the process of crater and weld pool formation in time. At EBG upward movement no crater collapse takes place, and the liquid metal of the weld pool is regularly transferred into the solidification zone (Figure 4, *a*). At EBG downward displacement a quasi-stationary weld pool forms, and the liquid metal is contained from pouring out by surface tension forces and vapour pressure in the penetration channel (Figure 4, *b*). From the given video materials on formation of the crater and weld pool it is seen that $L_{up} >> L_{down}$ ratio is fulfilled with up to several times difference in weld pool length.

Direction of gravity force of molten metal and metal transfer into the solidification zone also significantly influences formation of weld reinforcement (face bead) and undercuts in EBW of titanium alloys by a horizontal beam with incomplete penetration. A series of butt welds and beads deposited on solid metal on titanium alloy VT20 (δ = 17 mm) showed that at EBW by a horizontal beam by the upward schematic with welding speed variation in the range v_w = 8–32 mm/s and preservation of a constant heat input of the electron beam q/v weld face bead height and undercut depth on both sides of the weld increase linearly; with increase of welding speed the face bead width decreases non-linearly and is stabilized at v_w = = 24 mm/s (Figure 5).

In the case of EBW by a horizontal beam with incomplete penetration of VT20 alloy (δ = 17 mm) by the by downward schematic with variation of welding speed (v_w = 8–32 mm/s) and preservation of a constant heat input q/v the face bead forms in a regular and uniform manner along the entire weld length with a small reinforcement and without undercuts (Figure 6).

Thus, at EBW of titanium alloy VT20 by a horizontal beam with incomplete penetration formation of welded joints without undercuts on the weld face bead is achieved only when the downward schematic is used. It is recommended to apply this technique in commercial production in those cases, when machining of weld face bead is inadmissible.

It should be noted that all the samples and mock-ups of products of VT20 alloy (δ = 17 mm) with complete penetration welded in the above EBW mode

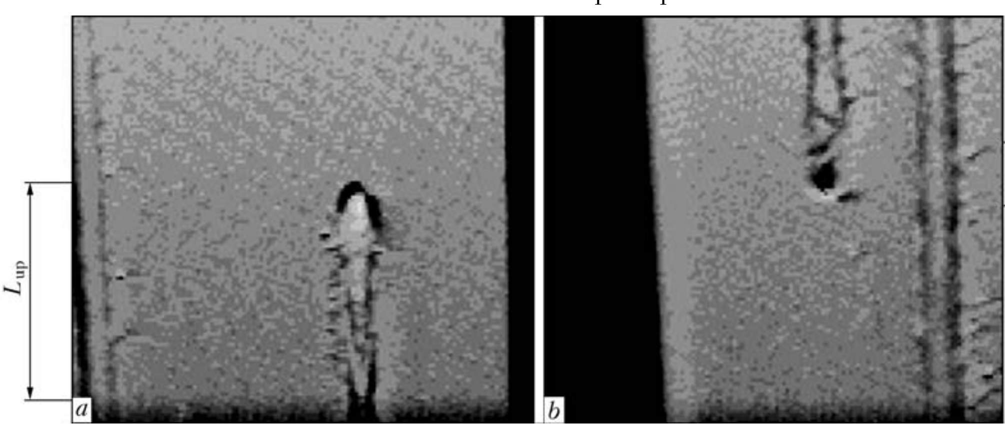

Figure 4. Videoimage of crater and weld pool in EBW by a horizontal beam of VT20 alloy (δ = 17 mm); for *a*, *b* — see Figure 3

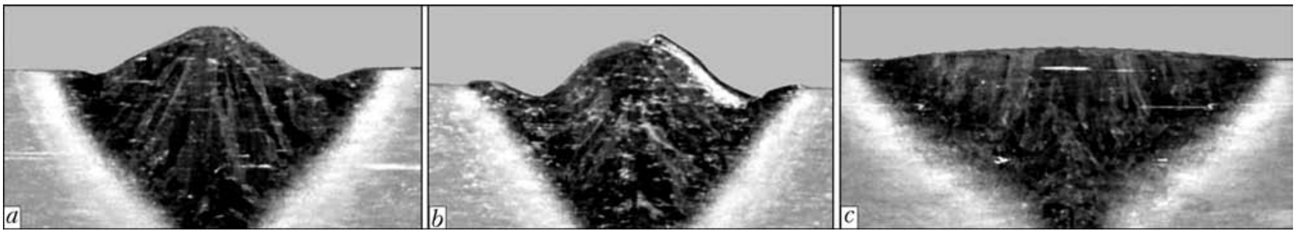

Figure 6. Macrostructure (×8) of welded joints of VT20 alloy with incomplete penetration and weld face bead: *a, b* — EBW by horizontal beam by upward schematic at v_w = 8 and 32 mm/s, respectively; *c* — downward schematic, v_w = 8 mm/s

have passed X-ray inspection. No defects in the form of cavities, pores, undercuts or lacks-of-fusion were found.

Defect-free formation of welded joints of titanium alloy VT20 (δ = 17 mm) produced in EBW with complete penetration, is achieved by the schematic of welding with a horizontal electron beam with EBG movement downwards, upwards and horizontally.

Thus, the recommended welding schematics and developed modes of EBW of titanium alloy VT20 allow eliminating machining of the face and reverse weld beads.

1. Stocker, G. (1974) Erfahrungen beim Elektronenstrahlschweissen dickwandiger Bauteile aus der Titanlegierung Ti–6Al–4V geglueht. *Schweissen und Schneiden*, 26(**9**), 91–93.
2. Paton, B.E., Nazarenko, O.K., Nesterenkov, V.M. et al. (2004) Computer control of electron beam welding with multi-coordinate displacements of the gun and workpiece. *The Paton Welding J.*, **5**, 2–5.
3. Wiesner, P., Ehrhard, H. (1983) Elektronenstrahlschweissen mit Strahlpendeln. *ZIS Mitteilungen*, 25(**1**), 17–28.
4. Friedel, K.P., Arata, Y. (1980) Preliminary evaluation of root defects elimination methods in partial penetration EB welding. In: *Proc. of Int. Conf. on Welding Research* (Oct. 27–29, 1980, Osaka), Section F.
5. Paton, B.E., Nazarenko, O.K., Lokshin, V.E. et al. (1972) Peculiarities of electron beam welding in different spatial positions. *Avtomatich. Svarka*, **6**, 1–4.
6. Nudelman, Ya.B., Zadery, B.A. (1988) Weld formation in electron beam welding of up to 25 mm thick titanium alloys. *Ibid.*, **5**, 29–30.

INFLUENCE OF MAIN TECHNOLOGICAL PARAMETERS OF THE PLASMA CLADDING PROCESS ON PROPERTIES OF COMPOSITE DEPOSITED METAL

A.I. BELY

E.O. Paton Electric Welding Institute, NASU, Kiev, Ukraine

The paper presents results of experiments on determination of the influence of technological parameters of the process of plasma cladding of composite alloys using filler material in the form of flux-cored strip consisting of a metal sheath and core, on formation and wear resistance of deposited metal. The strip core contained hard-alloy grains based on fused tungsten carbides.

Keywords: *plasma cladding, filler material, wear resistance, composite alloy, reinforcing particles, strip tungsten carbide (relite)*

The process of plasma cladding of composite alloys [1, 2] using filler material in the form of the flux-cored strip, which consists of a metal sheath and core of grains of fused tungsten carbide and fine-dispersed charge of alloying and deoxidizing components (strip relite), should provide a wear-resistant layer with optimal geometry at a high quality of formation and wear resistance (Figure 1).

It is well-known that wear resistance of composite alloy is determined by the concentration and wear resistance of reinforcing particles (fused tungsten carbide) in deposited metal and ability of its matrix to hold these particles. As a rule, the said properties of the wear-resistant layer depend on the cladding technology and level of dissolution of a reinforcing particle in the process of cladding. Dissolution of grains of tungsten carbides results in reduction of the concentration of the wear-resistant phase and increase of saturation of the matrix with tungsten and carbon, this increasing the probability of its embrittlement and decreasing wear resistance of alloy as a whole [3].

The paper presents results of investigations into the influence of main technological parameters of the plasma cladding process on the quality of formation, structure and wear resistance of the composite deposited metal.

Ranges of the main technological indicators of the plasma cladding process were as follows:

transferred arc current I_a, A	180–340
cladding speed v_{cl}, m/h	4–20
filler metal feed speed v_f, m/h	10–50

Cladding was carried out on low-carbon steel samples measuring 150 × 70 × 20 mm. The following conditions were used as the initial ones: I_a = 220 A, U = 34 V, v_{cl} = 8 m/h, v_f = 20 m/h, plasma gas flow

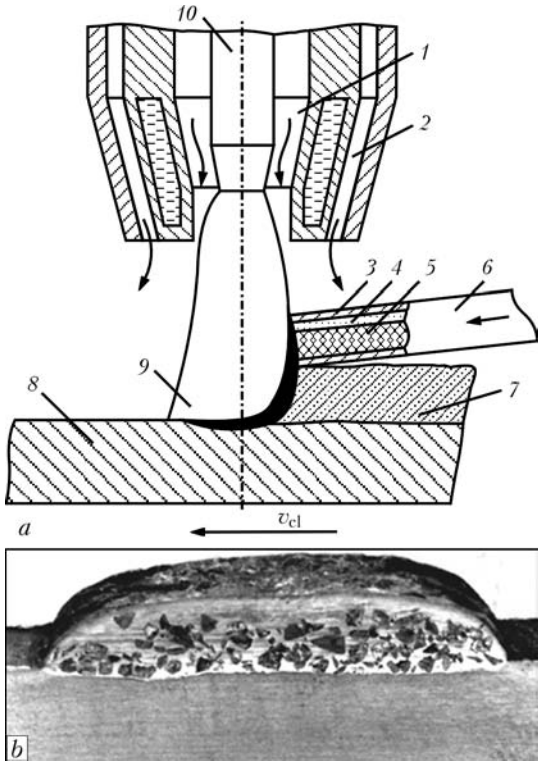

Figure 1. Scheme of plasma cladding of composite alloys using strip relite as a filler material (*a*) (*1, 2* — plasma and shielding gas, respectively; *3* — sheath; *4* — fine charge; *5* — reinforcing particles; *6* — filler material; *7* — deposited layer; *8* — sample; *9* — plasma arc column; *10* — electrode) and macrosection of the deposited bead (*b*)

rate — 2 l/min, shielding gas flow rate — 6 l/min, amplitude of oscillation of the plasma torch — 25 mm, and frequency of oscillation of the plasma torch — 35 min^{-1}. Strip relite AN-LZP-9-8 [4] was used as a filler material.

The evaluation of the influence of parameters of the cladding process on properties of the deposited metal was carried out at several values of each parameter, the rest of the parameters being kept constant.

The quality of the deposited metal was evaluated by the wear test procedure for composite alloys over a fixed abrasive (sliding path 30 m, sliding speed 0.5 m/s) at one value of the contact pressure equal to 1.055 MPa [3]. Three samples of each deposited metal obtained at fixed conditions of the process of cladding were tested, and the arithmetic mean of the value of wear of the tested samples was taken as an indicator.

It was determined experimentally (Figure 2) that the plasma arc current has the greatest influence on wear W of composite metal. Increase in the current is accompanied by increase in the time of existence of molten pool and its volume.

The time of contact of the molten matrix phase of alloy and reinforcing particles increases with increase in the time of existence of the molten pool, this resulting in growth of the degree of their dissolution, decrease in concentration of the wear-resistant phase, and, hence, reduction of wear resistance of the composite alloy as a whole.

The cladding speed in the investigated range of the process parameters has no noticeable influence on wear resistance values. However, its further increase leads to deterioration of formation of the deposited bead, resulting in the lack of fusion, disappearance of the common molten pool, reduction of the level of base metal penetration, and impossibility of performing the process.

Minimal values of the filler material feed speed lead to low performance of the deposited metal. In this case, the molten pool of a big volume is formed at a fixed cladding current value, this resulting in dissolution of the reinforcing particles and reduction of wear resistance of the alloy.

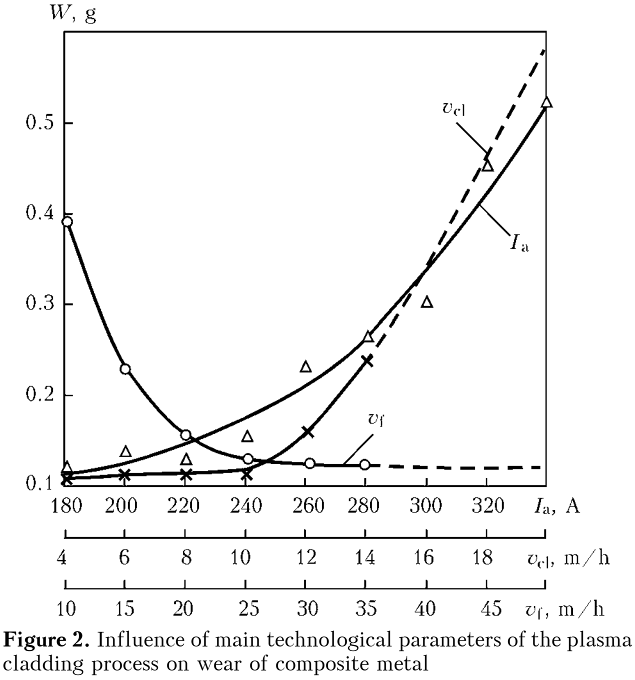

Figure 2. Influence of main technological parameters of the plasma cladding process on wear of composite metal

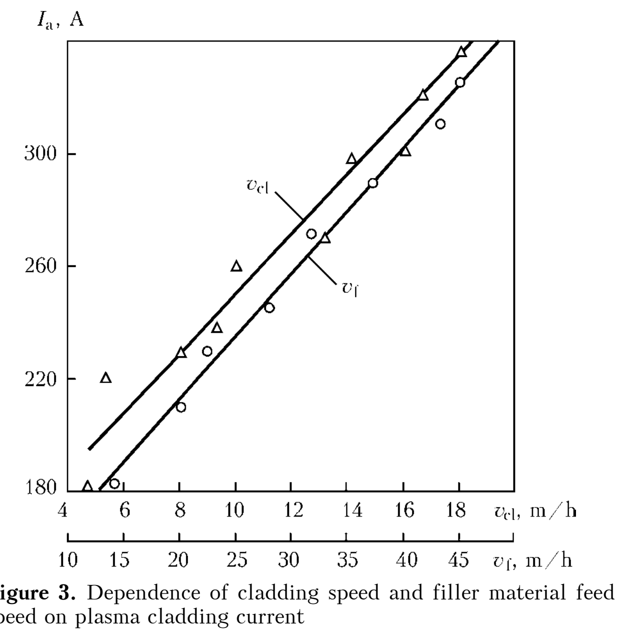

Figure 3. Dependence of cladding speed and filler material feed speed on plasma cladding current

Increase of the filler metal feed speed leads to increase of the amount of the filler material fed to the plasma arc, which is to be melted, this requiring a higher amount of heat.

As a result, dissolution of the reinforcing particles decreases, formation of the deposited bead improves, and its wear resistance grows. Exceeding the optimal filler metal feed speed leads to reduction of the efficiency of melting of the incoming filler metal and the base metal, this resulting in termination of cladding process (see Figure 2, the region is shown by dashed line).

Thus, for every standard size of the filler material (width and thickness of the strip relite) there is an optimal range of main technological parameters of the cladding process (current intensity, cladding speed and filler metal feed speed), which are interrelated to each other, and are of critical importance for formation and geometry of the deposited beads.

There is a close connection between the cladding speed, filler material feed speed and plasma arc current (Figure 3). Increasing the cladding speed is usually accompanied by growth of the filler material feed speed for maintaining constant size of the deposited bead. For this, it is necessary to increase the plasma arc current in order to provide melting of a bigger amount of the filler material.

Therefore, selection of optimal conditions for plasma cladding is reduced to determination of the current, cladding speed and filler material feed speed. Values of the rest of the process parameters (plasma gas and shielding gas flow rates, arc voltage etc.) have a minor influence on formation of the wear-resistant alloy and are to be maintained within the above ranges.

The influence of main technological parameters of the process of plasma cladding on dimensions and shape of the deposited beads is shown in Figure 4.

According to the experience, thickness of the layer of the deposited beads should be no more than 4–5 mm, otherwise a sudden decrease of the cladding quality will take place, which shows up in insignificant dissolution of the reinforcing particles. The minimal thickness of the deposited metal, which has been obtained by using the strip relite with the reinforcing grains of 0.40–0.63 mm size, is around 0.7 mm. However, it is very difficult to perform such a cladding process, the main role being given to the quality of the filler material.

Thus, the main technological parameters of the plasma cladding process by using the strip relite and their influence on the quality of composite deposited metal were determined. It was found that the plasma arc current has the highest influence on wear resistance of the composite alloy.

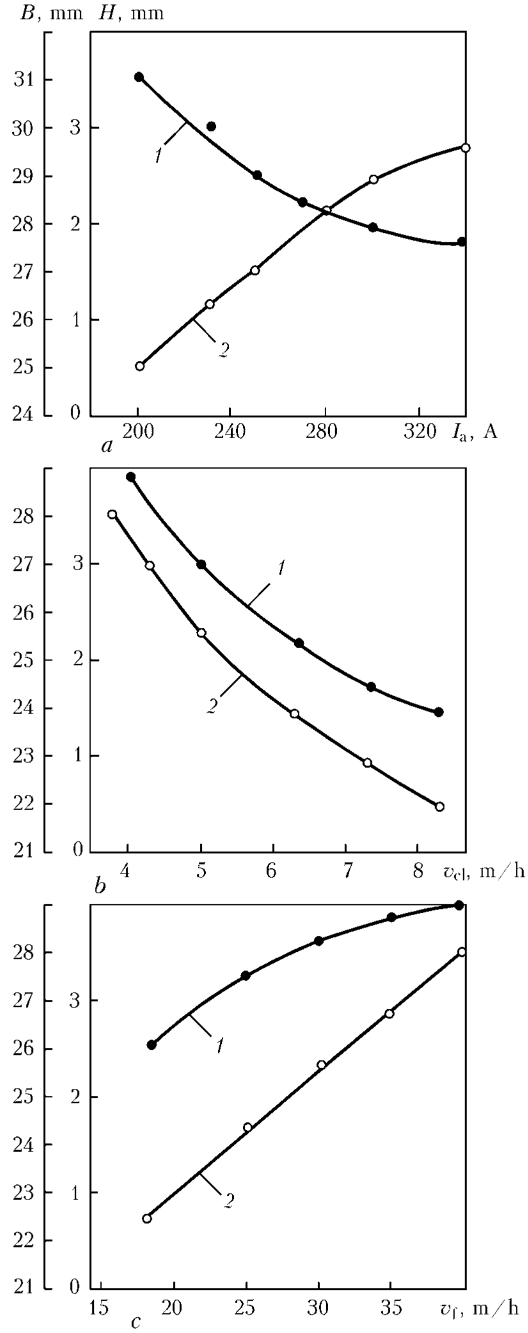

Figure 4. Influence of plasma arc current (*a*), cladding speed (*b*) and filler material feed speed (*c*) on height *H* (*1*) and width *B* (*2*) of deposited bead

1. Gladky, P.V., Pereplyotchikov, E.F., Ryabtsev, I.A. (2007) *Plasma cladding*. Kiev: Ekotekhnologiya.
2. (1990) *Method of plasma cladding of composite alloys*. USSR author's cert. 1622097. Publ. 22.09.1990.
3. Bely, A.I. (2006) *Materials and technology of cladding of drill pipe elements with composite alloy*: Syn. of Thesis for Cand. of Techn. Sci. Degree. Kiev: PWI.
4. *TU IES 677–88*: Strip relite AN-LZP.

MAGNETICALLY-IMPELLED ARC BUTT WELDING OF PARTS OF AUTOMOBILE RANGE OF PRODUCTS

S.I. KUCHUK-YATSENKO, V.S. KACHINSKY, V.Yu. IGNATENKO, E.I. GONCHARENKO and **M.P. KOVAL**
E.O. Paton Electric Welding Institute, NASU, Kiev, Ukraine

Peculiarities of magnetically-impelled arc butt welding of parts of the automobile range of products, including compact hollow parts of steering rod, shock-absorber and torque rod, are described. Results of metallographic examinations as well as evaluation of mechanical tests, proving the high quality of welded joints, are presented.

Keywords: *magnetically-impelled arc, press welding, automobile parts, joint formation, technology of welding*

High-efficiency and energy-saving processes of welding, assuring the good quality of parts being manufactured, and also allowing achievement of the higher labour productivity find a wide spreading at the automobile plants.

At the E.O. Paton Electric Welding Institute of the NAS of Ukraine the technology and equipment (welding machines MD102 and MD105) have been developed for the magnetically-impelled arc butt (MIAB) welding, which are widely used in the automobile industry of Ukraine. Since 1994 the MIAB-welded pneumatic springs and shock-absorbers (Figure 1) are manufactured at CJSC «Krasnodon Works «Avtoagregat» [1–3]. During this period more than 4 million of welded joints were made.

On the basis of gained multi-year experience of MIAB welding the following main advantages of this technology can be outlined: high efficiency under the conditions of mass production; low time of welding as compared with other processes; minimum consumption of part material for heating and upsetting; air-tightness of welded joints; absence of welding consumables and shielding gas; high strength properties of welded joints at the level of those of parent metal.

Table 1. Technical characteristics of machines for pipe welding

Machine type	Diameter of pipes, mm	Wall thickness, mm	Upsetting force, kN	Consumed power, kV·A	Mass, kg
MD101	10–51	1–4	40	30	230
MD1	18–61	1–6	60	45	190

Over the recent years the technology of MIAB welding of the new generation of parts of automobile industry has been developed at the E.O. Paton Electric Welding Institute. The investigations were aimed at the development of a relatively not expensive high-efficiency process of the MIAB welding for manufacture of automobile parts under the conditions of mass production.

Weldability of compact hollow automobile parts, such as a steering rod of ∅22 × 2.2 mm, shock-absorber of ∅40 × 2.2 mm and torque rod of ∅34 × 6 mm, was investigated. Basic requirements, specified for the work, are to develop the highly-efficiency process of welding for its application in mass automobile production with guaranteed mechanical properties of welded joint at the level of characteristics of the part parent metal.

The works were performed using welding machines MD101 and MD1 (Figure 2), technical characteristics of which are given in Table 1 (the welding efficiency is 60 joint/h), and chemical composition of parts is presented in Table 2.

Main technological parameters of welding the parts of steering rod, shock-absorber and torque rod are presented in Table 3.

Mechanical tests of welded joints were performed in accordance with procedures accepted at the automobile plants. They include full-scale rupture tests and also local bending of segments of circumferential welds.

Metallographic examinations of welded joints of parts of steering rod and shock-absorber were carried out in the LECO device M 400 at 1 N load and 100 μm pitch. To reveal the microstructure of welded joint,

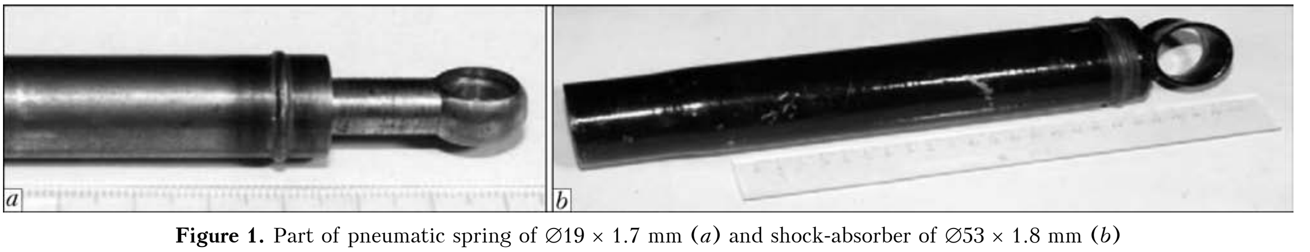

Figure 1. Part of pneumatic spring of ∅19 × 1.7 mm (*a*) and shock-absorber of ∅53 × 1.8 mm (*b*)

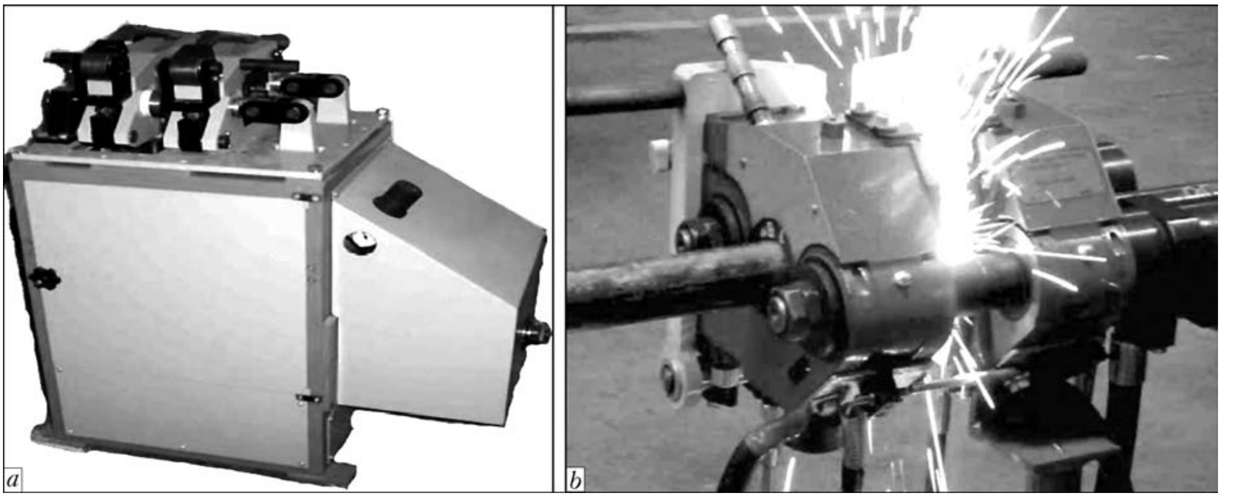

Figure 2. Machine MD101 (*a*) and machine MD1 in operation (*b*)

Table 2. Chemical composition of automobile parts, wt.%

Part	C	Si	Mn	S	P	Cr	Ni	Cu
Steering rod of ∅22 × 2.2 mm:								
pipe	0.194	0.174	1.01	0.004	0.015	0.05	0.04	≤0.02
part of left rod	0.175	0.107	0.91	0.004	0.012	0.17	0.07	0.12
part of right rod	0.170	0.080	0.90	0.004	0.011	0.17	0.07	0.22
Shock-absorber of ∅40 × 2.2 mm:								
pipe	0.146	0.152	1.23	0.004	0.012	0.05	0.04	≤0.02
bushing	0.136	0.162	0.56	0.018	0.011	0.07	0.08	0.08
Torque rod of ∅34 × 6.2 mm:								
pipe	0.18	0.22	0.55	0.010	0.015	0.02	0.01	–
head	0.32	0.20	0.55	0.008	0.006	0.05	0.05	0.1 W

Table 3. Main technological parameters of welding of parts

Part	Diameter, mm	Wall thickness, mm	Time of welding, s	Upsetting force, kN	Part shortening, mm	Consumed power, kW
Steering rod	22	2.2	3.7	21	2.1–2.3	6.1
Shock-absorber	4	2.2	4.8	31	3.7–3.9	6.7
Torque rod	34	6.2	13.2	40	7.0–7.5	7.2

the chemical etching by 4 % alcoholic solution of nitric acid was used.

Steering rods. The part of a steering rod represents a pipe of 300 mm length, to which rod hollow parts with 60 mm long thread are welded-on on both sides. Pilot technology of MIAB welding of pipe with hollow rods has been developed as a result of carried out investigations. Figure 3 shows the MIAB-welded joint.

Welded joints were subjected to rupture and bend tests. The rupture force was 12,900 kg, the fracture occurred on the pipe parent metal at 140 mm distance from the butt that proves the high mechanical strength of the joint. Bend tests showed high ductile properties of the joint.

Macrosections were manufactured from welded joints of the steering rod part (Figure 4). Width of HAZ was 2.2–2.4 mm. Welded joint does not require auxiliary operations after completion of the welding process and flash removal. Method of MIAB welding allows, when necessary, producing the height of weld reinforcement up to 0.5 mm.

The measurement of distribution of metal hardness in the zone of welded joint of the steering rod was

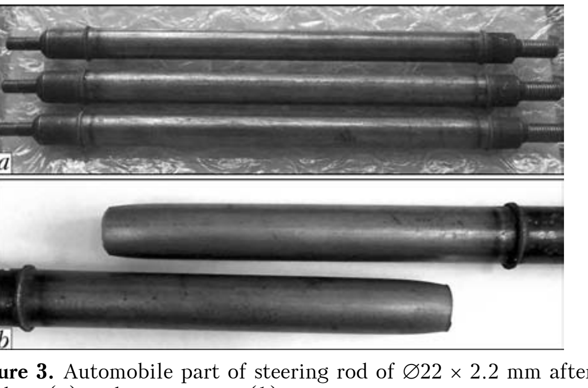

Figure 3. Automobile part of steering rod of ∅22 × 2.2 mm after welding (*a*) and rupture test (*b*)

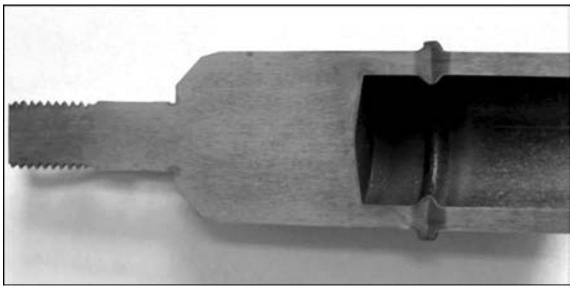

Figure 4. Macrosection (×1) of welded joint of left steering rod

performed in the direction from the pipe to the rod part (Figure 5). The carried out metallographic examinations of welded joint of the steering rod part showed the following results.

The ferrite decarbonized band on the welded joint line is absent (Figure 6). Metal hardness on the joint line is HV 2640–2970 MPa. Defects were not revealed in the joint zone.

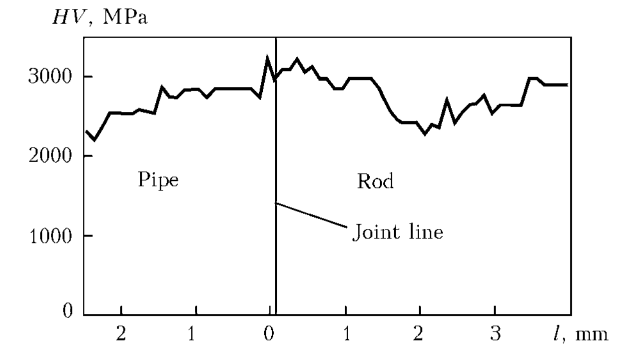

Figure 5. Distribution of metal hardness in the zone of welded joint of steering rod

The structure of HAZ overheating zone represents a mixture of pearlite, bainite (HV 3060–3110 MPa) and a small amount of ferrite (HV 2540–2610 MPa) (Figure 6). The width of overheating zone is 550–600 μm. Then the structure is refined, the amount of bainite is decreased, the amount of a pearlite component is increased.

The structure of parent metal of pipe is fine-grained (number 9–10 by GOST 5639–82), ferrite and pearlite (HV 2020 and 2120–2370 MPa, respectively) with a clearly expressed texture of rolled metal.

The structure of HAZ overheating area of rod part is bainite-ferrite (HV 2710–3210 MPa), width of overheating area is 700 μm. The structure of rod part parent metal is bainite-ferrite with hardness HV 2790–3090 MPa.

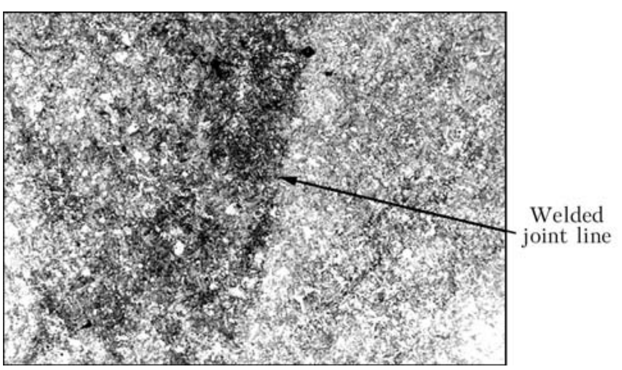

Figure 6. Microstructure (×250) of part–pipe welded joint (steering rod)

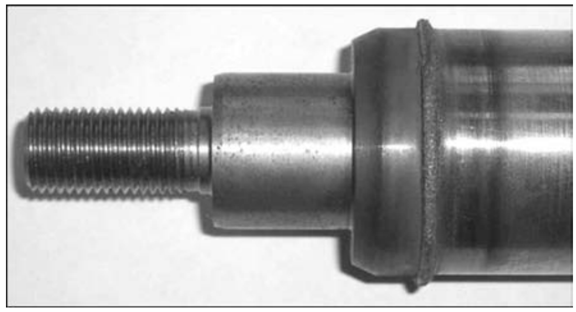

Figure 7. Welded joint of automobile part of shock-absorber

Shock-absorbers. The part represents a pipe of 300 mm length, the inner part of which is coated by chromium of 0.02 mm thickness, a hollow tail piece with 60 mm long thread is welded-on on one side. Figure 7 shows a welded joint made by MIAB method.

Mechanical tensile and bend tests showed that the joint strength is at the level of characteristics of the parent metal of the tail piece part. The tensile force up to fracture was 122 kN. Bend tests showed the high ductile properties of the welded joint.

Mechanical tensile and bend tests of welded joints of a torque rod and shock-absorber prove strength and high ductility of the joints, equal to those of the parent metal of parts. Bend tests are severe for this type of joints. The performed full-scale mechanical bend and rupture tests of parts of steering rod and shock-absorber showed that ductile properties of the welded joint are at the level of properties of the parent metal.

As a result of carried out investigations the pilot MIAB technology for the shock-absorber part has been developed.

Macrosection (Figure 8) was manufactured of the shock-absorber welded joint. Width of HAZ was 2.2–2.4 mm. Welded joint does not require auxiliary mechanical operations after completion of the welding process.

Metallographic examinations of welded joint of parts of shock-absorber of ∅40 × 2.2 mm showed the following results. Measurement of metal hardness distribution in welded joint zone was made in the direction from pipe into part (Figure 9). The ferrite decarbonized band on the line of joint of pipe and tail piece is absent (Figure 10). Metal hardness on the joint

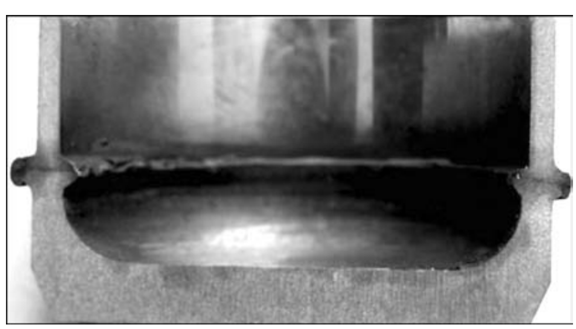

Figure 8. Macrosection (×1.5) of welded joint of shock-absorber

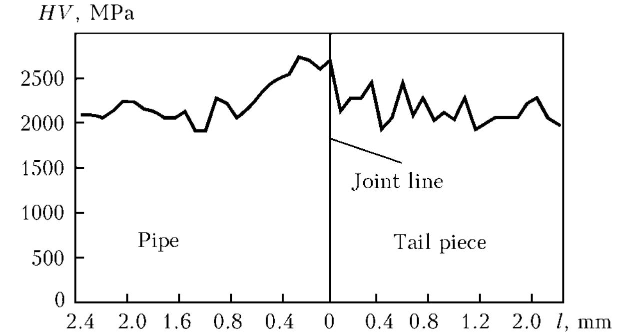

Figure 9. Distribution of metal hardness in the zone of welded joint of shock-absorber part

line is HV 2700–2850 MPa. Defects in the joint zone were not revealed.

The structure of HAZ overheating area of pipe metal consists of pearlite (HV 2570–2650 MPa), bainite (HV 3030–3210 MPa) and a small amount of ferrite. Width of overheating area is 500 μm.

The pipe parent metal has a ferrite-pearlite structure with a clearly expressed texture of rolled metal and HV 2210–2320 MPa.

The structure of HAZ overheating area of metal of tail piece part represents a mixture of ferrite with HV 2190–2210 MPa and pearlite with HV 2340–2390 MPa. Ferrite of different morphological forms is observed in the structure. Width of overheating area is 500 μm, HAZ length is 1200 μm.

The structure of parent metal of tail piece part is ferrite-pearlite (HV 1990–2210 MPa) with a great domination of a ferrite component.

It was found as a result of investigations that the welded joints of parts of steering rod and shock-absorber have no structures, changing significantly the properties of metal as regards to the parent metal. The bainite-ferrite structure is dominated in the structure of welded joints. The peculiar feature of structure of welded joints is the absence of a coarse-grain area.

Torque rod. The torque rod consists of a pipe and two heads. Pipe material is steel 20, heads are of steel 30. As-welded parts of the torque rod were subjected to fatigue tests in a special stand at tension–compression symmetric cycle. Results of tests are given in Table 4.

Table 4. Results of testing four torque rod parts at tension–compression symmetric cycle

Load, kN	Specific load, MPa	Number of cycles before fracture	Place of fracture
±70	133.0	914,000	In head body
±60	114.0	2,480,100	Same
±50	95.0	3,027,500	»
±45	85.5	10^7	Without fracture

The fracture of the torque rod part after tension-compression tests was in parent metal of a tip (Figure 11). The tests of welded joints at symmetric cycle

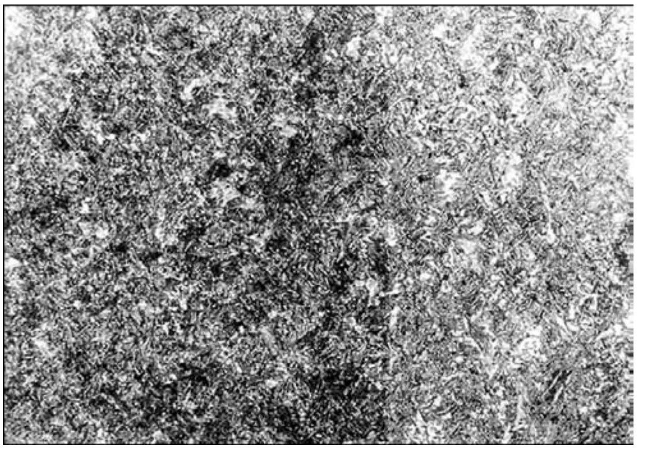

Figure 10. Microstructure (×320) of pipe–part welded joint (shock-absorber)

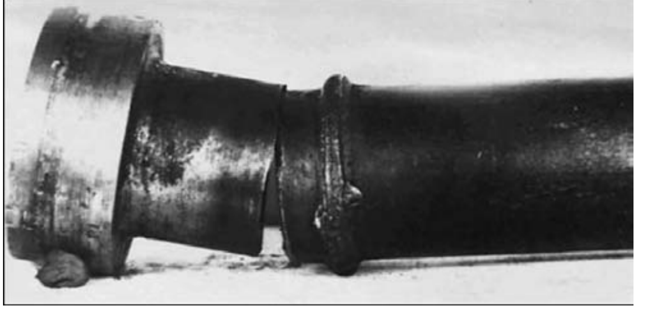

Figure 11. Part of torque rod after cyclic tests

of tension–compression were performed using joints with a flash. The presence of flash, causing the concentration of stresses, did not decrease the values of cyclic tests. This is stipulated by the fact that the fine-grain structure with high tough properties is observed in the place of an increased concentration of stresses at the boundary of weld reinforcement.

As a result of carried out investigations the pilot technology of MIAB welding of part of the ∅34 × × 6.2 mm torque rod of trucks has been developed.

Thus, the carried out full-scale mechanical rupture tests of parts of steering rod and shock-absorber, welded by MIAB method, prove the high mechanical strength, ductility and resistance to fatigue fractures of welded joint at the level of main characteristics of the parent metal.

The pilot technology of MIAB welding the automobile parts of ∅22 × 2.2 mm steering rod, ∅34 × × 6 mm torque rod and ∅40 × 2.2 mm shock-absorber has been developed. The developed technology can be used in mass production where the high labour productivity is required.

1. Kuchuk-Yatsenko, S.I., Krivenko, V.G., Kachinsky, V.S. et al. *Machine for magnetically-impelled arc butt welding.* Pat. 94128094 (3/4663) Ukraine. Publ. 20.12.94.
2. Kachinsky, V.S., Ignatenko, V.Yu., Golovchenko, S.I. (1997) Magnetically-impelled arc butt welding of tubular parts (equipment and technology). *Avtomatich. Svarka*, **7**, 39–41.
3. Kachinskiy, V., Ignatenko, V., Koval, M. (1999) Magnetically-impelled arc butt welding of hollow and solid parts. In: *Proc. of Int. Conf. on Exploiting Solid State Joining* (Cambridge, 13–14 Sept. 1999), 30–46.

LASER-ARC HYBRID WELDING PROCESSES (Review)

P. KAH[1], **A. SALMINEN**[1, 2] and **J. MARTIKAINEN**[1]
[1]Laboratory of Welding Technology and Laser Processing, Lappeenranta University of Technology, Lappeenranta, Finland
[2]Machine Technology Centre Turku Ltd, Turku, Finland

This study deals with the different types of hybrid welding processes in addition to describing the means and situation today regarding the principles and applications of various combinations of laser with welding arc. The processes are analyzed regarding their parameters involved and the type and thickness of the base material. This study looks into the productivity, economy and quality of laser hybrid welding and provides some fundamentals of the set-up of its parameters. The effects of parameters and set-up can be seen in the analysis, thus, the economic feasibility and quality management factors as the basis of analysis can be assessed.

Keywords: *laser-MIG/MAG welding, laser-TIG welding, laser-plasma arc welding, laser-tandem welding, laser-submerged arc welding, hybrid welding process*

The laser-arc hybrid welding process has been investigated since 1978, when Steen and co-workers in the UK published their first paper about TIG augmented laser welding [1]. Nowadays, the lasers used in hybrid welding include the older generation lasers like the CO_2, Nd:YAG and diode laser, and the new disc and fiber laser. The CO_2 laser was the firstly and normally used laser in hybrid welding [2–6]. The Nd:YAG laser was also used in hybrid process for welding of aluminum or materials of high reflectance and steel because of its short wavelength, which guarantees much higher absorption [7]. One reason to use Nd:YAG laser has been the possibility to use optical fiber for beam transportation.

Hybrid welding combines the energy of two different energy sources in a common process zone. Typically the focused laser beam is aimed to a joint perpendicular to the plate surface, whereas the arc torch is tilted to a suitable angle and aimed close to the interaction point of the laser beam and material. Typically this means that the laser beam with its high energy density and the electric arc with high energy efficiency interact at the same time in the same process area (plasma and weld pool) and mutually influence and assist each other. In the hybrid welding process, the number of variables grows through coupling the processes. The resultant mutual influence of the processes can have different intensities and characteristics depending on the arc and laser process used and on the process parameters applied [5–9]. A wide variety of hybrid processes exist, depending on the laser source (CO_2, Nd:YAG, diode, fiber or disc laser) and the arc welding process (MIG/MAG, TIG, plasma arc welding (PAW), tandem, submerged arc welding (SAW) with which it is combined. It is also possible to use special heads, in which the laser beam is surrounded by electric or plasma arc [9, 10].

With hybrid welding processes the potentials are fundamentally resolved by the appropriate selection of the method set-up and the basic parameter configurations adapted to the demand of material, structure and manufacturing conditions. If the boundary conditions are well chosen, hybrid welding proves to be a really stable, efficient, profitable and flexible technology.

Various studies have revealed that through coupling the processes synergistic effects are achieved and the disadvantages of the individual process can be compensated for, e.g. the typical narrow weld of laser welding leads in some cases to metallurgical and fit-up problems, and the higher heat input of arc welding increases distortion and subsequent rework cost. The advantages mainly come from:

- the gap bridgeability of the process to control the air gap caused by inaccurate groove manufacture and fixturing tolerances;
- the increase penetration and the welding speed above the sum of the single speed, thus, keeping the heat input and thermal distortions to the minimum;
- the increased regularity of the weld bead;
- a significantly wider range of applications adapted to the demands of material, structure and manufacturing conditions;
- the lower investment costs by saving laser power.

Metallurgical property improvements using filler material and diminished porosity due to the promoted escaping of gas out of the enlarged molten pool are also noted especially in the case of partial penetration welds [2, 3, 10–12]. However, in hybrid welding, the arc is stable because the arc cathode spot is located in the thermal action area by the laser radiation, which occurred in the keyhole. Therefore, the results observed with high speed camera show that the plasma generated by the laser was observed to play a vital role in arc stability [13, 14].

Hybrid welding has mainly been introduced in applications, in which plate thicknesses allow single pass welding, and thus also experimental work has been focused on single pass welding. A limiting factor with regard to plate thickness in single pass welding is the power of the laser. Naturally, with high power lasers, it is possible to weld thicknesses of up to 30 mm with

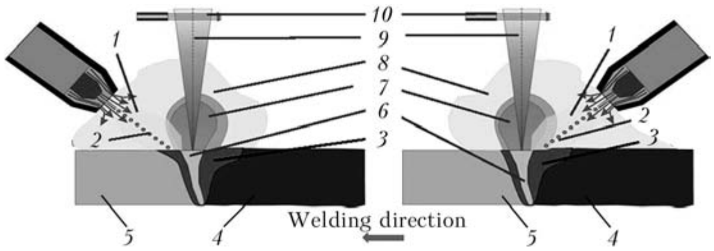

Figure 1. Schematic representation of laser hybrid welding with leading laser and leading arc arrangements: *1* — arc; *2* — filler material; *3* — melt pool; *4* — weld metal; *5* — workpiece; *6* — keyhole; *7* — metal vapour; *8* — shielding gas; *9* — laser; *10* — cross jet

a single pass. But also with medium power lasers, the welding of very thick steel plates is possible by using a gap between the plates to be welded and the multi-pass welding technique. Hybrid welding gives excellent opportunity to use medium power lasers for thicker sections, like in laser welding with a filler wire. In this case laser does not have to be very powerful, and this means a reduction in the investment cost and still more effective welding can be done. Apart from the square butt preparation, also V- and Y-groove can be used which are partially a result of blanking without any further edge preparation.

Application fields in laser-arc hybrid welding have been expanding in a variety of workshops and industries (for example, shipbuilding, automotive industry, vessel manufacturing) [9–11, 15, 16], as well as being an extensively studied method for a variety of materials. It is owing to a number of advantages of hybrid welding compared with individual processes.

The distance between the laser beam position and the arc (process distance) is an important parameter of hybrid welding as has been shown in [17]. If the distance is too long, the laser and arc plasmas will be apart from each other resulting in an unstable arc, since the laser plasma and heated material are no longer supporting the generation and maintenance of the arc [18]. According to some researchers, when the separation of the processes is 5 mm or more, the processes are acting independently [18, 19]. Of course this value depends, for example, on the welding speed, laser and arc powers and the material used.

Laser-MIG/MAG welding process. The fundamentals of the coupled process (Figure 1) are nearly the same for both the CO_2- and the solid-state lasers. The laser and arc processes have a common process zone and weld pool. The process can be controlled in such a way that the MIG/MAG welding part provides the appropriate amount of molten filler material to bridge the gap or fill the groove, while the laser is generating a keyhole within the molten pool to ensure the desired penetration depth. This can be reached at high speed. By combining the laser beam and the MIG/MAG arc, a larger molten pool is formed compared to the laser beam welding process [10].

The microstructure and mechanical properties of the weld metal can be improved by controlling its chemical composition by using proper filler material. In this case, the wire feeding elements should distribute homogeneously all over the weld metal to attain a homogeneous microstructure. It is not easy, however, to attain homogeneous distribution in narrow and deep penetration hybrid welds. The hot crack affinity of extrusion compound alloys is another reason to use filler material. With regard to those applications, the largest potential of the laser-arc hybrid welding technique is expected to be in the area of using additional filler material and thus the combination of laser-MIG/MAG hybrid welding process which is currently the most preferred laser-arc hybrid welding process [3–10]. This process has been reported to close gaps between 0.6 mm (with 2.7 kW [20]) and 1 mm (with 2.0 [18] and 5.7 kW [15]).

As with any other welding process, also the capabilities of laser-MIG/MAG hybrid welding are essentially determined by the appropriate selection of the system set-up and the basic parameter configuration. In that case, the parameters of laser and MIG/MAG welding can be varied freely in a rather wide range in order to adjust the welding process to the required performance regarding depth, gap bridging, weld shape and metallurgical properties [5].

If we compare the penetration characteristics of laser, MIG/MAG and hybrid welding, it shows that the laser weld has bead concavity, whereas the MIG/MAG-welded seam has extreme weld support and hybrid welding has extreme reinforcement and high weld width with the same penetration depth and the same welding speed as in laser welding. A typical example of such welds can be seen in Figure 2, which somewhat exaggerates the difference, since the welding is performed in bead-on-plate configuration, but still represents the situation.

The penetration depth is mainly determined by the laser beam power and shaping, whereas the weld width is mainly determined by the arc, in particular, by the

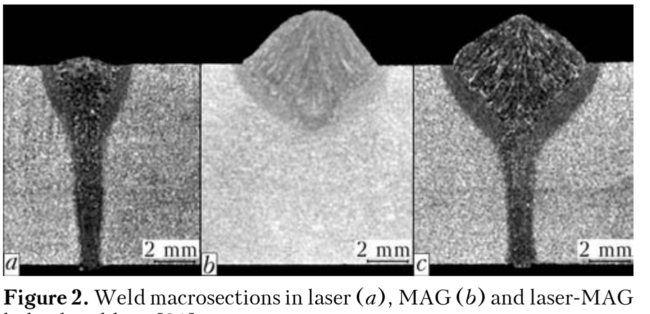

Figure 2. Weld macrosections in laser (*a*), MAG (*b*) and laser-MAG hybrid welding [21]

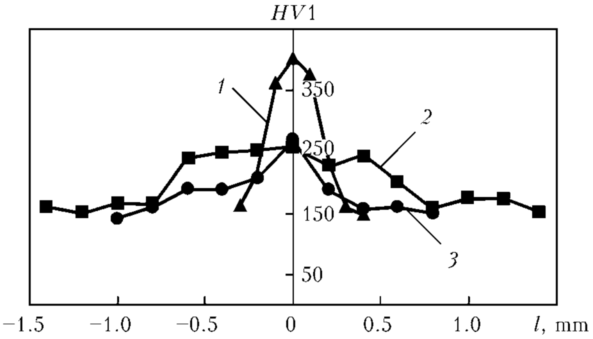

Figure 3. Hardness $HV1$ of weld metals at MIG-laser hybrid welding without gap of 2.13 mm CMn alloy 250 using 2250 W CO_2 laser and 9 kW MIG arc at maximum speed of laser (*1* — 4.4), MIG (*2* — 2.2) and hybrid (*3* — 4.5 m/min) welding [25]: l — distance from weld center, mm

voltage. If there is no air gap, the maximum welding speed achieving full penetration for CO_2 laser-MIG/MAG hybrid welding is lower than for CO_2 laser welding. This is caused by the extra material on top of the workpiece that requires to be penetrated and the fact that the focal point position is diverted from the set-up value. The welding speed can, however, be increased with an increase in the air gap width. Air gaps of up to 1.5 mm in width can be bridged, but at this maximum width the process is quite unstable and produces spatters. The welds produced by hybrid welding have also typically lower hardness in comparison to that in arc welding [22].

According to an experiment carried out to investigate the stability of the condition of a hybrid CO_2 laser-MIG/MAG process by analyzing the influence of several process parameters, it was shown that the optimum process distance depends on the metal transfer mode in shielded-gas metal arc welding. The base metal transfer mode is important in order to achieve a stable and repeatable process. It has been reported in many papers that arc parameters giving the pulsed/spray arc should be preferred to the short/globular arc [10, 23]. Nd:YAG laser radiation, due to a lower interaction with the arc plasma, allows a closer approach to the arc than CO_2 laser radiation. The focal point should, in most cases, be set below the workpiece surface to maximize penetration [9]. Normally, the smallest possible arc inclination is desired. Angles in the range of 15 to 30° relative to the laser axis work with technically acceptable effort.

Lui et al. [24] studied the process parameters of laser-MAG hybrid welding of HSLA-590 steel using a 2.4 kW CO_2 laser with MAG welding. They found that the arc-leading hybrid bead was not as smooth as the laser-leading bead. Considering the bead appearance, the laser-leading process is better than the arc-leading hybrid process. It was also examined that the hybrid weld metal had a higher toughness than the laser weld metal even at higher welding speed.

Hardness measurements in MIG-laser hybrid welding were made on butt welds with a zero gap and the maximum possible welding speeds resulting in sound welds. Figure 3 shows that the maximum values are HV1 400, 258 and 268 for the laser, MIG and hybrid processes, respectively. This corresponds to 2.5, 1.7 and 1.75 times the base material values, respectively. Despite the higher value in the center of the hybrid weld as compared to the MIG weld, the hardness values of the hybrid weld are generally $HV1$ 20–50 lower than those of the MIG weld. This also results in a 40 % reduction of the size of the HAZ, from 8.6 to 5.2 mm^2, measured with the aid of digital image processing. The bainite is completely avoided in MIG-laser hybrid welding where acicular ferrite is formed in the HAZ. This also explains the considerable reduction in the hardness of the weld metal [25].

The effect of the gap distance in butt welding can be visualized by plotting the maximum welding speed to the ability to bridge gaps (Figure 4). The laser welding process displays a clear drop in the welding speed at a gap wider than 0.1 mm. For the MIG welding, no change is evident at variable gap distances. For the hybrid welding, only a small decrease in the maximum welding speed is observed at increasing gaps. With a gap size of 0.6 mm, a reduction in speed of only 22 % (from 4.5 to 3.5 m/min) is seen [25].

Different joint configurations, materials and material thickness have been investigated in hybrid welding by different research groups. Figure 5 shows excellent misalignment tolerances reported in [15] on

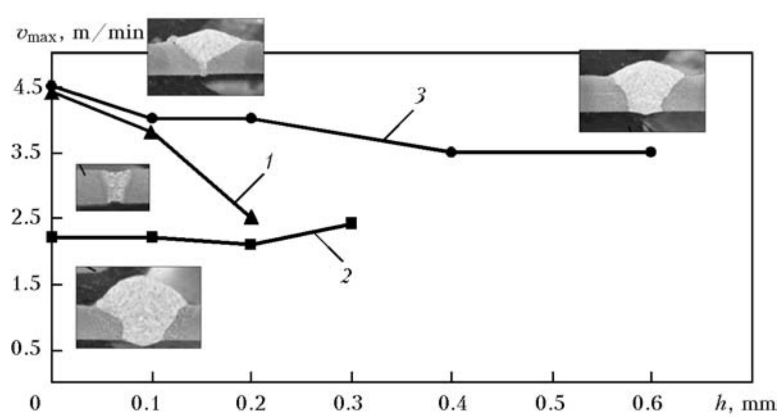

Figure 4. Effect of gap width h on maximum speed v_{max} of laser (*1*), MIG (*2*) and hybrid (*3*) welding of 2.13 mm CMn alloy 250 using 2250 W CO_2 laser and 9 kW MIG arc [25]

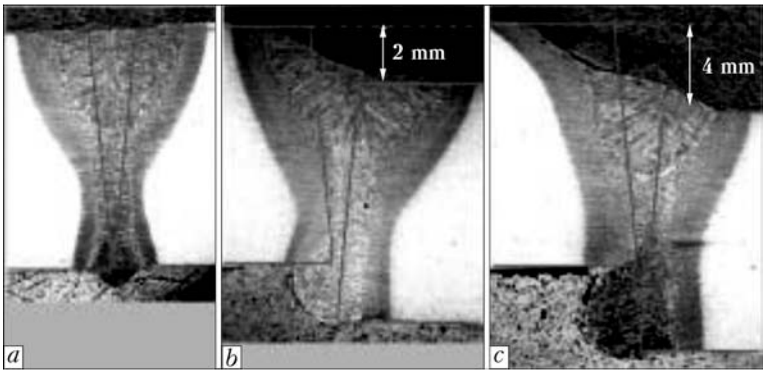

Figure 5. Macrosections of the pipeline steel X52 welded joints 10 mm thick at speed of hybrid welding of 1.0 (*a*) and 0.8 (*b, c*) m/min [15]

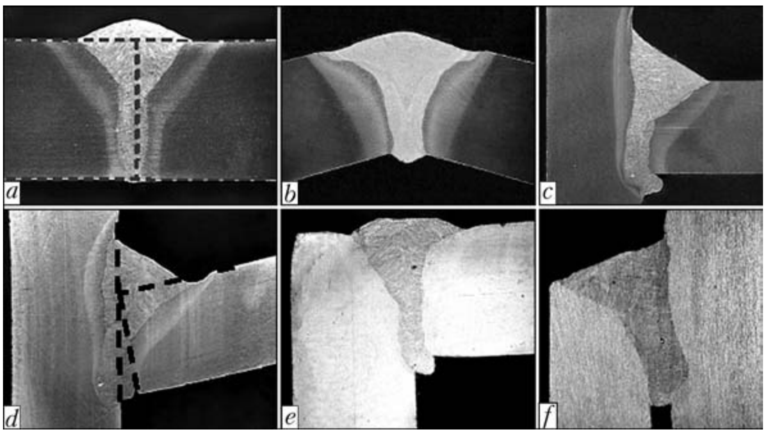

Figure 6. Macrosections of the different configuration hybrid-welded joints for 6–8 mm heavy section steel (*a–e*) and 2 mm thin sheet steel (*f*) [26]

hybrid welding of 10 mm pipeline steel X52 with 10° single V-groove and 1 mm root face, using CO_2 laser of 10.5 kW, MIG pulse arc, filler wire G3Si1 of diameter 1.2 mm and assist gas argon–helium mixture at wire feed rate of 5.2 m/min. Hybrid welding is superior to the laser welding in respect of this joint preparation fault.

Hybrid welding has also shown a very good weld bead reinforcement junction to the base material of different joint configurations (Figure 6) [26]. According to the description, a 3 kW Nd:YAG laser using a 0.6 mm fiber or a 6 kW CO_2 laser were used. The welds were crack- and pore-free welds of sufficient strength, and produced at very high speeds.

A study was recently conducted in Fraunhofer-Institut fuer Lasertechnik (ILT) [3] to expand the previous state of the art of laser-MAG hybrid welding of high strength structural steels. The majority of the welds were carried out with an incorporated nozzle for hybrid welding fabricated by ILT. The results shown that the laser beam power and the welding speed have to be regulated to the plate thickness and the gap width for butt joints in the downhand and side position. It was noticed in the same experiment that thicknesses ranging up to 25 mm can be welded (Figure 7) without any hot cracks, and if they exist, with only few small pores. V- or Y-groove preparation in the range of 4–8° full angle and suitable welding speed mutually with the right energy input per unit length are the vital points to be considered.

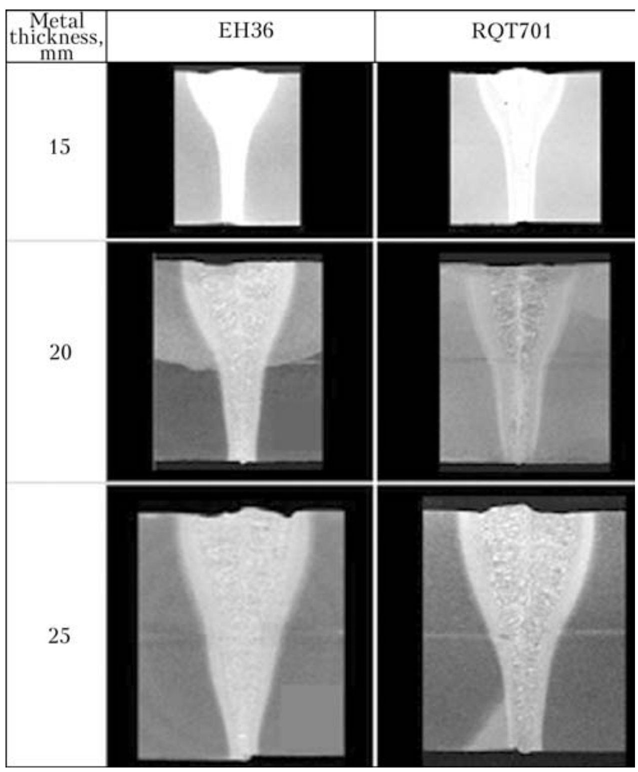

Figure 7. Cross-sections of optimized hybrid welds used for mechanical and technological tests [3]

The differences between the CO_2 and the Nd:YAG laser in hybrid welding come as a result of their wavelengths. The CO_2 laser is more economical and offers a higher speed than the Nd:YAG laser if the available higher power is utilized. But the laser beam delivering system is more complex for the CO_2 laser than for the Nd:YAG laser with a shorter wavelength that can be delivered through an optic fiber. This offers higher absorption especially in the case of welding aluminum. However, both the CO_2 and lamp-pumped Nd:YAG laser have significant drawbacks. The first one is the relatively low wall plug efficiency at much less than 10 %. This means that the systems not only require large amounts of energy to operate but that they also require chiller equipment to extract waste heat [13, 16, 17, 27].

The choice of process gas (shielding gas) parameters is an important factor in hybrid welding. With Nd:YAG lasers the selection of process gas can be determined according to the arc stability demands and bead shielding properties; for MIG/MAG welding also droplet detachment and spatter-free metal transfer have to be considered. In this case argon will constitute the dominant portion of the gas used. Small additions of oxygen promote droplet detachment and reduce spatter. Mixtures of helium lead to higher arc voltage and the corresponding power increase results in wider welds, but also destabilize the arc. Nevertheless, using CO_2 lasers, a helium mixture is often used to avoid plasma shielding. Fortunately, the presence of the laser beam enables acceptable arc stability even with a significant helium portion [27].

Within the automotive industry, Volkswagen and Audi are two particularly well-known examples of companies convinced by the benefits of hybrid laser-MIG welding. In the shipbuilding industries the technique is slowly gaining a firmly established acceptance for a wall thickness of 15 mm [6, 9, 15, 28].

Laser-TIG welding process. When a TIG arc is operated simultaneously with a laser beam, a heat condition is established in which it is theorized that laser absorption is improved. The absorption of the laser energy into the base material is enhanced in this heated region [5]. This combination creates a moving common melt pool along the weld pass. A typical schematic diagram of laser-TIG welding is presented in Figure 8.

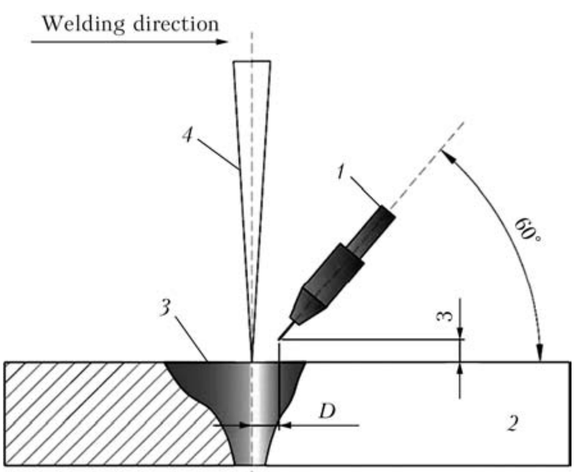

Figure 8. Schematic set-up of hybrid CO_2 laser-TIG welding [29]: *1* — TIG welding torch; *2* — workpiece; *3* — weld pool; *4* — laser beam; *D* — laser–arc distance

Steen and Eboo [1] conducted their experiments with CO_2 laser and TIG arc. It was found that combining a TIG arc with the laser meant serious advantages to the process: firstly, the arc root remained stable in the hot spot generated by the laser so that the arc, even of low current, can be performed with high welding speed without instability, and, secondly, the arc root is narrowed in the combined process which appears to avoid some of the undercutting normally associated with high speed arc welding especially of aluminum alloys. The absorptivity of the weld metal increases with an increase in temperature in the case of a 10,600 nm wavelength [1, 15, 30]. It is also reported that both the CO_2 laser and the TIG welding processes greatly depend on the shielding gas and its protecting method used [6].

Lui and Zhao [31] have studied the welded joint of magnesium alloy and steel by using different joining techniques. They found that due to the high energy intensity and the fast stir action in the molten pool, it is possible to weld magnesium alloy and steel by laser-TIG hybrid welding, which is almost impossible with conventional fusion welding processes, with the following parameters: laser power of 400 W, welding speed v = 15 mm/s), TIG welding current I = 80 A, process distance of 1 mm, laser focus position of 1 mm, diameter of the tungsten electrode of 3.2 mm, angle between the electrode from the workpiece and welding direction of 50°, and the argon flow rate of 0.5 l/s. Moreover, the laser pulse frequency was 39 Hz.

One of the defects of laser welding is porosity due to the high power density and deep penetration especially in the case of partial penetration. A great challenge is to avoid or decrease the number of weld pores when welding aluminum. The set-backs are porosity due to the evaporation of alloying elements such as magnesium. Cracks can also appear if the welding parameters are not suitable [6, 14]. However, porosity formation in weld metal depends on the TIG welding current and the composition of the shielding gas in laser-TIG hybrid welding.

Laser-TIG hybrid welding has proven to be a promising technique to weld very thin austenitic stainless steel sheets (0.4–0.8 mm) in a butt joint configuration. The molten pool generated by laser stabilizes the TIG arc allowing welding speeds as high as 15 m/min with the laser trailing. The combination of both the laser and TIG arc is able to produce full-penetrated welds with enough width to absorb small cut edge defects or misalignments between the two sheets. In order to avoid thermal distortions and excess fusion,

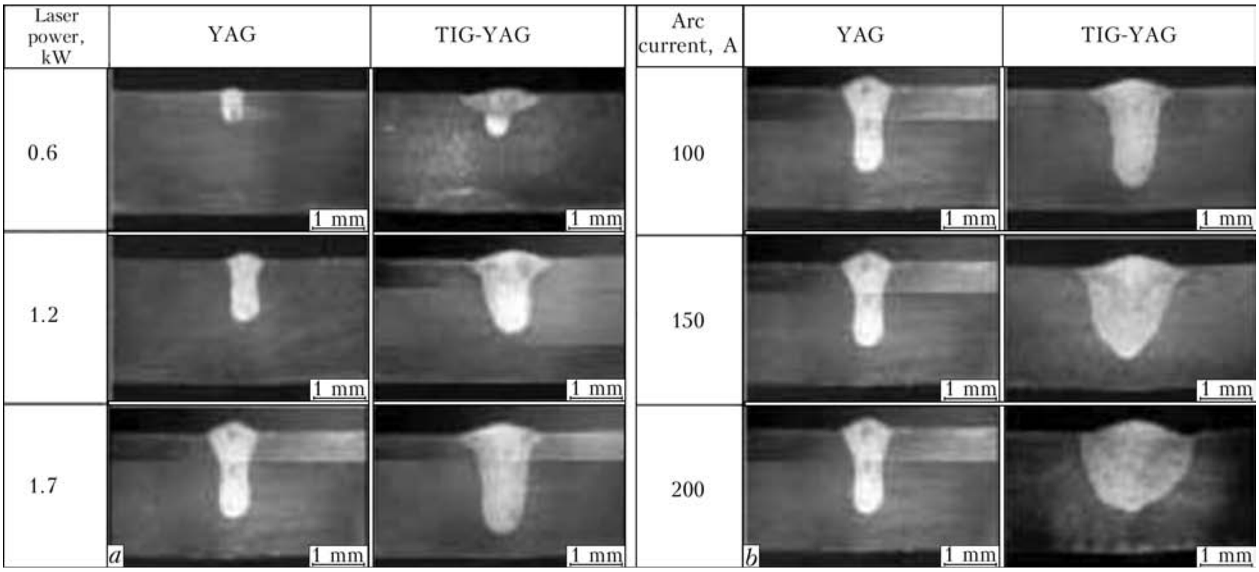

Figure 9. Cross-sections of 304 type stainless steel 5 mm thick in YAG laser and hybrid laser-TIG welding at various laser power (*a*) and arc current (*b*) [12]: *a*, *b* — v = 10 mm/s, α = 55°, h = 2 mm, d = 2 mm, I_a = 100 A, Ar as shielding gas ($5\cdot10^{-4}$ m^3/s); *b* — P = 1.7 kW

the TIG welding current has to be minimized and the use of additional shielding gas is necessary [32].

It is also noted by other researchers that the penetration in the hybrid welding process does not depend on the arc current but on the laser power in CO_2 laser-MAG hybrid welding and Nd:YAG laser-TIG hybrid welding [26, 33]. Figure 9, *a* shows the cross-section of the 304 type stainless steel welds subjected to YAG laser and YAG laser-TIG hybrid welding at various laser powers. In all of the welds, the penetration of hybrid welds was deeper than that of YAG laser welds when the TIG welding current was kept at a constant value. However, in the cases of different TIG welding currents and constant laser power, the penetration remained the same, but the weld width grew with the increase of TIG welding power as shown in Figure 9, *b* [12].

Laser-PAW process. In a process for laser-plasma hybrid welding to weld workpieces, the laser beam and the plasma jet are brought together in the process region close to the workpiece (Figure 10) [34]. In operation, the plasma torch is positioned at an angle of approximately 45° to the laser beam. A free microwave-induced plasma jet is generated in a high-frequency microwave source and guided in a hollow waveguide. The process gas is introduced into the microwave-transparent tube through the gas inlet opening and plasma is generated by an electrode-free ignition of the process gas [34–36]. The main arc initiation is via a low amperage pilot arc formed between the tip of the electrode and the nozzle. When the pilot arc is switched on, it produces sufficient heat to ionize the air gap between the nozzle and the workpiece. An additional advantage from the tungsten electrode is that the electrode is placed behind the nozzle that provides the characteristic jetting effect of the plasma gas. Stable arc operations are maintained without deteriorating the electrode for relatively long periods since the tip of the electrode is not exposed to impurities [35].

By using a hybrid laser-plasma welding process, the arc heat source is introduced which can be used as a heat treatment tool to increase cooling rates after welding. In this way the presence of a brittle microstructure, which is susceptible to failure during service, can be reduced. In addition, by using hybrid laser-plasma welding as an integrated welding and heat treatment system, the production time can be significantly reduced [35].

The process offers significant advantages when used for laser-plasma welding including a stiff, high-temperature, columnar arc with good directional properties which permit greater tolerance compared with laser welding to disparity and comparable poor fit-up conditions. Furthermore, for a relatively small capital increase this process offers commercial advantages and potential for multiple applications of lasers in the manufacturing industry. At present, there are only a

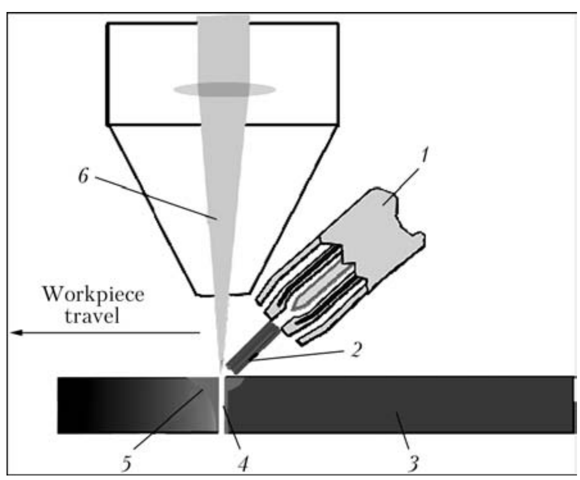

Figure 10. Experimental arrangement of plasma arc augmented laser welding system: *1* — plasma torch; *2* — plasma arc; *3* — workpiece; *4* — keyhole; *5* — weld pool; *6* — laser beam

few hybrid laser-plasma systems installed in industrial applications but this will most likely change in the future due to the great potential of the process. In order to stimulate the use of hybrid laser-plasma systems, a thorough scientific understanding of the process and investigation of its industrial feasibility are required [34].

Early tests on the laser-augmented PAW process [34] were carried out using a 400 W CO_2 laser and a 50 A arc current. In the experiment a wide variety of different materials were tested which included mild steel, stainless steel, titanium and aluminum in various thicknesses from 0.6 to 2.0 mm. It was noted that the combined process can suppress humping in high speed welding with thin sheets. In plasma arc-laser welding, a higher tolerance to beam–gap misalignment (0.15–0.5 mm at 2 m/min and 50 A) has been noted.

It was reported [37] that the laser-assisted PAW process eliminates hot cracking in the fusion zone for aluminum alloys 6061 and 6111 when using a continuous power arc instead of the pulsed arc. Fusion zone dimensions for both stainless steel and aluminum were found to be wider than laser welds. It was also noticed that the laser-plasma welds did not appear as shiny as with pulsed Nd:YAG laser welding. The laser-plasma hybrid welding process was also experienced to be a very stable process, a phenomenon that has earlier been described for laser-GMA welding.

Laser tandem-MIG welding process. The laser tandem-MIG process is combinations of laser welding and the arc processes with only one molten zone. The process principle of laser tandem-MIG hybrid welding is outlined in Figure 11 [9]. The laser beam is set at approximately 90° to the workpiece and is used for welding the root. Both of the other trailing arcs have a pushing tilt angle and are used for increasing the ability to bridge root openings and increase throat thickness. The process uses three different power outputs, thus the outputs can be set, depending on what welding result is desired. The welded joint geometry, the preferred joints overfill, and the welding speed can be selected by means of suitable power output for the tandem process. Also, by regulating the welding speed, focal point diameter and laser power, the depth of the root can be adjusted in the course of bevel preparation. Moreover, two different filler metals with various compositions can be used to attain the desired metallurgical properties [9].

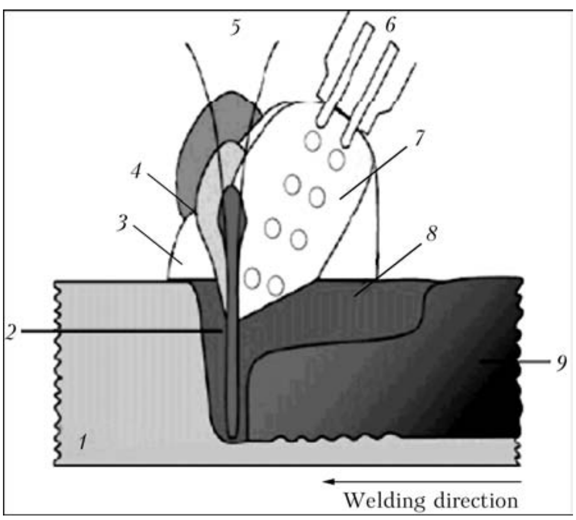

Figure 11. Schematic sketch of laser tandem-arc welding [9]: *1* — workpiece; *2* — keyhole; *3* — shielding gas cloud; *4* — laser-induced plasma; *5* — laser beam; *6* — electrode; *7* — arc; *8* — weld bead; *9* — molten pool

By selecting favorable process parameters the weld metal properties such as geometry and structural constitution can be purposefully influenced. The arc welding processes increase the gap bridging ability by the amount of the filler material added. It also determines the weld width and thus decreases the requirements of weld preparations. Process efficiency can be considerably increased by the interactions of the processes.

Reported mostly by Staufer [9, 38], the vital advantage of combining processes in this manner is the fact that as the filler metal melts off, it generates an arc pressure, which does not act on the workpiece but is distributed across separate arc roots. In the laser tandem-MIG hybrid process the control of the laser power, the power of the arc and the arc lengths is possible separately which is claimed to result in better drop detachment, more stable arcs and fewer spatters. Moreover, with this process it is also possible to use laser-MIG/MAG hybrid welding with a single arc. The laser tandem hybrid process has been investigated by Staufer [38] for a structural steel pipe, which complies with the standard EN 10149-2 for a pipe with a wall thickness of 8 mm and an inner diameter of 500 mm. It was reported that by using a Y-groove preparation, a full penetration weld can be achieved.

Laser-SAW process. The laser-MIG/MAG hybrid welding process met problems in some applications with regard to pores at the root of the sheet when more than 12 mm thick plate is welded with partial penetration. This was attributed to the insufficient degasification possibility of deep and narrow laser welds. To prevent this, the molten pool has to be maintained for a longer period [39]. This was the reason for experimenting with maintaining the molten pool for a longer time by using the laser-SAW hybrid process and thus creating more favorable degasification possibilities. Here both processes are moved as close as possible (13–15 mm) into one process zone [28].

The coupling of the processes, both the laser beam welding and the SAW process in one process zone proved to be a problem, since the flux had been falling into the keyhole of the laser beam and the laser radiation had been absorbed by the flux and not by the component. For that reason, a device which impeded this «falling forward» of the flux had been designed and built. One starting point is the separating plate (patented by RWTH, Aachen University), which is mounted between the laser beam and the flux feeder (Figure 12).

As far as previous investigations are concerned, the spatial distance of both processes and the separation of the weld into two regions, namely, the laser-welded and SA-welded region, has been noticeable. The distance must be chosen to be short enough to ensure that the smallest possible quantities of the flux are falling forward and large enough that the slag running ahead of the process does not jam to the sheet. The inclination angle of the separating plate is also most important. If the inclination angle is too large, the separating plate may be captured by the laser beam, and if it is too small, the arc might burn between the separating plate and the filler wire. Those areas have not shown any mixing of the weld material. It has just been the preheating, brought in the laser beam welding process which resulted in the synergy effect of increasing the welding speed of the SAW process [21, 40].

So, it is established that hybrid laser-SAW is the most attractive variation of laser-arc hybrid welding. The industry shows interest in hybrid laser-SAW and a possible practical application. This will be further increased through the use of less expensive, more robust and more flexible laser power sources. Further development of this process and a wider field of application are to be expected from the use of solid-state lasers. Particularly advantageous is the reduced risk of plasma shielding. It is easier to couple the shorter wavelength of the solid-state laser into the material to be processed. The flexibility of the equipment would also improve with a shorter wavelength, since the complicated beam guidance via mirror optics can be dispensed with and the laser beam can be guided via optical fiber into the processing optics [28].

For achieving better degasification and a weld, if it has a pore quantity which is as low as possible, or a pore-free weld, the solution may lie in the expansion or stabilization of the vapour capillary. One possibility for this would be welding and testing with adapted oscillating optics.

The addition of shielding gas/or process gas is another process parameter, which has to be tested for further work in this field. If efficient solid-state lasers, e.g. fiber lasers, can be used, the shielding gas could be dispensed with and a compressed air jet could be used, for cleaning of the weld surface would be reduced this way and the method would become even more economically viable [28].

Laser-SAW hybrid process improved degassing through the covering of the molten metal by the slag, good gap bridging ability, increased welding possibilities compared to laser welding thick plate by using different diameters of wire. Large potential expected through application of suitable wire/flux combinations, new fields of application of the laser technology [28].

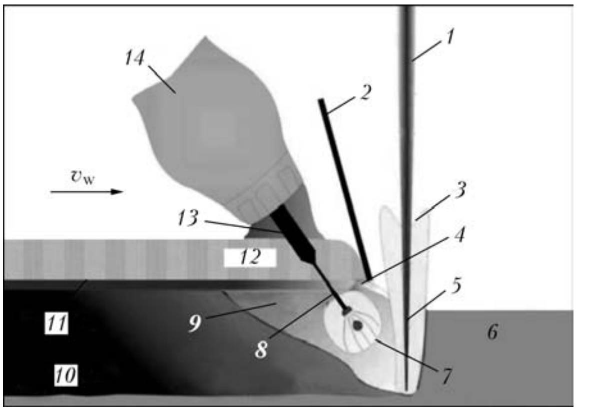

Figure 12. Schematic representation of laser-submerged arc hybrid welding [28]: *1* — laser beam; *2* — separation plate; *3* — metal vapour plasma; *4* — liquid slag; *5* — keyhole; *6* — base metal; *7* — weld cavity with arc; *8* — consumable electrode wire; *9* — molten pool; *10* — weld metal; *11* — solid slag; *12* — flux; *13* — contact tube; *14* — flux hopper

CONCLUSIONS

From the study to assess the different types of laser-arc hybrid welding, it came out that the process is involved in a growing number of industrial applications due to the economic and technical advantages of this technology. Some important superior features, compared to laser welding, are listed below:

- this disruptive technology has the potential to dramatically change construction methods, accepted production paradigms and business economics. Manufacturers who embrace this technology stand to make significant gains over their competitors;
- hybrid welding requires an appropriate selection of the system set-up and basic parameter configurations. If these boundary conditions are well chosen, hybrid process proves to be a really stable, efficient and flexible technology. Thus, if they are not properly set, there will be defects in the weld;
- productivity is improved through an increased welding speed. For sheet material it is possible to get a 40 % enhancement of the speed compared to conventional laser welding;
- when using hybrid welding, the investment cost for the laser power source is significantly less and the electrical efficiency is much higher;
- with 20 mm thick it is now considered as the state of the art to weld joints with gaps in the range of 0 to 1 mm in a flat position and using an I-, V- or Y-edge preparation with high strength structural steel. Thus, laser-MIG/MAG hybrid welding has the capability of single-pass full penetration and is confirmed for an increased thickness range;
- another practical consideration in introducing the hybrid process in industrial applications is the ability to produce quality welds in the face of a changing joint gap for welding thicker sections by allowing achievable edge preparation;
- in an industrial application, it is conceivable that the gap would vary throughout the weld, and it is desirable to develop a single set of processing condi-

tions to accommodate this condition, so that expensive sensor feedback and real-time parameter adjustment is not required;

• nevertheless, this technology is recognizing only a slow growth in today's industries. Some explanations for this slow acceptance are the high investment costs and the complexity of the process due to its large number of parameters. The set-up of the processing parameters requires a high degree of skill and accuracy, and these imperatives added to an incomplete knowledge of the process are the limiting factors for its wider industrial application.

1. Steen, W.M., Eboo, M. (1978) Arc augmented laser welding. *Metal Construction*, 21(**7**), 332–335.
2. Bagger, C., Olsen, F.O. (2005) Review of laser hybrid welding. *J. Laser Appl.*, 17(**1**), 2–14.
3. Petring, D., Fuhrmann, C., Wolf, N. et al. (2007) Progress in laser-MAG hybrid welding of high strength steels up to 30 mm thickness. In: *Proc. of ICALEO* (Orlando, Florida, USA), 300–307.
4. Fellman, A., Jernstrom, P., Kujanpaa, V. (2003) CO_2-GMA hybrid welding of carbon steel — the effect of shielding gas composition. In: *Proc. of ICALEO* (Jacksonville, Florida, USA, October 13–16), 56–65.
5. Dilthey, U., Wiesschemann, U. (2002) Prospectives offered by combining and coupling laser beam and arc welding. *Welding Int.*, 16(**9**), 711–719.
6. Graf, T., Staufer, H. (2003) Laser-hybrid welding drivers VW improvements. *Welding J.*, **17**, 42–48.
7. Shibata, K., Sakamoto, H., Iwasa, T. (2006) Laser-MIG hybrid welding of aluminium alloys. *Welding in the World*, 50(**1/2**), 27–34.
8. Jokinen, T., Karhu, M., Kujanpaa, V. (2003) Welding of thick austenitic stainless steel using Nd:YAG laser with filler wire and hybrid process. *J. Laser Appl.*, **15**, 220–224.
9. Staufer, H. (2007) Laser hybrid welding in the automotive Industry. *Welding J.*, October, 86(**10**), 36–40.
10. Kaierle, S., Bongard, K., Dahmen, M. et al. (2000) Innovative hybrid welding process in an industrial application. In: *Proc. of ICALEO* (Dearborn, USA), **89**, 91–98.
11. Defalco, J. (2007) Practical applications for hybrid laser welding. *Welding J.*, October, 86(**10**), 47–51.
12. Naito, Y., Mizutani, M., Katayama, S. (2003) Observation of keyhole behavior and melt flows during laser-arc hybrid welding. In: *Proc. of ICALEO* (Jacksonville, Florida, USA), Section A, 159–167.
13. Sugino, T., Tsukamoto, S., Arakane, G. et al. (2006) Effects of interaction between the arc and laser plume on metal transfer in pulsed GMA/CO_2 laser hybrid welding. *IIW Doc. IV-903–06*.
14. Hu, B., Den Ouden, G. (2005) Laser induced stabilisation of the welding arc. *Sci. and Techn. of Welding and Joining*, 10(**1**), 76–81.
15. Petring, D., Fuhrmann, C., Wolf, N. et al. (2003) Investigations and applications of laser-arc hybrid welding from thin sheets up to heavy section components. In: *Proc. of ICALEO* (Jacksonville, Florida, USA), Section A, 1–10.
16. Mahrle, A., Beyer, E. (2006) Hybrid laser beam welding — classification, characteristics and applications. *J. Laser Appl.*, **18**, 169–180.
17. Kah, P., Salminen, A., Martikainen, J. (2009) The effect of the relative location of laser beam and arc in different hybrid welding processes. In: *Proc. of ICALEO* (Orlando, Florida, USA).
18. Kutsuna, M., Chen, L. (2002) Interaction of both plasma in CO_2 laser-MAG hybrid welding of carbon steel. *IIW Doc. XII-1708–02*.
19. Abe, N., Hayashi, M. (2002) Trends in laser arc combination welding methods. *Welding Int.*, 16(**2**), 94–98.
20. Bagger, C., Wiwe, B.D., Paulin, N.A. et al. (2003) Closing the weld gap with laser/MIG hybrid welding process. In: *Proc. of 9th Conf. on Laser Materials Processing in the Nordic Countries* (Trondheim, Norway), 113–124.
21. Olschok, S., Reisgen, U., Dilthey, U. (2007) Robot application for laser-GMA hybrid welding in shipbuilding. In. *Proc. of ICALEO* (Orlando, Florida, USA), 308–315.
22. Shinn, B.W., Farson, D.F., Denney, P.E. (2005) Laser stabilization of arc cathode spots in titanium welding. *Sci. and Techn. of Welding and Joining*, **10**, 475–481.
23. Schubert, E., Wedel, B., Kohler, G. (2002) Influence of the parameters on the welding results of laser-GMA welding. In: *Proc. of ICALEO* (Phoenix, USA), Section A.
24. Lui, Z., Kutsuna, M., Xu, G. (2006) Properties of CO_2 laser-GMA hybrid welded high strength steel joints. *IIW Doc. IV-907–06*.
25. Bagger, C., Olsen, F. (2003) Comparison of plasma, metal inactive gas (MIG), tungsten inactive gas (TIG) processes for laser hybrid welding. In: *Proc. of ICALEO* (Jacksonville, Florida, USA), Section A, 11–20.
26. Nilsson, H., Kaplan, A. (2002) Influence of butt- and T-joint preparation in laser arc hybrid welding. *IIW Doc. XII-1732–02*.
27. Fellman, A., Salminen, A. (2005) A study of phenomenon of CO_2-laser welding with filler wire and MAG hybrid welding. In: *Proc. of ICALEO* (Miami, USA), 117–126.
28. Reisgen, U., Olschok, S. (2009) Laser-submerged arc hybrid welding. *The Paton Welding J.*, **4**, 38–42.
29. Gao, M., Zeng, X., Hu, Q. et al. (2009) Laser-TIG hybrid welding of ultra-fine grained steel. *J. Materials Processing Techn.*, **209**, 785–791.
30. Liming, L., Gang, S., Liang, G. et al. (2005) Pore formation during hybrid laser-tungsten inert gas arc welding of magnesium alloy AZ31B — mechanism and remedy materials. *Sci. and Eng. A*, **390**, 76–80.
31. Liu, L.M., Zhao, X. (2008) Study on the weld joint of Mg alloy and steel by laser GTA hybrid welding. *Materials Characterization*, **59**, 1279–1284.
32. Arias, J.L., Romero, P., Vandewynckele, A. et al. (2005) Laser-TIG hybrid welding of very thin austenitic stainless steel sheets. In: *Proc. of ICALEO* (Miami, USA), 104–107.
33. Nielsen, S.E., Andersen, M.M., Kristensen, J.K. et al. (2002) Hybrid welding of thick section C/Mn steel and aluminum. *IIW Doc. XII-1731*.
34. Walduck, R.P., Biffin, J. (1994) Plasma arc augmented laser welding. *Welding and Metal Fabr.*, **4**, 172–176.
35. Wibowo, M.K. *A study of hybrid laser-plasma arc welding:* NIMR cl. 8 report (Joining Technologies).
36. Devermann, T., Biffin, J., Blundell, N. (2002) Plasma augmented laser welding and its applications. *Sci. and Techn. of Welding and Joining*, 7(**1**), 1–10.
37. Fuerschbach, W.P. (1999) Laser assisted plasma arc welding. In: *Proc. of ICALEO*, Section D, 102–108.
38. Staufer, H. (2005) High productivity by using laser-GMAW and laser tandem-hybrid processes for thick plates. In: *Proc. of IIW Int. Conf.* (Praque, Czech Republic), 66–68.
39. Dilthey, U., Olschok, S. (2004) Untersuchungen zur Nutzung der synergieeffekte bein Hochleistungs-laser hybridschweissen von dickwandigen Rohrkorpern aus C–Mn Stahlen. In: *Abschlusssbericht des AiF-Forschungsvorhabens 13.407N*. Aachen.
40. Coiffier, J.C., Jansen, J.P., Peru, G. et al. (1997) Combination of laser beam and submerged arc processes for the longitudinal welding of large welded pipes. In: *Proc. of Int. Symp. on High Strength Steels* (Trondheim, Norway).

MANUFACTURE OF DRILL BITS FOR PRODUCTION OF DISPERSED METHANE IN MINE WORKING

V.F. KHORUNOV, S.V. MAKSYMOVA and **B.V. STEFANIV**
E.O. Paton Electric Welding Institute, NASU, Kiev, Ukraine

The effect of the brazing temperature on performance of diamond-hard alloy cutters was investigated. It was shown that a combination of the developed brazing filler metals and technology provided a substantial increase in length and rate of well drilling, which was proved by the industrial test results.

Keywords: *superhard materials, diamond layer, diamond-hard alloy cutter, rock destruction tool, bit, methane, brazing, brazing filler metal*

The main tool for efficient drilling of the earth's interior in production of hydrocarbons is a bit for rotary drilling, which is classified as a bit with fixed cutters, or roller bit, intended for different rock types and a wide range of conditions [1]. The bits with fixed cutters have blades, which are a single whole with the body and are rotated together with it. The roller bits have metal roller cones, which are independently rotated with rotation of a bit in a working face.

The cost of drill bits is only 1–5 % of the total cost of a well, but they directly determine the cost of drilling a unit length of the well, as the time required to drill it depends upon the drilling rate and service life of a bit till wear. The bits with fixed cutters are more expensive. But they drill quicker and their lifetime is longer, compared to the roller ones, in some hard and abrasive rock. They can be fitted with cutters with natural or synthetic diamonds. Cutters with synthetic polycrystalline diamonds are more resistant to impact loads than with the natural ones, and are very efficient in hard, moderately abrasive rock. The efficiency of using these diamonds is limited by thickness of a diamond plate, which is determined by diffusion of cobalt from the hard-alloy substrate into the diamond layer, as well as by stresses induced by thermal expansion of tungsten carbide and its shrinkage. High residual stresses and dry diamond grains may cause delamination, exfoilation and cracking in the diamond plates as a result of incomplete penetration of cobalt in synthesis of polycrystalline diamonds. In turn, this reduces the service life of a cutter and a bit as a whole [1].

In the CIS countries, the key materials to manufacture tools are cermet hard alloys of the type of VK-6, VK-8, VK-15, VK-20 etc., and superhard materials, such as natural and synthetic diamonds. Theoretical and technological principles of producing such materials were worked out by the V.N. Bakul Institute for Superhard Materials of the NAS of Ukraine [2, 3].

The purpose of this study was to select brazing filler metals, develop technology for brazing diamond-hard alloy cutters (DHAC) and technology for manufacturing drill bits. The DHACs (Figure 1) are manufactured by brazing diamond-hard alloy plates (DHAP) to hard alloy holders (HAH), i.e. tungsten carbide base alloys, where cobalt (2 to 25 wt.%, depending on the alloy grade) is used as a binder. The DHACs employed in the experiments were hard alloy cylinders with a diameter of 13.5 mm and height of 3.5 mm, coated with a 0.7–0.8 mm thick layer of synthetic polycrystalline diamonds. The diamonds used in the form of crystals with a maximal size of 20–60 μm are characterised by shape stability, high hardness, wear resistance, and low thermal expansion coefficient.

Diamond is a meta-stable modification of carbon, and physical-mechanical properties of the diamond layer dramatically degrade in heating of DHAP to a critical temperature (670–700 °C) [3, 4] because of diffusion interaction between the diamond particles and cobalt (Figure 2). Catalytic graphitisation of polycrystalline synthetic diamonds, formation of cracks due to different thermal expansion coefficients of diamond and cobalt, and, as a result, fracture of the diamond layer take place.

The temperature of graphitisation of each grade of synthetic polycrystalline diamonds depends upon many factors, including the degree of purity (content of metal catalyst impurities), heating environment and time of holding at an increased temperature. Therefore, to manufacture DHAC by brazing traditional DHAP (with polycrystalline synthetic diamonds) to hard alloys, it is necessary to allow for the above peculiarities of the synthetic diamonds. Melting point

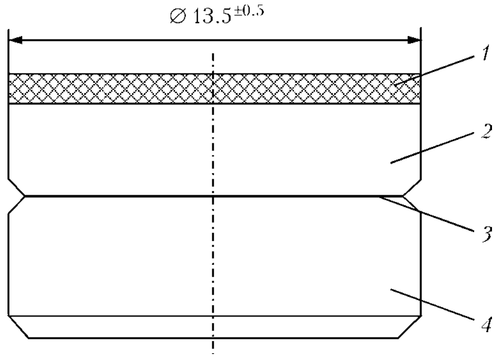

Figure 1. Schematic of DHAC: *1* — diamond layer; *2* — hard alloy substrate; *3* — brazed seam; *4* — HAH

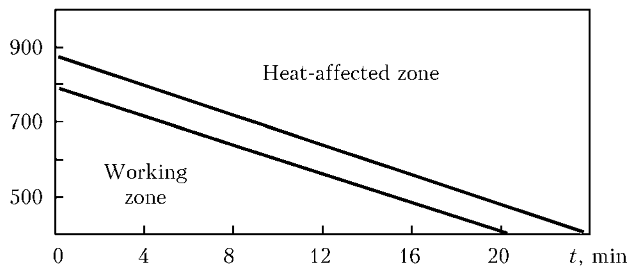

Figure 2. Dependence of ultimate heating temperature of DHAP on heating time

of a brazing filler metal should not exceed 650–700 °C, and it should be characterised by good fluidity and wettability with respect to the base materials. As the base material and brazing filler metals have substantially different thermal expansion coefficients, the filler metals should be characterised by a high ductility for relaxation of stresses induced at the interface between the phases. Moreover, considering loads that affect DHAC during operation, shear strength of the brazed seam should be not lower than 300 MPa, and wear of DHAC under the test conditions given below should be no more than 0.2 mm.

Such contradictory requirements are hard to meet with the DHAC manufacturing technology that exists since the Soviet time and with the available brazing filler metals. For example, copper-zinc filler metals alloyed with different elements, which improve their physical-mechanical and technological characteristics, have received wide acceptance for joining hard alloys. These filler metals spread well over hard alloys and are extensively applied to produce joints of these materials. However, using them for brazing DHAP leads to degradation of synthetic diamonds because of a high temperature of the process.

Copper-silver filler metals characterised by a low melting temperature, sufficient ductility and good fluidity hold more promise for brazing DHAP to hard alloys. The base in this case is eutectic alloy of the Cu–Ag system with a melting point of 779 °C [5]. Adding such materials as zinc, cadmium and tin allows the melting point of filler metals to be decreased, this having a positive effect on their technological properties. The area of spreading of filler metals greatly depends upon their composition (Table).

It should be noted that joining DHAP to HAH is, in fact, brazing of two hard alloys, as the diamond coating is located on the outer surface of DHAP. Therefore, at the first stage, to determine shear strength of the brazed joints, two plates of hard alloy VK-8 simulating DHAC were brazed to each other. That made the investigations much simpler and less expensive.

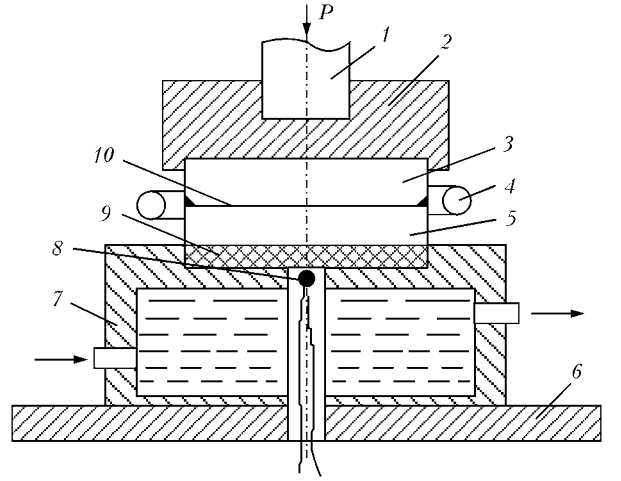

Figure 3. Schematic of fixture for brazing DHAC: *1* — hold-down; *2* — support; *3* — HAH; *4* — inductor; *5* — DHAP; *6* — substrate; *7* — cooler; *8* — thermocouple; *9* — diamond layer; *10* — brazed seam

As shown by the results of mechanical tests, filler metals of the copper-silver system alloyed with other elements (zinc, manganese, nickel etc.) provide a sufficient shear strength (about 300 MPa). However, the shear strength is a mandatory, but insufficient parameter for choosing optimal composition of a filler metal to be used to manufacture DHAC.

To generate the reliable information, it is necessary to subject the brazed joints to the comprehensive tests, which make it possible to evaluate strength and wear resistance. Wear resistance is a key parameter that most realistically reflects service conditions of drill bits fitted with diamond cutters. The level of wear resistance depends upon the temperature of heating of the diamond layer and time of holding at this temperature. Therefore, brazing of DHAC to investigate wear resistance was carried out in a special fixture (Figure 3), where the diamond layer contacted the surface being cooled (to compare, some cutters were brazed without cooling). The heating parameters provided by generator VChI4-10U4 were as follows: I_{grid} = 0.1 A, I_{anode} = 0.6–0.7 A. The resulting cutters (Figure 4) were tested on a rig that simulated real

Area of spreading of brazing filler metals over hard alloy substrate

Basic system (filler metal grade)	Heating time, s	Filler metal melting temperature range, °C	Filler metal spreading area, mm^2
Ag–Cu–Zn–Cd (PSr-40)	24	590–610	89.87
Ag–Cu–Zn (PSr-45)	27	665–730	67.63
Ag–Cu–Zn–Sn (BAg-7)	26	618–651	46.33
Ag–Cu–Zn–Ni–Mn (BAg-22)	23	680–699	121.40
Cu–Zn–Mn–Sn–Ni (PM-50)	25	780–870	119.18
Cu–Mn–Fe–Ni (PM-72)	40	810–890	50.19

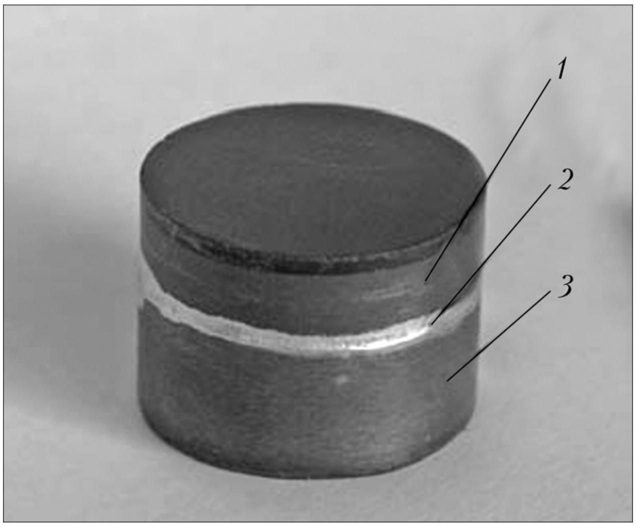

Figure 4. Brazed DHAC for drill tools: *1* — DHAP; *2* — brazed seam; *3* — HAH

service conditions. In other words, it was gouging of the rock (e.g. quartz sandstone) for which a given cutter was meant.

The test parameters were as follows: longitudinal feed speed — 0.55 m/s, cut depth — 0.5 mm, transverse feed — 28 mm/pass, no cooling, and rock destruction products were not removed from the gouging zone (no water was used). The value of wear after gouging was measured on the rear edge of DHAC by using optical microscope. The tests conducted allowed choosing the filler metals that provided the required level of wear resistance, which was not in excess of 0.2 mm. The results obtained were used to develop the technology for brazing DHAC to a blade. This is the most critical operation in terms of maintaining properties of the diamond layer. With the traditional technology, brazing of the cutters is performed in series, i.e. the previous cutter is subjected to repeated heating when brazing the next cutter. Moreover, induction heating is sometimes combined with flame (surface) one, this being dangerous in terms of the probability of the direct contact of the diamond layer with the torch flame.

The special design of an inductor providing a uniform temperature field within the zone of brazing of cutters was developed in the course of this study. That made it possible to perform simultaneous brazing of all cutters by using only high-frequency heating. With this technology, the diamond layer is held at a high temperature for a minimal time and preserves its properties required for operation. It should be noted that the optimal compositions of filler metals provide good wetting of low-alloy steel of a blade and substrate material of the cutters, as well as reliable fixation of the latter in the blade (Figure 5).

Joining of blades to the body was carried out by semi-automatic MIG welding in argon atmosphere. Welding conditions, quantity and sequence of deposition of welds, time pauses for cooling of the welds etc. were selected. The special attention was given to welding of the upper part of a bit, where the welding arc went closely to the diamond layer.

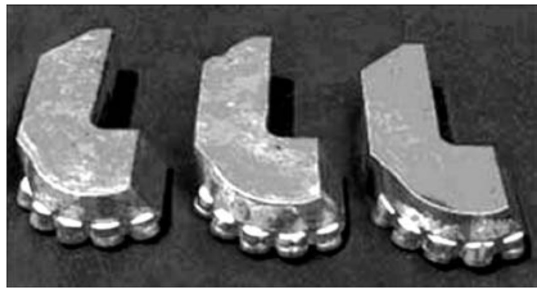

Figure 5. Blades of drill bits with DHAC brazed into them

Figure 6. Drill bit fitted with DHAC

The developed technology and filler metals were applied to manufacture a batch of the bits intended for drilling the medium-hardness rock (Figure 6). The bits successfully passed industrial tests and were used in the process of production of dispersed methane at the A.F. Zasyadko Mine.

The industrial tests showed that application of the optimal compositions of filler metals and the developed technology by using the domestic DHAPs allowed increasing the drilling length from 100–120 to 400–450 m. When using foreign DHACs with no change in design of the bit and stabiliser, the drilling length was increased to some extent, but capabilities of these cutters were underutilised. And only the combination of the improved design of the bit and stabiliser, developed brazing filler metals and technology made it possible to achieve a drilling length of over 1000 m (without repair). After removal of accidental damages caused, e.g. by harder rock inclusions, the drilling length increased to 1500–1700 m or more.

1. (2000) Besson, A., Burr, B., Dillard, S. et al. (2000) On the cutting edge. *Oilfield Rev.*, Autumn, 36–57.
2. Novikov, I.V. (2008) Development of synthesis of superhard materials. In: *Actual problems of current materials science*. Vol. 2. Kiev: Akademperiodika.
3. (2005) *Tools from superhard materials*. Ed. by N.V. Novikov. Moscow: Mashinostroenie.
4. Artyukhov, V.P., Pruss, O.P. (1997) Analysis of the processes of brazing of diamond-hard alloy cutters. *Sverkhtv. Materialy*, **2**, 38–43.
5. (1996) *Constitutional diagrams of binary metallic systems*: Refer. Book. Ed. by N.P. Lyakishev. Vol. 1. Moscow: Mashinostroenie.

APPLICATION OF PULSE ELECTROMAGNETIC EFFECTS TO CONTROL THE PROCESS OF ELECTRODE METAL TRANSFER IN ARC WELDING

P.Yu. SIDORENKO and **R.N. RYZHOV**
NTUU «Kiev Polytechnic Institute», Kiev, Ukraine

The impact of electromagnetic effects induced by axial pulse magnetic fields on parameters of electrode metal transfer in metal-arc welding was evaluated.

Keywords: *arc welding, pulse electromagnetic effects, control of transfer, axial controlling magnetic fields*

Control of electrode metal transfer in arc welding is an important problem, the solution of which allows reducing metal losses for spattering and improving the weld formation.

The use of electromagnetic effects (EME) is one of the most efficient methods for controlling the transfer process. These effects based on axial low-frequency magnetic fields were successfully applied in submerged metal-arc welding [1, 2]. However, application of these effects in gas-shielded welding received no acceptance because of increased spattering caused by the impact on metal drops by the centrifugal forces formed in rotation of the drops at the electrode tip.

The EME based on the pulse axial controlling magnetic fields (CMF) were used to advantage to provide proportioned transfer of filler metal in arc brazing [3] and increase hot crack resistance of TIG welds [4]. As shown by analysis, no experience of using EME in metal-arc welding is available now. Unlike the widely applied EME based on the low-frequency magnetic fields, the EME under consideration are based on the force impact on the molten metal drops, which is generated as a result of interaction of the magnetic field with eddy currents induced in their volumes.

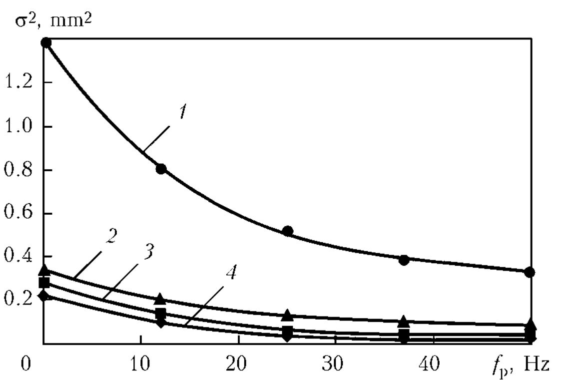

Figure 1. Dependence of variance of distribution of electrode metal drop sizes on frequency of axial pulse CMF in welding using flux-cored wire PPT-9 (*1*), CO_2 welding (*2*), welding in a mixture of Ar + 18 % CO_2 (*3*), and welding in argon atmosphere (*4*)

Investigations were carried out in gas-shielded (Ar, 82 % Ar + 18 % CO_2, and CO_2) metal-arc welding of low-carbon steel, and in welding using self-shielding flux-cored wire of the PPT-9 grade. VDU-504 unit was used as a welding power supply. Sizes of the electrode metal drops detached from the electrode tip were fixed by using a digital camera. The welding parameters are given in the Table. Sizes of the drops were determined, and variance (deviation of sizes of the drop from their mean value characteristic of a given transfer frequency) was calculated after computer processing of images of the arc region.

It was found that the size of the drops detached from the electrode tip in welding under conventional conditions may vary 2 times. The use of the given EMF leads to decreased variance of distribution of sizes of the drops in welding in argon atmosphere by 92 %, in a mixture of Ar + 18 % CO_2 — by 85 %, and in CO_2 — by 74 % (Figure 1).

The highest value of variance was observed in flux-cored wire welding, which is attributable to non-uniform melting of the charge and sheath, having different physical-chemical properties and specific characters of the energy balance at the electrode extension [5]. The above factors make the electrode metal transfer process unstable.

The impact of pulse EME on losses of electrode metal for spattering was evaluated. The level of spattering was determined by the standard procedure. It is a known fact [6] that CO_2 welding is characterised by increased losses of electrode metal for spattering, this being associated with systematic short-circuiting of the arc gap accompanied by blowups of the bridges. In this case, metal may spatter both from electrode and from pool [7]. Similar results were obtained in the course of the experimental investigations (Figure 2).

The use of pulse EME allows reducing the electrode metal losses in welding in argon atmosphere by 38 %, in welding in a mixture of Ar + 18 % CO_2 — by 43 %, and in CO_2 welding — by 32 %. This effect is explained by a decreased number of short-circuits due to a decreased size of the drops. In addition, the use

Parameters of gas-shielded metal-arc and self-shielding flux-cored wire welding of low-carbon steel

Wire grade	Shielding gas	I_w, A	U_a, V
Sv-08G2S, 1.2 mm diameter	Ar	100	24
	82 % Ar + 18 % CO_2		
	CO_2	110	22
PPT-9, 2.5 mm diameter	–	200 175	34 26

of these pulse effects makes it possible to control movement of the drops into the weld pool.

Investigations with flux-cored wire welding were performed in two modes differing in arc voltage (see the Table). The experiments showed that increase in the arc voltage leads to a substantial decrease in the spattering level. This, like in the previous case, is associated with a decreased probability of short-circuits.

Increase of the frequency of the EME under consideration was accompanied by a 30 % decrease in size of the transferred drops, and by an exponential decrease in the coefficient of losses of electrode wire metal for spattering (Figure 2). Welding at a lower voltage is characterised by instability of the processes of electrode metal transfer, and by a higher variance of distribution of the drop sizes. Most probably, it is this fact that determines the increased losses for spattering (up to 12.5 %, see Figure 2).

Therefore, application of EME based on the axial pulse magnetic fields allows increasing the frequency of transfer of the drops and, accordingly, decreasing their sizes. The efficiency of the given EME grows with increase of the frequency of the CMF pulses. As a result, this makes it possible to reduce the electrode wire metal losses for spattering.

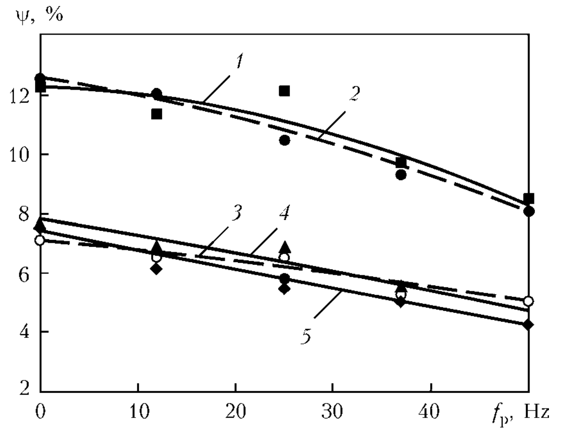

Figure 2. Variations in coefficient of electrode metal losses for spattering in welding with pulse EME: *1, 4, 5* — CO_2 welding, welding in a mixture of Ar + 18 % CO_2, and welding in argon atmosphere, respectively; *2, 3* — welding with flux-cored wire PPT-9 at U_a = 26 and 34 V, respectively

1. Zavialov, V.E., Zvorono, Ya.P., Petrakov, A.B. (1990) Application of longitudinal magnetic field in submerged-arc surfacing. *Svarochn. Proizvodstvo*, **2**, 3–6.
2. Zernov, A.V. (1972) Application of longitudinal magnetic fields in automatic submerged-arc welding of root welds of pipeline roll butt joints. *Ibid*., **3**, 26–27.
3. Tarasov, M.M., Kapustin, S.S. (1982) Application of high-frequency electromagnetic field for proportioned electrode metal drop transfer. *Avtomatich. Svarka*, **8**, 10–12.
4. Ryzhov, R.N. (2007) Influence of pulse electromagnetic actions on formation and solidification of welds. *The Paton Welding J*., **2**, 49–50.
5. Pokhodnya, I.K., Suptel, A.M. (1972) *Flux-cored wire welding*. Kiev: Naukova Dumka.
6. Khejfits, A.L. (1986) Comparative evaluation of some methods for reduction of spattering in CO_2 welding. *Avtomatich. Svarka*, **3**, 58–60.
7. Potapievsky, A.G. (1974) Types of metal spattering in CO_2 welding. *Ibid*., **5**, 10–12.

SOLEMN MEETING DEDICATED TO THE JUBILEE OF VICTORY IN THE GREAT PATRIOTIC WAR

A solemn meeting dedicated to the 65th anniversary of Victory in the Great Patriotic War was held on May 7, 2010 at PWI at the legendary tank T-34. Among those present were participants of the GPW, PWI scientific staff members, administration and leading specialists, representatives of the young generation.

The meeting was opened by Prof. Boris E. Paton, who expressed his sincere jubilee congratulations for the veterans. He noted a significant contribution to the Victory of that small but united PWI team, who worked heroically in the Urals during the war years, doing everything in their power for the fastest liberation from the fascist yoke.

Then the meeting was addressed by Prof. I.K. Pokhodnya, I.M. Kokojko, retired Major-General, now the staff member of the Presidium of NASU, A.I. Fomin, PWI veteran, former flux maker, and A.N. Kornienko, Dr. of Sci. (Hist.).

It was noted in the speeches that PWI which was evacuated to Nizhny Tagil already at the start of 1942, determined the causes for crack initiation in armour steel joints, developed technologies of sound welding and automatic machines for manufacture of complex three-dimensional structures of tank armoured bodies. It was possible to achieve a stable high quality of the joints at welding speed, which was 8 times higher than the speed achieved by the best manual welders. Teenagers could and did work as automatic machine operators. 250 welders were freed just in the Nizhny Tagil plant. In 1942–1943, 20 designs of machines for welding the tank bodies and 8 designs of machines for welding air bombs and ammunition were developed and realized, and flow lines were designed. Institute's scientific staff went out to plants, worked directly in the shops and trained welders. Under such hard conditions the Institute's team consisting of three dozen people officially working for 12 hours seven days a week, managed to resolve a lot of other organizational and technological problems. Fluxes from local raw materials were developed including blast-furnace slags. The phenomenon of self-regulation of consumable electrode arc processes was discovered for the first time in the world. It was the basis for designing simplified automatic welding heads with a constant speed of electrode wire feed. By the end of 1943 the work was performed in 52 defense industry plants, which have mastered submerged-arc welding.

During the war years, the automatic machines welded 4 mln m of welds, saved 5 mln kW/h of power, and labour consumption of tank body manufacture was reduced 5 times. By the end of the war, the country's plants produced up to 30,000 heavy and medium tanks and self-propelled guns annually. All together 102,857 tanks and self-propelled guns were produced in the Soviet Union during the war years.

It is highly important that the growing generation had a clear idea of the great contribution made by Ukraine into Victory and subsequent reconstruction of the post-war world.

Editorial Board
of «The Paton Welding Journal»

AUTOMATIC MACHINES ADTs 625, ADTs 626 AND ADTs 627 FOR ORBITAL WELDING OF PIPELINES

The welding complexes ADTs 627 U3.1, ADTs 625 U3.1 and ADTs 626 U3.1 developed at the Research Engineering Centre of Welding and Testing in Atomic Energy of the E.O. Paton Electric Welding Institute are designed for automatic orbital welding with non-consumable (tungsten) electrode in shielding gases (mainly argon) of position welds of 8–76 mm diameter pipelines of up to 4 mm wall thickness, manufactured of steels of pearlite, austenite classes and high alloys, under site conditions and for repair of objects of power engineering, including nuclear power stations, heat power stations and also of other fields of industry.

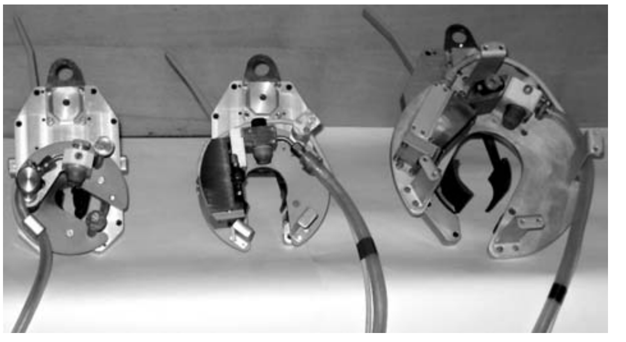

Brief technical characteristics of automatic machines

Parameter	ADTs 627	ADTs 625	ADTs 626
Diameter of pipes being welded, mm	8–24	18–42	45–76
The smallest distance between pipes, mm	60	65	80
Ranges of welding speed adjustment, m/h	1–20		
Diameter of tungsten electrode (of grades VL, VI or VT), mm	1.6	2.0	3.0
The largest radial movement of torch, mm	15	16	20
The largest torch movement across the butt, mm	±1	±5	
Cooling of torch	Gas		
Ranges of welding current adjustment, A	8–250		
Ranges of arc voltage adjustment, V	9–18		
Accuracy of welding current maintenance, %	not more than ±2		
Accuracy of arc voltage maintenance, V	not more than ±0.20	±0.15	
The highest speed of torch movement relative to mechanism AAAV, mm/s	–	10	
Location of electric drive of rotation of face-plate	Parallel to the pipe axis		
Mass of welding head, kg	not more than 3.0	3.5	4.9
Consumed electric power, kV·A	not more than 6		

Each welding complex consists of

❖ multifunctional power source for welding using non-consumable electrode in inert gases (TIG welding)
❖ controller unit (control system)
❖ remote control panel
❖ one of welding heads (ADTs 627, ADTs 625, ADTs 626)
❖ collector
❖ set of connecting cables, wires and hoses

Power source of increased reliability provides

❖ formation of the steep-falling «boyonet» external volt-ampere characteristics necessary for TIG welding process and high dynamic properties similar to welding inverters

❖ presetting of values of welding current and time parameters of components of welding cycle by welding current and inert gas supply (duration of time intervals «gas before welding», «smooth increase in welding current», «heating», «smooth decrease in welding current», «gas after welding»)

❖ contactless exciting of welding arc using high-voltage breakdown of arc gap

❖ stabilization of preset values of welding current and time parameters of welding cycle at the influence of external disturbances (fluctuations in voltage of mains, changes in length of arc gap and other)

❖ realization of modes of automatic pitch-pulsed welding and welding using modulated current and also welding cycles in the modes 2T, 4T and in a special mode 4T-I

❖ possibility of remote control

Controller unit (control system)

❖ generates signals of control of switching on, switching off and duration of operation of components and mechanisms of welding set in the modes SETTING UP and WELDING according to programmed algorithms of performance of TIG welding of position welds of pipelines

❖ provides control and maintenance of stable value of preliminary set speed of rotation of face plate of welding head (welding speed)

❖ realizes control of functioning of automatic controller of arc voltage of welding heads providing maintaining of stable length of arc gap during welding due to automatic compensation of its deviations from preset value by correction of position of electrode of welding head relative to the workpiece being welded in accordance with the deviations of welding arc voltage

Remote control panel consists of control units, signalization and indication, providing selection or presetting of

• kind of work of welding complex (setting up/welding)
• kind of control mode (automatic/manual)
• kind of welding mode (continuous/pulsed)
• direction of rotation of face plate of welding head (forward/backward)
• directions for the mode of setting the radial movement of electrode of welding head (electrode up/down)
• preliminary control of consumption of inert gas (gas control)
• switching on/switching off of welding cycle (start/stop)
• values of arc voltage U_a
• values of welding speed v_w
• correction of values of welding current ΔI_w in the process of welding
• digital indication of preset and current values of welding current I_w, arc voltage U_a, welding speed v_w and consumption of inert gas (GAS)

Each welding head includes

❖ body of light-weight structure
❖ clamping mechanism of welding head on the pipe
❖ face plate rotated around the pipe axis
❖ mechanism of face plate rotation
❖ welding torch
❖ executive mechanism of vertical movement of torch of welding system of automatic control of arc voltage in welding heads ADTs 625 and ADTs 626 and system of mechanical copying in welding torch ADTs 627

Design of welding heads provides

• quick installing and fastening of head on pipeline being welded and its removal by one welder-operator
• reliable fastening of head body on the pipeline which excludes its displacement caused by shocks and vibration
• accuracy of installing of a head on the pipeline (non-parallelism of the axis of welding torch relative to the axis of pipeline does not exceed 3°)
• reverse of rotation direction of face plate (on the command of control system of welding complex)
• quick replacement of worn-out tungsten electrode of welding torch
• laminar flow of inert gas and reliable protection of welding zone
• possibility of transverse correction of position of welding torch electrode relative to the butt of pipeline

Connection of any of welding heads to the power source, controller unit, control panel and system of gas supply is performed using a collector.

The distinctive feature of these welding complexes is their capability to provide the quality process of automatic orbital TIG welding of position welds of pipelines at the length of welding circuit of up to 60 m.

Eng. Gavva V.M.

INFORMATION FOR CONTRIBUTORS TO THE PATON WELDING JOURNAL

«The Paton Welding Journal» is an English translation of the monthly «Avtomaticheskaya Svarka» journal published in Russian since 1948.

THE PATON WELDING JOURNAL is a scientific journal publishing fundamental and applied papers and short notes in the area of:

- *weldability of structural materials*
- *welding different types of steels and cast irons*
- *welding non-ferrous metals, including aluminium, titanium, etc.*
- *joining dissimilar and composite materials*
- *welding refractory metals and alloys*
- *welding cryogenic materials*
- *arc welding*
- *flash-butt welding*
- *electron beam and laser welding*
- *explosion welding and cutting*
- *friction welding*
- *electroslag welding*
- *soldering and brazing*
- *advanced structural materials*
- *surfacing and coating deposition*
- *cutting*
- *computer technologies in welding*
- *strength of welded joints and structures*
- *residual stresses and strains*
- *calculation and design of welded joints and structures*
- *automation of welding fabrication*
- *estimation of residual life of welded structures*
- *welding for fabrication of unique structures*
- *welding and repair in thermal and nuclear power engineering*
- *advances in underwater welding, cutting and repair*

The journal accepts also advertisements and announcements of conferences and publications on related topics.

THE PATON WELDING JOURNAL is published monthly.

Subscription requests should be sent to the Editorial Office.

Manuscripts should be submitted in duplicate in English, and supplemented with a text file and figures on a diskette. An electronic copy may be submitted by e-mail.

The rules for submission of electronic copies are as follows:

- an electronic copy should be submitted on a diskette or by e-mail simultaneously with sending a hard copy of the manuscript;
- acceptable text formats: MSWord (rtf, doc);
- acceptable graphic formats for figures: EPS, TIFF, CDR. Figures created using software for mathematical and statistical calculations should be converted to one of these formats.

Manuscripts should be supplemented with:

- official letter signed by a chief manager of the institution where the work was performed. This rule does not apply to papers submitted by international groups of authors.

Title page:

- title of the paper and name(s) of the author(s);
- name of affiliated institution, full address, telephone and fax numbers, e-mail addresses (if available) for each author.

Abstract: up to 100 words, must be presented in English. Before the abstract text one should indicate in the same language: the paper title, surnames and initials of all authors.

Key words: their amount must not exceed eight word units. In the specific cases it is acceptible to use two- or three-word terms. These words must be placed under the abstract and written in the same language.

Text should be printed double-spaced on white paper (A4 format) with a 12-point font. Titles of the paper and sections should be typed with bold capitals.

Tables should be submitted on separate pages in the format of appropriate text processors, or in the text format (with columns separated by periods, commas, semicolons, or tabulation characters). Use of pseudo-graphic characters is not allowed.

List of references should be double-spaced, with references numbered in order of their appearance in the text.

Captions for figures and tables should be printed in the manuscript double-spaced after the list of references.

Pictures will be scanned for digital reproduction. Only high-quality pictures can be accepted. Inscriptions and symbols should be printed inside. Negatives, slides and transparencies are accepted.

Figures: each figure should be printed on a separate page of the manuscript and have a size not exceeding 160 × × 200 mm. For text in figures, use 10-point fonts. All figures are to be numbered in order of their appearance in the text, with sections denoted as (a), (b), etc. Placing figure numbers and captions inside figures is not allowed. On the back side, write with a pencil the paper title, author(s) name(s) and figure number, and mark the top side with an arrow.

Photographs should be submited as original prints.

Color printing is possible if its cost is covered by the authors.

For information about the rules and costs, contact the Executive Director.

No author's fee is provided for.

Publication in TPWJ is free of charge.

Manuscripts should be sent to:

Dr. Alexander T. Zelnichenko
Executive Director of
«The Paton Welding Journal»,
11, Bozhenko Str.,
03680, Kiev, Ukraine
International Association «Welding»
Tel.: (38044) 287 67 57, 529 26 23
Fax: (38044) 528 04 86
E-mail: journal@paton.kiev.ua
www.nas.gov.ua/pwj

SUBSCRIPTION
FOR «THE PATON WELDING JOURNAL»

If You are interested in making subscription directly via Editorial Board, fill, please, the coupon and send application by fax or e-mail.

The cost of annual subscription via Editorial Board is $324.

Telephones and faxes of Editorial Board of «The Paton Welding Journal»:

Tel.: (38044) 287 6302, 271 2403, 529 2623

Fax: (38044) 528 3484, 528 0486, 529 2623.

«The Paton Welding Journal» can be also subscribed worldwide from catalogues of subscription agency EBSCO.

SUBSCRIPTION COUPON	
Address for journal delivery	
Term of subscription since	200 till 200
Name, initials	
Affiliation	
Position	
Tel., Fax, E-mail	

ADVERTISEMENT IN
«THE PATON WELDING JOURNAL»
(DISTRIBUTED ALL OVER THE WORLD)

«AVTOMATICHESKAYA SVARKA»
RUSSIAN VERSION OF «THE PATON WELDING JOURNAL»
(DISTRIBUTED IN UKRAINE, RUSSIA AND OTHER CIS COUNTRIES)

External cover, fully-colored:
First page of cover
(190×190 mm) – $700
Second page of cover
(200×290 mm) – $550
Third page of cover
(200×290 mm) – $500
Fourth page of cover
(200×290 mm) – $600

Internal cover, fully-colored:
First page of cover
(200×290 mm) – $400
Second page of cover
(200×290 mm) – $400
Third page of cover
(200×290 mm) – $400
Fourth page of cover
(200×290 mm) – $400

Internal insert:
Fully-colored (200×290 mm) – $340
Fully-colored (double page A3)
(400×290 mm) – $570
Fully-colored (200×145 mm) – $170

- Article in the form of advertising is 50 % of the cost of advertising area
- When the sum of advertising contracts exceeds $1000, a flexible system of discounts is envisaged

Technical requirement for the advertising materials:

- Size of journal after cutting is 200×290 mm
- In advertising layouts, the texts, logotypes and other elements should be located 5 mm from the module edge to prevent the loss of a part of information

All files in format IBM PC:

- Corell Draw, version up to 10.0
- Adobe Photoshop, version up to 7.0
- Quark, version up to 5.0
- Representations in format TIFF, color model CMYK, resolution 300 dpi
- Files should be added with a printed copy (makeups in WORD for are not accepted)